5-2018

Studies on the Impact Initiation and Kinetics of Condensed Phase Reactives with Application to the Shock Induced Reaction Synthesis of Cubic Boron Nitride

Matthew T. Beason
Purdue University

STUDIES ON THE IMPACT INITIATION AND KINETICS OF CONDENSED PHASE REACTIVES WITH APPLICATION TO THE SHOCK INDUCED REACTION SYNTHESIS OF CUBIC BORON NITRIDE

by

Matthew T. Beason

A Dissertation

Submitted to the Faculty of Purdue University

In Partial Fulfillment of the Requirements for the degree of

Doctor of Philosophy

School of Mechanical Engineering

West Lafayette, Indiana

May 2018

THE PURDUE UNIVERSITY GRADUATE SCHOOL
STATEMENT OF COMMITTEE APPROVAL

Dr. Steven F. Son, Co-Chair
School of Mechanical Engineering
Dr. Ibrahim E. Gunduz, Co-Chair
School of Mechanical Engineering
Dr. Weinong Chen
School of Aeronautics and Astronautics
Dr. Alejandro Strachan
School of Materials Engineering
Dr. Lori J. Groven
South Dakota School of Mines and Technology, Department of Chemical and Biological Engineeering

Approved by:

Dr. Jay P. Gore
Head of the Graduate Program

For my wife, my family, and my friends.

ACKNOWLEDGMENTS

I would like to thank Professors Steven Son and Emre Gunduz for their advice and support throughout my graduate career. Additionally, the advice and expertise of David Adams and Professor Alexander Mukasyan have been invaluable for a significant portion of this work. I would also like to thank Professors Weinong Chen, Lori Groven and, Alejandro Strachan for their assistance and advice in various areas of this work as well as being members of my committee.

Mike Abere and Josh Pauls both made significant contributions to this work through their experimental contributions and discussions with the author. I would also like to acknowledge Andrew Justice, Omar Yehia, and Luciano Mozzone for assisting me with various experiments performed throughout this work. Furthermore, my tenure at Purdue has been enriched by a long series of lunches, game nights, and coffee runs that greatly enriched my graduate school experience.

Finally I would like to acknowledge the support of my family throughout my education. I would like to thank my parents, who supported and encouraged me the entire way. Most importantly, I would like to thank my loving and supportive wife, Anne, who kept me going.

This work was supported by the Department of Energy, National Nuclear Security Administration, under the award number DE-NA0002377 as part of the Predictive Science Academic Alliance Program II. Further support was given by the Department of Defense through a National Defense Science and Engineering Graduate (NDSEG) Fellowship.

TABLE OF CONTENTS

LIST OF TABLES

LIST OF FIGURES

ABSTRACT

Author: Beason, Matthew T. PhD
Institution: Purdue University
Degree Received: May 2018
Title: Studies on the Impact Initiation and Kinetics of Condensed Phase Reactives with Applications in the Shock Induced Reaction Synthesis of Cubic Boron Nitride
Committee Chair: Steven F. Son & I. Emre Gunduz

Shock induced reaction synthesis is a complex, scientifically rich field with the potentially to produce novel materials with unique properties. This work seeks to understand the processes governing shock induced reaction synthesis. Particular emphasis is placed on the reaction kinetics of condensed phase reactives under various mechanical and thermal heating rates. This understanding was then applied to the synthesis of cubic boron nitride through shock induced reaction synthesis.

Mechanical initiation of reactions in powder systems involve complex interactions that can yield unexpected results. Two materials that exhibit similar thermal responses can behave very differently under the same loading conditions due to differences in their mechanical properties. Reactive composite powders with small characteristic dimensions can exhibit short ignition delays and reduced thermal ignition thresholds; however, a full understanding of the response of these powders to rapid mechanical loading is still unclear. This work seeks to clarify the role of mechanical properties in impact induced ignition by considering the response of nanolaminate (NL) powders and high energy ball milled (HEBM) Ni-Al powders subjected to impact loading. The powders were placed into a windowed enclosure and mechanically loaded using a light gas gun, which allowed the resulting reactions to be observed using high-speed imaging. Even though the thermal ignition temperatures for the two powders are within 30 °C of each other, it was observed that the NL powders reacted on the microsecond timescale, immediately following the compaction wave for a short distance before decoupling from the compaction front. In contrast, the HEBM powders reacted after a several millisecond delay and clearly propagated as a deflagration front. Microindentation showed that the HEBM powders are much more ductile than those of NL. This suggests that the primary difference between the behavior of these materials on impact results from the ability and degree of the material to fracture, illustrating that the mechanical properties of a reactive material can have a dramatic effect on ignition during impact loading.

By using the jump equations to understand compaction events, it is easy to think about the compaction wave as a discontinuity, with no structure. In practice this is not the case. Both shock waves and compaction events have been observed to have a structure with a finite thickness. Studies of the propagation of shocks through monolithic solids have shown that the strain rate, which is directly related to the shock width, scales with the pressure rise to the fourth power. Studies of dynamic compaction of porous materials have shown that this relationship is closer to linear. This work seeks to study the effect that increasing the crush strength of the compact has on the width of the compaction wave. Ball milling is used to produce strain hardened powders that are then pressed to form a porous compact. Plate impact experiments are performed to evaluate the equation of state and measure the shock width of both milled and unmilled powders. The results show that a Mie-Gruneisen equation of state accurately predicts the response of all materials tested; however, the compaction width is found to change with milling condition. For all materials tested, the compaction width is found to decrease with increase pressure rise; however, the unmilled material is found to have a longer rise time compared to the ball milled material. This results in a reduction in apparent viscosity with increased crush strength. It is suggested that stress waves percolating ahead of the compaction front (since the velocity of the compaction wave is below the acoustic velocity of the parent material) and their interaction defines the compaction width. In a weaker material, a weaker stress is required to begin compaction, resulting in a broader front compared to a stronger material and an increased viscosity.

Despite their widespread use, the reaction pathways of thermite (reduction-oxidation) reactions are relatively unknown. Multilayer thin films produced through magnetron sputtering provide a highly controlled geometry and direct contact between reactives, making them an ideal platform to study atomic-scale processes underlying thermite reactions. This work utilizes the multilayer thin film geometry to study the combustion and reaction pathway of equimolar Al-NiO. The low heating rate kinetics and product phase growth are studied through hot-stage X-ray diffraction and differential scanning calorimetry. The results indicate significant product formation beginning as low as 180°C, and results in the formation of nickel aluminum intermetallic phases. Hot-plate ignition experiments show that ignition occurs in the solid state for fine bilayer thicknesses, with a transition to melt dependent reaction for multilayers with larger bilayer thicknesses. Laser ignition and self-propagating reactions are observed to exhibit a similar length scale dependence in reaction behavior. The activation energy determined from the hot-plate

ignition experiments was found to be less than that for the laser ignition experiments, indicating a heating rate dependent response.

This work culminates with the direct synthesis of cubic boron nitride through shock loading of 3B+TiN composite particles. It was found that reduction of the diffusion distance through high energy ball milling before loading was critical for success, with unmilled powders showing no evidence of reaction after recovery. The results show the possibility of rapid reaction occurring in a condensed phase system at microsecond timescales. As a results, optimization of this process may provide a route for the fabrication and discovery of other advanced compounds.

CHAPTER 1. INTRODUCTION

1.1 Objective and Motivation

The overarching objective of this work was to advance the current understanding of processes governing shock induced reaction synthesis. Specifically, this work sought to understanding the kinetics of condensed phase reactives at various mechanical and thermal heating rates in order to reduce the reaction timescale to a length relevant for reaction to occur under shock loading. This was accomplished through studies on the mechanical compaction of porous materials, the behavior of different nanolaminate reactive materials to weak mechanical loading, the kinetics of reaction in reactive multilayer thin films at varying heating rates, and application of shock induced reaction synthesis utilizing a condensed phase reactive to produce a metastable product phase.

The synthesis of these studies provides a view of the dynamic compaction of heterogeneous condensed phase reactives where different heating mechanisms are at play. It is often thought that condensed phase reaction is too slow to effect the propagation of a shock wave, and that the reaction timescale for a condensed phase reactive is on the ms timescale. This work addresses this misconception through a series of studies. Given sufficient length scale reduction, achieved through high energy ball milling or physical vapor deposition, it is shown that the reaction timescale can be varied from the ms timescale down to the μs timescale. Through low velocity impact experiments it is shown that the mechanical properties can dominate the reaction behavior of a condensed phase reactive, and dictate the intensity and type of hot-spots generated. Ultimately it is shown that a condensed phase reaction can occur on the time-scale of a shock by the recovery of a high pressure product phase resulting from a condensed phase reaction.

1.2 Organization

This work begins with an introduction describing the motivation and objectives of this work. Chapter 1 concludes with a brief description of the contents of each chapter and an explanation of the chapters place in the work.

A review of the relevant literature on dynamic compaction and shock induced reaction synthesis is provided in Chapter 2. This chapter reviews the necessary theory behind the jump equations and basic constitutive models relevant to powder compaction. It then discusses mechanisms of energy deposition during dynamic compaction. This is followed by a review of experimental techniques utilized in shock synthesis and a review of impact initiation of intermetallic reactives. This chapter concludes with a review of studies investigating the shock synthesis of metastable high pressure phases.

Chapter 3 investigates the behavior of different Ni-Al reactive composites to weak impact. This work contrasts two nano-scaled reactive composites composed of Ni-Al with comparable thermal ignition temperatures. One is produced through high energy ball milling, resulting in a tortuous microstructure lacking long range order. The other is produced by comminuting laminate materials produced through physical vapor deposition. The resulting powder maintains the periodic microstructure of the parent laminates. The resulting powders are found to react on different timescales when impacted under the same conditions. The high energy ball milled Ni-Al deflagrates long after pressure release. The nanolaminate powder is found to initial react with the propagation of the compaction front, travelling with a fixed delay behind the leading edge of the wave. These results are interpreted in light of the differing mechanical properties of the specific powders with general conclusions being presented.

The effect of the crush-strength of a powder on the structure and viscosity of a compaction wave is investigated in Chapter 4. By cold-pressing high energy ball milled Al, a series of Al green bodies are produced with varying crush-strengths. The equation of state and shock structure of this material is investigated through plate impact experiments and photonic Doppler velocimetry (PDV). The results show that while the equation of state of the porous compacts are unaffected by the strength of the parent material, the rise time of the compaction wave is dependent on the milling process with the ball milled powders propagating narrow compaction waves compared to the unmilled powders. An interpretation of the results is then presented.

An in depth study of the reaction kinetics of the Al-NiO system at varying heating rates is given in Chapter 5. The thin film geometry is utilized in order to directly control the microstructure being studied. The deposited material is examined to verify the stoichiometry and crystallinity of the produced material with particular attention paid to the composition and structure of the composition and structure at the material interfaces. Studies related to the reaction of the Al-NiO are then presented. Hot-stage X-ray diffraction (HS-XRD) is used to investigate the sequence of phase formation at heating rates relevant to differential scanning calorimetry (DSC) performed on the deposited films. This is followed by ignition studies at two different heating rates and observations about self-propagating reactions in free-standing foils. Activation energies are determined for the low rate experiments and the ignition experiments. The behavior of the system is then discussed as a function of diffusion length scale and heating rate.

Shock induced reaction synthesis is applied to the synthesis of cubic boron nitride (c-BN) in Chapter 6. Nano-scaled reactive composites composed of B and TiN are produced through high -energy ball milling. These powders are loaded to high pressures (20-25 GPa) through an explosive compaction experiment designed specifically for this work. A physical mixture of micron scale powder is found to not react under this mechanical loading; however, the ball milled B-TiN composites do react. Examination of the product phase through XRD and high resolution transmission electron microscopy (HRTEM) show that a high pressure polymorph of BN, c-BN, is formed as a product phase. The implications of the formation of c-BN under shock loading are discussed.

The work is summarized in Chapter 7. The results from each chapter are discussed in light of their role in shock induced reaction synthesis. Following this, paths for future work stemming from this research are suggested.

CHAPTER 2. BACKGROUND

2.1 The Jump Equations

The jump equations can be used to describe the propagation of steady planar one-dimensional pressure waves, as seen in Figure 2.1. These equations are derived from the conservation of mass, momentum and energy (see Davison [1] for a full derivation) and in Eulerian form are given by:

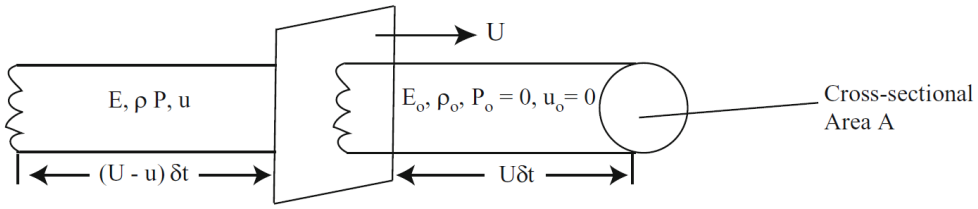

Figure 2.1. One-dimensional hydrodynamic flow [2].

$$\rho_0 U_s = \rho(U_s - U_p) \tag{2.1}$$

$$t_{11}^{+} - t_{11}^{-} = -\rho_0 U_s U_p \tag{2.2}$$

$$E - E_0 = -\frac{1}{2}(t_{11}^{+} - t_{11}^{-})\left(\frac{1}{\rho_0} - \frac{1}{\rho}\right), \tag{2.3}$$

where t_{11} is the component of the Cauchy Stress in the direction of propagation, ρ is the density, U_s is the velocity of the shockwave, U_p is the particle velocity and E is the internal energy with the subscript 0 representing the initial state. Since these equations (2.1-2.3) are derived directly from the conservation equations they have no dependency on the medium under question (i.e. there has been no constitutive response assumed) and are often used to interpret experimental results.

The pressure experienced by a material is given by the trace of the Cauchy stress tensor,

$$p = -t_{ii}. \tag{2.4}$$

The stress tensor can then be decomposed into the deviatoric stress, t_{ij}', and the pressure in the form:

$$t_{ij} = t'_{ij} - p\delta_{ij}, \tag{2.5}$$

where δ is the kronecker delta. The deviatoric stress in real materials is limited by the shear strength, τ_{max}, of the material. Since the pressure achievable is not limited in compression, eventually a state will be reached where $|p| >> \tau_{max}$. In this regime the deviatoric component of the Cauchy stress can be neglected [3] and the jump equations become:

$$\rho_0 U_s = \rho(U_s - U_p) \tag{2.6}$$

$$p - p_0 = \rho_0 U_s U_p \tag{2.7}$$

$$E - E_0 = -\frac{1}{2}(p - p_0)\left(\frac{1}{\rho_0} - \frac{1}{\rho}\right), \tag{2.8}$$

Equations 6-8 are most accurately applied in high shock or in materials with very low shear strength (fluids) when in a state of uniaxial strain.

2.2 Powder Behavior

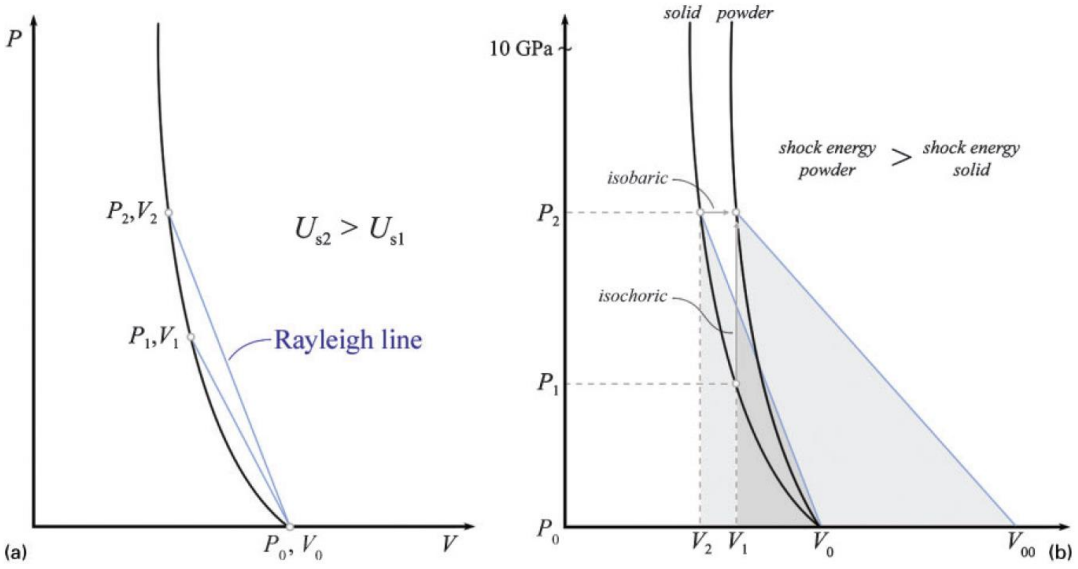

Figure 2.2. (a) P-V Hugoniot of a solid material. (b) Comparison of the Hugoniot of a powder with negligible compaction strength compared to the principal Hugoniot of the solid matrix[4].

The principal Hugoniot of material is the collection of states that can be achieved behind a shockwave passing through a material initially at atmospheric pressure and temperature, an example of which can be seen in figure 2.2(a). The line connecting the initial state to the final state in P-V space is called the Rayleigh line, The slope of which is proportional to $-(\rho_0 U_s)^2$. This relationship is interesting when comparing the response of a solid to a powder. The Hugoniot of a powder differs from a solid due to the increased specific volume at its initial state. This results in an increased amount of energy necessary to reach the same pressure as the solid, as evidenced by the shaded area in figure 2.2(b), as well as a reduced shock velocity compared to the a solid brought to the same pressure state, as evidenced by the slope of the respective Rayleigh lines.

The increased absorption capabilities of powders compared to solids results in compaction waves being attenuated while they propagate more rapidly than the equivalent solid. As a result, they can be used to attenuate unsupported shocks. A simple model describing the attenuation process for situations where the matrix material has negligible strength is given in section 2.2.1. Modelling the behavior of material where the matrix material is relatively strong is

more complicated. The most common method is outlined in section 2.2.2. The analysis in both 2.2.1 and 2.2.2 follows both Forbes [2] and Davison [1].

2.2.1 Snow Plow Model

The simplest model to understand powder compaction is the Snow Plow model. This model is non-physically, but it does provide several rules-of-thumb, with regard to shock attenuation in particular, that have correlated well with experiments [2]. To proceed, the Hugoniot of the porous material is idealized as a vertical and horizontal line as seen in Fig. 2.3. This assumes that the powder has no strength during crush-up, immediately compacting to full density at which point it is infinitely stiff. While there are occasions where the powder can be assumed to have negligible strength, the second assumption is never justifiable. This assumption results in an infinite sound speed in the material behind the compaction wave. The consequences of this will be seen later.

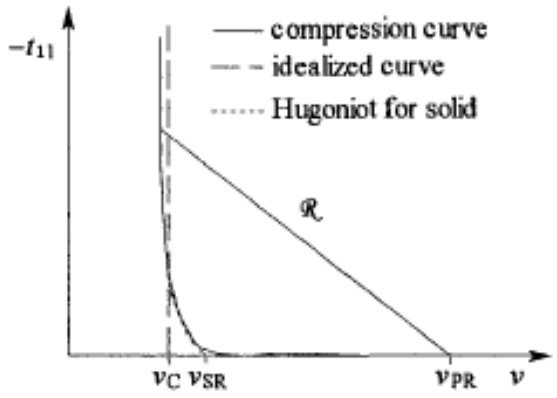

Figure 2.3. Comparison of a typical Hugoniot to the assumed Hugoniot in the snowplow model.

Combining equations 6 and 7 gives the following equation for the shock velocity and particle velocity,

$$U_s = v_1 \left(\frac{P}{(v_1 - v_2)}\right)^{\frac{1}{2}}, \tag{2.9}$$

$$U_p = \left(P(v_1 - v_2)\right)^{\frac{1}{2}}. \tag{2.10}$$

Considering a material with the Hugoniot represented in Fig. 2.3 being shocked from $v_1 = v_{00}$ to a solid density of $v_2 = v_{SR}$, or from $\alpha_1 = v_{00}/v_{SR}$ to $\alpha_2 = 1$, the peak shock and particle velocities are

$$U_s = v_{00} \left(\frac{P}{(v_{00} - v_{SR})}\right)^{\frac{1}{2}} = \left(\frac{P\alpha^2 v_0}{\alpha - 1}\right)^{\frac{1}{2}}, \tag{2.11}$$

$$U_p = \left(P(v_{00} - v_{SR})\right)^{\frac{1}{2}} = \left(Pv_0(\alpha - 1)\right)^{\frac{1}{2}}. \tag{2.12}$$

A square pulse traveling into the material of width $x = U_s dt$ will provide an initial impulse

$$I_0 = \frac{1}{v_{00}} x U_p = \frac{x U_p}{\alpha v_0}. \tag{2.13}$$

The total combining equations 11-13 it can be shown that

$$P \propto \frac{1}{x^2} \propto \frac{1}{t}. \tag{2.14}$$

Since the sound speed behind the compaction front is infinite and the total impulse, $I = \int p(x)dx$, is conserved, the waveform becomes a triangular pulse with the leading edge connected to the origin as seen in at three different times in Fig 2.4.

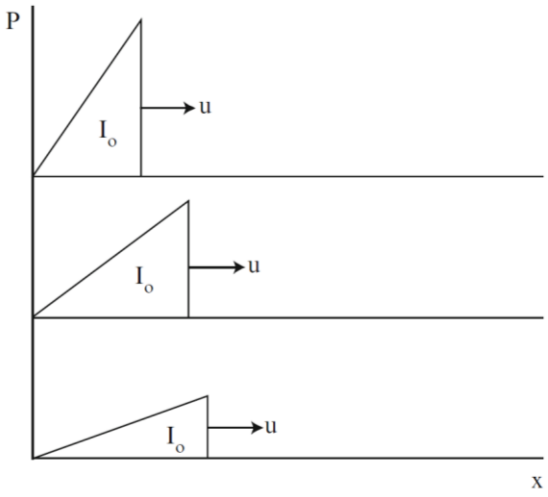

Figure 2.4. Predicted structure of a square input into a porous material with negligible strength analyzed with the Snowplow model.[5]

The key result from this analysis is equation 14. This proportionality shows that compaction wave's decay with distance travelled, and provides a comparison for experimental measurements. It is important to note that this analysis is for an unsupported square wave.

2.2.2 P-α Model

The P-α model is a constitutive law for powders that was originally proposed by Hermann [6] in 1969. In this model the internal energy of the parent material is given by

$$E = E_s(v, s), \tag{2.15}$$

where s is the specific entropy of the parent material. The key assumption of the model is that the internal energy of the parent material at a given specific volume and entropy is unchanged by converting it into a porous material. The internal energy of the porous material can then be expressed as

$$E = E(v, s, \alpha) = E_s\left(\frac{v}{\alpha}, s\right), \tag{2.16}$$

where $\alpha = v_{00}/v_0$ is the porosity of the material. This allows the pressure and temperature equations of state to be derived from the internal energy:

$$P = -\frac{\partial E(v,s,\alpha)}{\partial v} = -\frac{\partial E_s\left(\frac{v}{\alpha},s\right)}{\partial v} = -\frac{\partial E_s}{\partial v_s}|_s \frac{\partial v_s}{\partial v} = -\frac{1}{\alpha}\frac{\partial E_s}{\partial v_s}|_s = \frac{1}{\alpha}p_s(v_s,s), \quad (2.17)$$

$$T(v,s,\alpha) = \frac{\partial E(v,s,\alpha)}{\partial s} = \frac{\partial E_s\left(\frac{v}{\alpha},s\right)}{\partial s} = T_s\left(\frac{v}{\alpha},s\right). \quad (2.18)$$

The porosity can be defined to be a function of the internal energy and pressure

$$\alpha = \alpha(P,E), \quad (2.19)$$

and would be evaluated through a series of plate impact experiments at increasing initial temperature; however, it is often assumed that α is only a function of initial pressure due to the difficulty of these experiments. A full thermodynamic description is found from a suitable equation of state for the solid (i.e. Mie-Gruneisen) and an evolutionary equation for the solid. There have been many proposed forms for equation 19. Hollow sphere models typically use a logarithmic relation between critical pressure and the porosity resulting in an exponential form for the evolution equation [7–9] that is a function of the matrix yield strength and the pressure, such as

$$\alpha = \begin{cases} \alpha_0 \text{ if } P < P_{crit} \\ 1 - \frac{1}{e^{-\frac{3P}{2Y}}} \text{ if } P > P_{crit} \end{cases}, \quad (2.20)$$

where P_{crit} is a function of the initial porosity. It is often enough to fit experimental data in the region of incomplete compaction to a polynomial relating the final pressure and porosity [5,7]. The most common form is

$$\alpha = 1 + (\alpha_p - 1)\left(\frac{P_s - P}{P_s - P_e}\right), \quad (2.21)$$

where α_p is the porosity at the porous materials elastic limit, P_e, and P_s is the crush strength of the powder.

2.3 Mechanisms for Energy Deposition and Localization in powder Compaction

Understanding the mechanisms through which energy is deposited into a heterogeneous material through the passage of a shockwave and how that results in the initiation of reaction is

the primary goal in Hot-Spot theory [10–12]. It can be seen that if the energy deposited into a porous material was to be averaged over the entire volume of the material, the impact condition required to initiate reaction would be much greater than what is experimentally observed [10]. In order to understand the results and conclusions given later in this work a brief review of energy localization in powder compaction is given in this section.

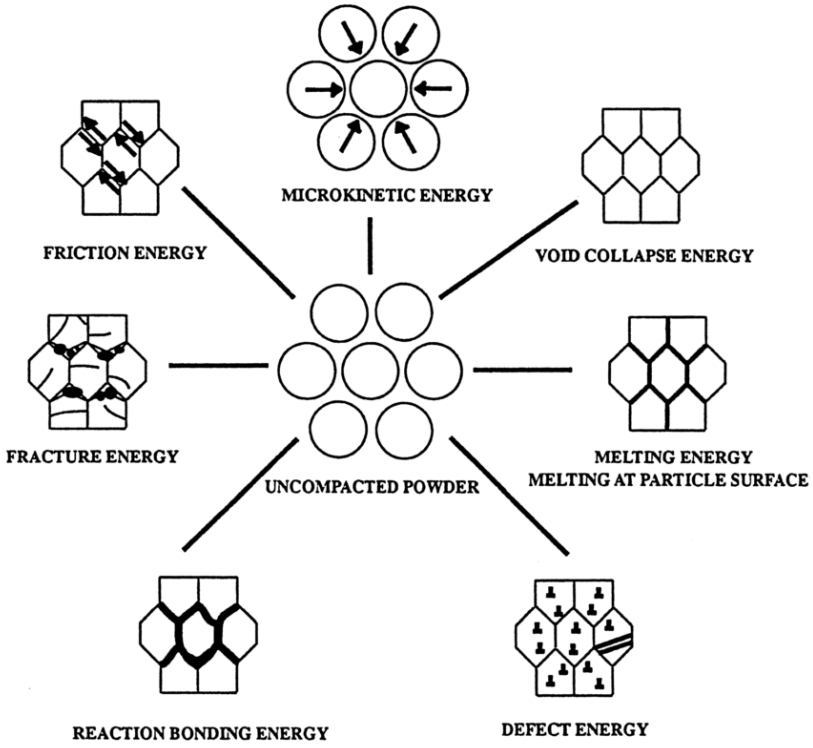

Figure 2.5. Energy deposition mechanisms during shock compaction [13].

Figure 2.5 graphically illustrates the most common mechanisms of energy deposition and localization in powder compaction. A brief description is given below:

a) Plastic deformation: For void collapse and consolidation to occur, significant plastic deformation must occur. Where greater deformation occurs, more energy will be deposited.
b) Microkinetic energy: Any kinetic energy that is beyond what is necessary for void collapse. Standard examples are viscous heating such as jetting and vorticity between particle surfaces.
c) Melting: At high enough shock pressures, it is known that a material can melt. Additionally, since the majority of energy deposited through rearrangement is localized

to the particle surface or ‘skin’ localized regions can experience melting [14]. This acts as an energy sink due to the latent heat of melting.

d) Defect energy: The passage of a shockwave introduces a significant number of point, line, and interfacial defects.
e) Interparticle friction: As the powders rearrange and deform, significant friction occurs between the particle surfaces.
f) Fracture: In brittle materials, it is likely that the particles fracture during rearrangement. This can rapidly release strain energy in a local region.
g) Adiabatic gas compression: If a gas phase fills the powder voidspace, it may become trapped. This results in adiabatic compression of the gas to very high pressure. At timescales conducive to heat transfer, this energy is then deposited into the matrix material and can result in poorly formed final materials [15].

An understanding of these mechanisms is critical to interpret impact experiments and know what physics are necessary for any modelling effort.

2.4 Experimental Techniques Relevant to Shock Synthesis

In order to study the behavior of materials under shock loading, methods had to be developed to controllably generate a shockwave and measure the response. Early work in shock synthesis relied on recovery experiments to infer whether reaction occurred as a result of shock loading [16]. However, this method does not indicate whether reaction occurs on the timescale of the shockwave or long after the passage of the shock as a result of residual heating. As a result time-resolved experiments were designed in order to measure the influence of reaction of the propagation of a shockwave. This is done by examining the powders Hugoniot response and comparing it to an inert powders response.

This section covers the experimental methods relevant to the proposed work. Section 2.4.1 details explosive compaction experiments that have been used to reach the pressures from 3-85 GPa [17]. Due to their simplicity and cost, these experiments can be used as a screening test to determine if synthesis of a high pressure phases is possible with the given reactive system. Additionally, this method would be used to produce greater quantities of material if this were to be scaled.

Section 2.4.2 details the methodology behind measuring an unknown materials Hugoniot through plate impact experiments. From this a material equation of state can be determined as well as inference of reaction. Light gas guns are typically used for these experiments; however, in the last 20 years laser driven flyer plate technology has matured to the point of being useful for shock physics [18,19]. The methodology described can be applied to all plate impact experiments and will be applied in the proposed experiments.

2.4.1 Explosive Compaction

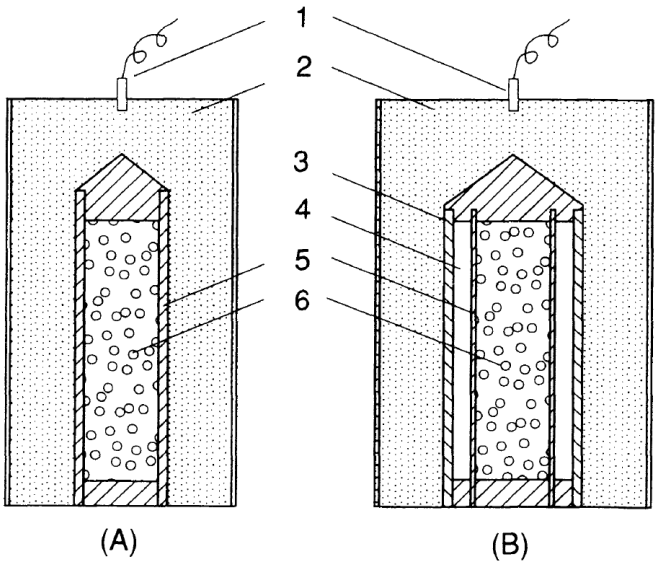

Figure 2.6 Cylindrical assembly for explosive compaction of powders with (A) single and (B) double wall configurations; 1) detonator, 2) explosive, 3) flyer, 4) air gap, 5) confiner, 6) powder.[20]

Figure 2.6. shows typical configurations for cylindrical compaction experiments. In both configurations an explosive is used to generate a shockwave that converges radially, compacting the powder. The powder can then be recovered in the capped assembly. Typically, low performance explosives provide better results. The lower shock velocity results in a longer push and higher velocity explosives can damage the recovery capsule.

The single walled configuration is simple to design, but delivers a triangular pulse. The peak pressure experienced by the powder can be increased by using a larger amount of explosives or an explosive with a higher detonation velocity [20]. Increasing the shock velocity

can result damage to the final compact and more pronounced Mach stem formation, seen in figure 2.7 (b) [21].

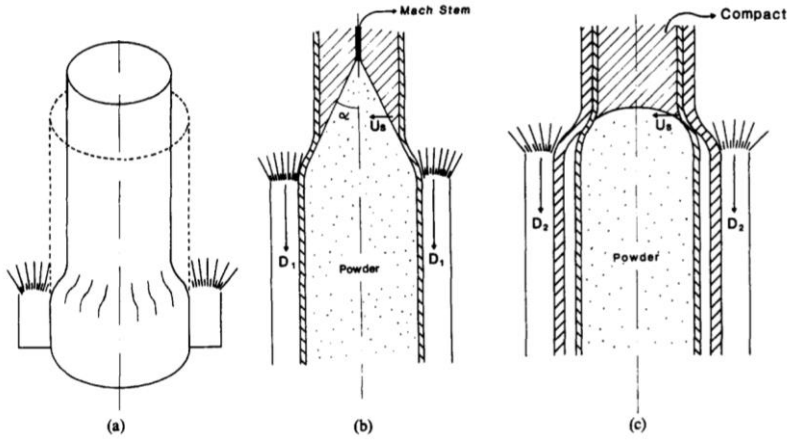

Figure 2.7. (a) Diagram showing deformation in single walled explosive compaction. (b) Diagram showing the formation of the Mach stem and velocity gradient in single walled experiment. (c) Deformation induced in double walled configuration [21].

Increased pressures can be achieved without the formation of a Mach stem with the double walled configuration seen in Fig 2.7 (c) [17,20,21]. The angle α seen in figure 2.7 (b) is correlated with the formation of the Mach stem. Smaller angle α results in a more pronounced Mach stem. The double cylinder experiment results in a more planar compaction since the detonation velocity will be much higher than the velocity that the of the flyer tube. It is important to note that the double walled experiment produces a square pulse of a controlled width, which may result in a longer duration at pressure when compared to the single walled experiment. Additionally, the double cylinder experiment was shown to generate much higher pressures than single wall experiments when used to compact Inconel 718 powders [21].

2.4.2 Plate Impact

The development of the light gas gun allowed high precision measurement of materials equations of state. In combination with two-stage and powder gas guns, impacting at predefined flyer velocities ranging from 30 m s^{-1} to 6 km s^{-1} allows investigations of material response up to 100's of GPa [17].

Figure 2.8 shows a standard configuration for plate impact of a thin specimen. In this configuration, a sample is mounted in electrical potting (epoxy) and lapped to a high level of parallelism. This is then directly mounted to the barrel of the gas gun in order to minimize tilt between the flyer plate and the target. The impact velocity is measured through either an electrical short or a break line (optical or thin wire). Flyer velocities have also been measured by using a magnetic flyer to induce a current in a coil around the barrel. A state of uniaxial strain is generated through inertial confinement. By maintaining a high diameter to thickness ratio (typically d/t = 5-10, but this can also be experimentally determined) release waves cannot reach the centerline of the sample. This maintains a state of uniaxial strain on the central axis, where all state measurements must be taken [17].

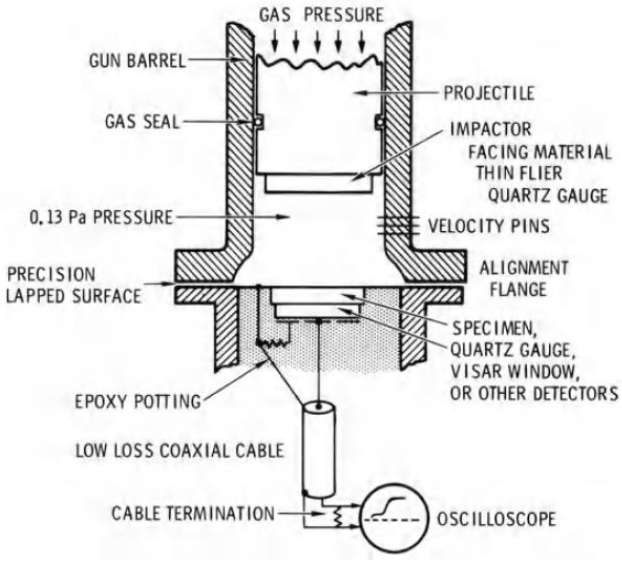

Figure 2.8. Standard experimental arrangement for plate impact experiment using a gas gun.

To set the state of the impacted material, it is necessary to measure two variables while under uniaxial strain. While this can be any pair of shock velocity, particle velocity, pressure, temperature, or density, there are many complications with measuring temperature and measurement of density would require a synchrotron x-ray source and phase contrast imaging. As a result, particle velocity, shock velocity and pressure are the most common measurements taken.

Time resolved measurement of the particle velocity can be achieved using laser diagnostics such as velocity interferometry for any reflective surface (VISAR) or photonic

Doppler velocimetry (PDV), these diagnostics require expensive equipment and are not necessary to measure a materials Hugoniot. Due to the geometry of the experiment, if the flyer plate is made from a well characterized material (copper for example) the flyer plate velocity can be used to determine the particle velocity in the sample through impedance matching. An example of this can be seen in Fig. 2.9 where material A is the donor (flyer) and material B is the accepter (target). The backward facing Hugoniot of the flyer would be centered at the point ($u_{flyer} = u_{0A}$, P = 0) in P-up space. The Rayleigh line for the target material is centered at the origin with a slope of $\rho_0 U_s$. If the shock velocity is measured experimentally, the intersection of the target materials Rayleigh line and the flyer materials Hugoniot in P-up space gives the particle velocity and pressure, setting a single point on the target materials Hugoniot. Repeated experiments at different flyer velocities allow the target materials Hugoniot to be fully characterized.

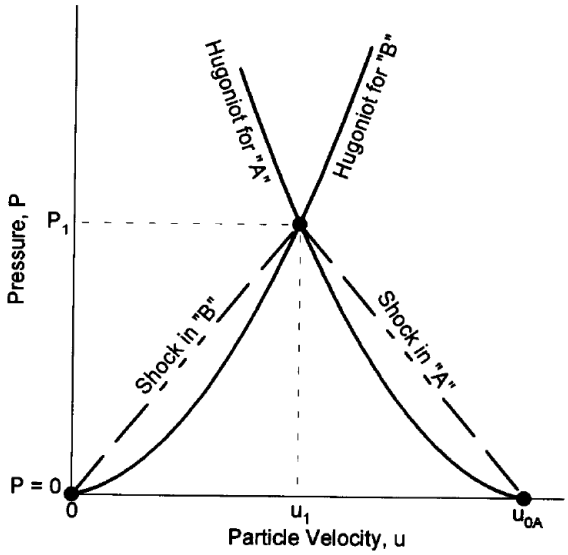

Figure 2.9. Impedance matching diagram for plate impact experiments with donor material A and target material B [22].

Conversely, pressure gauges can be used to establish pressure on the front or back surface. It is evident from Fig 2.9 that a similar method as what was used to determine the pressure with measurement of flyer velocity and shock velocity could be used to determine the shock velocity from measured values of pressure and flyer velocity. A more interesting approach is to provide pressure gauges on the front and back surfaces of the target material while measuring the flyer velocity. With a known distance between the pressure gauges, the shock velocity, pressure and

flyer plate velocity could be independently measured. Impedance matching would then provide multiple ways of validating the measurements taken.

2.5 Impact Initiation of Intermetallic Reaction

The first time resolved evidence of reaction on the timescale of a shockwave was done by Batsanov et al. [23] in 1987. In this work, powders of Sn and S with particle sizes of 5-10 μm were mixed at an equimolar ratio and compared to SnS powders. The samples were explosively loaded and manganin pressure gauges were used to determine the shock pressures. The key results from this experiment is shown in Fig. 2.10. The shocked Sn+S exhibits a deviation from the calculated inert Hugoniot.

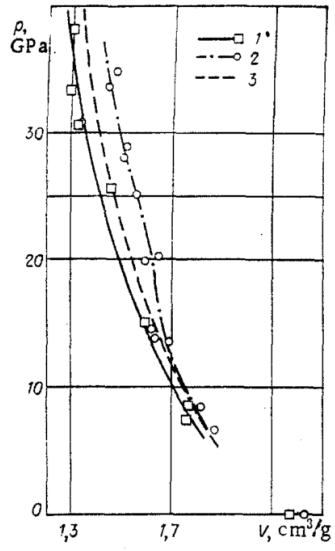

Figure 2.10. Shock Hugoniot measured by manganin pressure gauges for 1) SnS, 2) physically mixed Sn+S, and 3) calculated inert mixture of Sn and S. Note the deviation in the physically mixed Sn+S above 15 GPa.

The work on Sn+S illustrates the primary method of inferring reaction on the timescale of a shockwave. Since the reactions observed are highly exothermic (ΔH_0 = 727 kJ/kg in the case of Sn+S), there is an increase in specific volume due to a thermal back pressure when reaction occurs. Divergence of this kind in P-v space can be indicative of many different first order phase transitions [3,24]. Particularly, polymorphic phase transformations exhibit a volume contraction

deviate to a lower volume point (left on P-v plot above). It is important to note that this behavior has been observed in several binary intermetallic systems at pressures where there are no first order phase transitions present [23,25,26].

This particular discovery led researchers to distinguish two separate modes of reaction for shock loaded metallothermic reactions [4,16]. When a reaction occurs as a result of impact on the timescale of pressure equilibration (the ns-μs timescale) or exhibits a response similar to figure 2.10, the reaction is referred to as being 'shock induced.' If an impacted material reacts after pressure equilibration (on the order of several ms) as a result of thermal heating from compaction it is referred to as having been 'shock assisted.'

A general theory explaining why a material reacts in either mode is yet to be discovered; however, Graham's CONMAH model (CONfiguration, Mixing, Activation, and Heating) [27] conceptually details the necessary steps that are required for shock induced reaction to occur. The description is divided into 3 separate stages: the initial configuration, the transition or compaction zone (shock rise), and the compressed configuration after release. The initial configuration greatly effects energy localization through the particle morphology and peak shock pressure due to initial density; however, the CONMAH model deals primarily with what occurs during the transition zone. During the transition zone the configuration of the material is drastically altered through plastic flow and mixing through vorticity and jetting in the powder voidspace during pore collapse. Further plastic deformation at interfacial regions results in generation of large defect densities as well as introducing fresh material contact, activating the material. The bulk heating generated during this process and the mechanisms by which they are localized may then be sufficient to ignite the material. The degree by which these processes occur are thought to govern the mode by which reaction occurs.

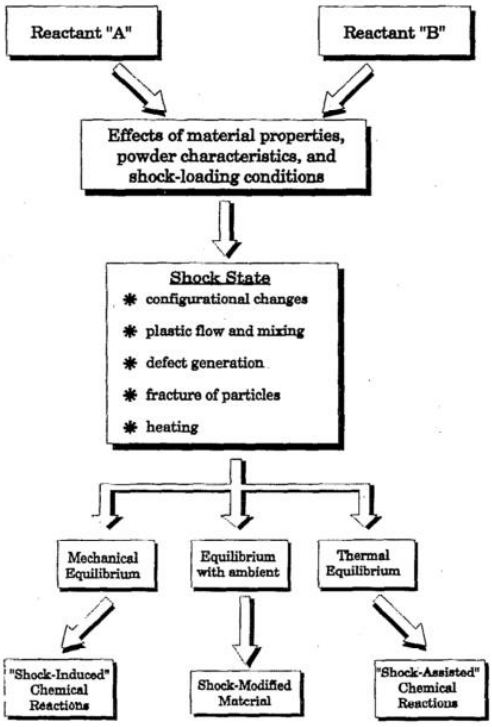

Figure 2.11. Schematic representation of Graham's CONMAH model *[28]*.

Due to the difficulty of studying the transition region experimentally, shock induced reactions have been primarily studied by varying the initial configuration. There have been a significant number of papers that study the effect of particle morphology on shock induced reactions [29–31]. Work on the titanium-silicon system (Fig 2.12) was the first to show the effect of particle size on shock induced reaction. In this work, coarse (Si = 45-149 μm, Ti = 105-149 μm), medium (Si, Ti = 10-44 μm) and fine (Si < 10 μm, Ti = 1-3 μm) physical mixtures of powder where shocked using an explosively driven flyer and manganin pressure gauges. As it can be seen, the medium sized powders appear to exhibit a shock induced reaction at pressures above 1.5 GPa. This work clearly illustrate that the material response cannot be predetermined by thermochemical behavior alone and that the behavior is highly dependent on the crush-up response of the powders. It has been observed that reduced diffusion distances increase the likelihood of shock induced reactions. Reeves et al. [31] showed that nanoparticle mixtures of Ni and Al exhibited reaction on the timescale of compaction.

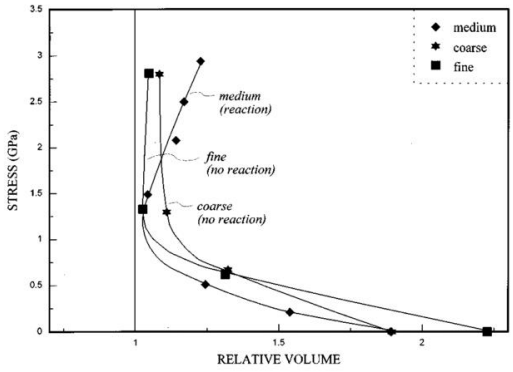

Figure 2.12. Effect of particle size on the impact response of the 5Ti+3Si system. Note that all particle sizes are 1-200 μm, so the effect of oxide thickness on all particles should be comparable.

Several papers have shown that by altering the aspect ratio (such as using flake Al instead of spherical Al) of the constituents in the Ni-Al system can result in shock induced reactions at lower pressures [30,32,33]. This supports the intuitive conclusion that promoting mixing due to deformation results in reaction on a shorter timescale.

The observation that reduced diffusion distances increased the likelihood of shock induced reaction led to the investigation of composite particles to study shock initiation [26,31,34–36]. This work has led to mixed results. The work by Xu and Thadhani [26] indicated that increased milling results in a loss of exothermicity, resulting in a less pronounced shock induced response in the ball milled Ni-Ti system. The loss in exothermicity suggests prereaction during milling; however, it was also suggested that the significant strain hardening resulting from milling altered the crush-up response of the powder. Anvil-on-rod impact of ball milled Ni-Al performed in the same research group showed that HEBM resulted in a minimum impact velocity for ignition at an intermediate milling time, with higher thresholds at longer and shorter milling durations.

Work on HEBM Ni-Al using the Asay shear test [35,36] has suggested that HEBM may inhibit shock induced reactions, but promotes shock assisted reaction. It has been seen that nanopowder mixtures of Ni-Al begin to exhibit rapid reaction at impact velocities near 800 m s^{-1}, while HEBM powders are not seen to exhibit this behavior at impact velocities up to 1000 m s^{-1} [35]. Work at lower impact velocities showed that HEBM powders reacted with a shorter ignition delay with increased ball milling times [36].

2.6 Shock Synthesis of High Pressure Phases

Shock synthesis is the process by which a material is impacted at high velocity resulting in chemical reaction and synthesis of a desired product phase [16]. This method of synthesis can result in fully dense compacts of high hardness materials (metals and ceramics) as well as potentially create novel materials through chemical reactions at extreme pressure and temperature. The previous section (2.7) discussed research on the mechanisms of shock induced reaction. This section discusses the application of shock induced reactions to synthesize materials.

The most common application of shock synthesis is production of fully dense binary intermetallics. Many efforts have led to the synthesis of carbides, borides, aluminides and silicides [16]; however, there have not been a significant number of works that produce novel materials or methods of synthesis. Efforts to synthesize novel materials have focused on producing materials that are incredibly hard, such as cubic boron nitride (c-BN) or the suspected β-carbonitride (β-C_3N_4).

Shock induced polymorphic phase transformations can be utilized to recover a metastable material that has unique or desirable material properties, such as high hardness. The most commercially successful examples of this are the explosive synthesis of diamond [37] and c-BN [38,39]. By explosively shocking graphite, the hexagonal form of carbon, nano-diamond can be recovered. This process has been used extensively to produce commercial abrasives. A similar process can result in the formation of high pressure phases of BN; however, it is not as straight forward as diamond synthesis.

BN is isoelectronic with C, meaning that they share valency and bonding structures (i.e. it forms the same crystal structures). Several of the more common polymorphs of BN are presented in Fig. 2.13. There is some debate as to whether the most stable form of BN at atmospheric conditions is h-BN, the graphite like phase, or c-BN, which is the diamond-like phase [40]; however, bulk synthesis techniques under atmospheric conditions are most likely to produce h-BN. The phase diagram in Fig. 2.14 shows the high pressure behavior of BN. At high pressure and temperature the c-BN phase becomes the preferable phase. Additionally, the wurtzitic phase of BN (w-BN) forms preferentially at high pressure and lower temperatures [39] and is structurally similar to lonsdaleite. Both c-BN and w-BN exhibit sp^3 bonding, which contributes to the predicted hardness of both phases.

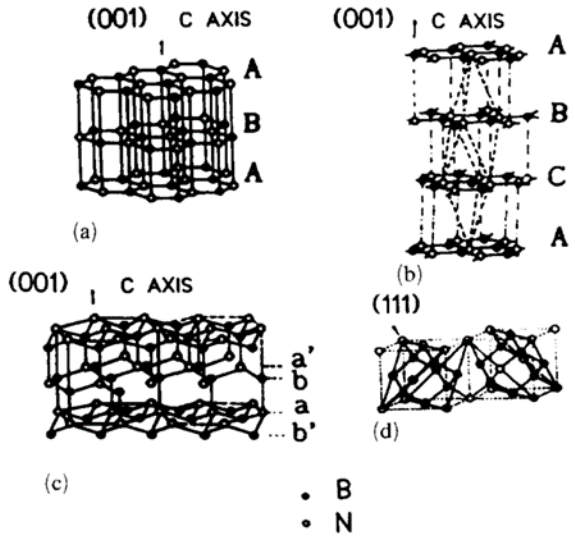

Figure 2.13. Several common BN crystal structures: (a) h-BN; (b) r-BN; (c) w-BN; (d) c-BN.

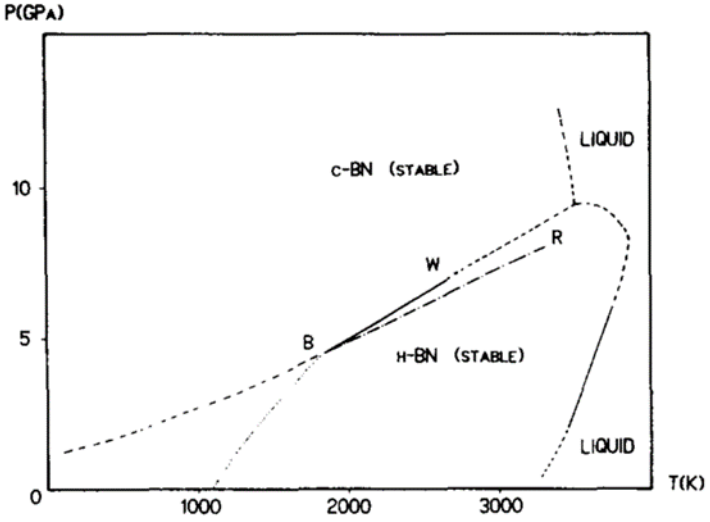

Figure 2.14. The boron nitride P-T phase diagram *[39]*. Line B-W represents the Bundy-Wentorf equilibrium line *[41]*, while B-R is the equilibrium line as corrected by Rapoport *[42]*.

A significant amount of research has been done in Japan on the behavior of BN under explosive loading [14,43–47]. Single shock loading of h-BN was shown to result in the formation of w-BN in Soma et al. at pressures up to 55 GPa [44] without formation of c-BN. Contrary to this, plate impact experiments by Coleburn and Forbes [48] measured a discontinuity in the P-v Hugoniot for h-BN near 12 GPa, and were able to recover a mixture of c-BN and w-BN. Unfortunately, Soma et al. did not reconcile their results with Coleburn and Forbes. From

reading their papers, the samples used by Soma et al. were hot pressed to near full density at a 1:20 ratio of h-BN to Cu in an effort to rapidly quench the shocked BN while Coleburn and Forbes used nearly fully dense pure h-BN. It is suggested that the material used by Soma et al. did not reach as high of a temperature state when compared to Coleburn and Forbes.

Further work from the Japanese group showed that under multiple shock loadings, h-BN can be driven from purely h-BN, seen in Fig. 2.15 (A), to a mixture of h-BN and w-BN, seen in Fig. 2.15 (B), and finally a mixture of phases including w-BN and c-BN, Fig. 2.15 (C, D). The XRD traces in Fig. 2.15 (C, D) shows peaks that are labelled with a 'u.' These peaks are suggested to be the so called explosive or E-phase of BN. The structure and existence of this phase is still debated [49–52]. Some researchers have even suggested that E-BN is of a fullerene-like structure [50]. While this structure was first reported through explosive compaction of h-BN [53], hence its designation as the explosive phase, it is not currently thought to be a high-pressure phase, since it has been produced by several different methods at atmospheric pressure [52,54]. This phase illustrates the complexity of BN and the difficulty in identifying its structure.

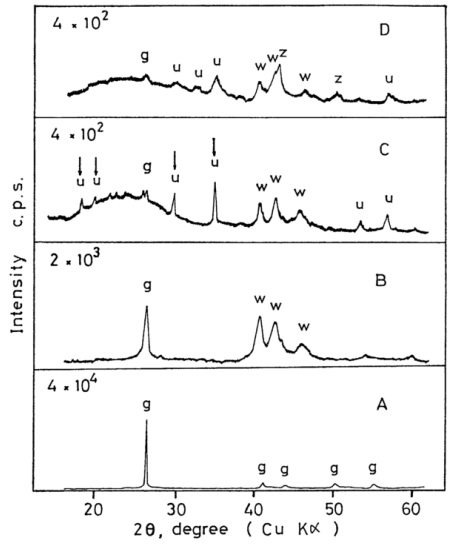

Figure 2.15. XRD of multiple shock loading of BN, with A being the initial material and B-D measurements taken after succesive shock loading. g: h-BN; w: w-BN; z: c-BN; u: unknown.

Shock synthesis of c-BN is not straightforward. Typically, the conversion is low and the use of a quench material (Cu) is required [44,48]; however, the fact that it is a commercially relevant

high pressure phase makes it an interesting candidate for shock induced reaction synthesis. There have been few attempts to directly synthesize high pressure polymorphs through reactive synthesis [55,56]. Liepins et al. [55] reports direct synthesis of a thin sheet of c-BN by explosively shocking ammonia borane (NH_3BH_3). The paper is limited in details, with only a small amount of material recovered and an X-ray microprobe diffraction measurement showing a lattice spacing of 3.655 Å compared to the 3.616 Å standard as the only justification of c-BN being synthesized. Forward referencing of this work shows no evidence of further work. Collins et al. [56] attempted synthesis of beta carbonitride (β-C_3N_4), a hypothetical phase of carbonitride predicted have hardness comparable to diamond, via shock loading of a mixture sodium dicyanamide ($NaN(CN)_2$), carbon tetra-iodide (CI_4) and sodium azide (NaN_3). IR spectra and TEM characterization was used to show that sp^3 bonding was present and the atomic ratios were appropriate for carbonitride formation; however, it was not conclusive that β-C_3N_4 was formed.

CHAPTER 3. THE ROLE OF FRACTURE IN THE IMPACT INITIATION OF NI-AL INTERMETALLIC COMPOSITE REACTIVES DURING DYNAMIC LOADING

3.1 Introduction

A complete understanding of the initiation of intermetallic reactions under impact loading is lacking. These materials are often highly heterogeneous, with length scales relevant to initiation spanning from millimeters to nanometers. Specifically, the microstructure of composite particles affects the mechanical response as well as the timescale for atomic diffusion. Under identical loading, reactions can be initiated on the μs timescale or not at all due solely to the microstructure [25,30,31,35,57–59]. Likewise, the difference in mechanical properties could possibly result in two materials with identical compositions and thermal ignition temperatures responding differently to impact. This has not been fully explored in past work.

The Ni-Al system has been used extensively to study metallothermic reactions under impact loading as well as for use as a structural energetic material [16,31,33,36,60,61]. By reducing the characteristic diffusion length, intermetallic reactions can occur on the timescale of a shockwave [31]. The current understanding is that prompt reactions on the μs timescale result primarily from mechanical mixing [4,16]. Additionally, understanding of reactions under high-rate loading could lead to new methods of materials synthesis by utilizing reactive pathways at high pressure to avoid energy barriers present in different methods of synthesis [4]. Since the Ni-Al system is well characterized, it provides an ideal system to study the effect of mechanical properties and microstructure on impact initiation.

High energy ball milling (HEBM), a process by which lamellar composite particles can be produced from ductile powder mixtures, has been used to create composite Ni-Al particles with significantly lower thermal ignition temperatures (230°C) than microscale powder mixtures (660°C) [62]. Efforts to use HEBM to increase the sensitivity of the Ni-Al system to impact has yielded mixed results. It has been suggested that producing composite particles through HEBM induces significant strain hardening, resulting in a higher impact velocity necessary for initiation [26,34]. Reeves et al. [35] showed that under identical impact loading, a physical mixture of nanopowder Ni-Al reacted on the μs timescale while similar HEBM Ni-Al composites reacted on

the ms timescale. Other work suggests that HEBM can reduce the ignition delay of the Ni-Al system in response to impact when reaction occurs long after pressure relaxation [36]. These studies suggest that composite particles inhibit prompt reaction under impact loading, even though they have lower thermal ignition temperatures.

Alternatively, magnetron sputtering has become a useful method to produce and study intermetallic reactives and thermites [63]. By alternating sputtering targets, this method can yield Ni-Al nanolaminate (NL) materials with a highly controlled microstructure compared to HEBM composites. As such, the mechanical hardness of the NL reactive composite can be controlled by altering the layer thickness due in part to the Hall-Petch effect [64], limiting the amount of plastic deformation during fracture and significantly reducing fracture toughness. This method can be utilized to produce NL composite powders with a propensity to fracture and ignition temperatures matched to an equivalent HEBM system, allowing investigation of the role fracture plays in impact initiation. Further, they are an attractive system for simulation or experimentation because the nanostructured laminate is uniform compared to HEBM composites.

The objective of this study is to experimentally investigate the role of fracture as a mechanism for impact driven reaction. This was done by comparing the ignition of chemically similar systems of HEBM and NL Ni-Al powders via impact. The thermal and mechanical properties of both powders are characterized in order to explain why the NL Ni-Al powder reacts on the μs timescale while the HEBM Ni-Al powder reacts on the ms timescale. It is suggested that fracture and interparticle friction are key to understanding not only the difference between these two materials, but initiation due to impact.

3.2 Experimental Methods

Multilayer Ni-Al nanolaminates were purchased from Indium Corporation with an average composition of $Al_{50}Ni_{46}V_4$. The materials were ordered to not contain the typical InCuSil brazing layer and were received in 23 x 19 cm sheets with an 80 μm thickness and 50 nm bilayer spacing (total thickness of 1 layer of Al and 1 layer of Ni). The sheets were cut into pieces of approximately 0.25 g and ground into millimeter scale particles using a mortar and pestle. The material was then milled for 20 hours (h) on a roller mill using 6.35 mm diameter 440C steel balls. The milling container was 50 mm in length, 25 mm in diameter and capped with PTFE. A ball to powder mass

ratio of 50:1 was used at a speed of 300 revolutions per minute (rpm). After the initial 20 h milling increment, the NL particles were sieved into separate batches of particle diameter, d>53 μm and d<53 μm. The larger particles were placed back in the mill and milled for additional periods of 5 h at the same crash ratio and rate. This process was repeated for up to 3 additional 5 h increments or an additional 15 h of milling.

Equimolar Ni-Al milled composite particles were produced using a Retsch PM100 planetary ball mill. Nickel (3-7 μm, 99.9% metals basis, Alfa Aesar) and aluminum (-325 mesh, 99.5% metals basis, Alfa Aesar) powders were milled in a two-stage process. In the first stage, the materials were dry milled in three 5 min increments with 15 min rest times followed by a 2 min increment resulting in a total milling time of 17 min. This is the critical milling time, where any further milling resulted in reactions during milling. In the second stage, the material was wet milled in 20 ml of hexanes for a total milling time of 10 min in 5 min increments with 15 min rest times in order to reduce the particle size. The milling media was 440C steel balls with a diameter of 9.5 mm at a 5:1 ball to powder mass ratio. After milling, the powders were allowed to dry for 20 h at near vacuum conditions. The powders were sieved into two separate batches, 25<d<53 μm and d<25 μm, and mixed at a 7:3 mass ratio respectively to match the as sieved mass distribution of the NL powder.

Powder morphologies and microstructures were characterized scanning electron microscopy (SEM, FEI NOVA nanoSEM) and scanning transmission electron microscopy (STEM, FEI Magellan 400). Additionally, x-ray diffraction (XRD) was performed using a Bruker D8 diffractometer to evaluate whether significant reaction occurred as a result of milling and to determine final product formation after impact

The effect of milling on the heat release of the HEBM and NL Ni-Al powders was investigated through differential scanning calorimetry (DSC, TA Instruments Q600). Approximately 15 mg samples were placed in alumina pans and heated at 10°C/min from 50-1000°C in a 100 ml/min flow of ultra-high purity argon.

The Asay shear experiment as presented in Fig. 3.1 has been used to study impact initiation of several energetic formulations [31,35,36,65]. For each trial, 1.75 g of powder was poured into an assembled sample holder with a 2 mm by 20 mm cross sectional area and quartz viewing window. A steel plunger was then inserted into the holder and the powder was tapped to a final density. A light gas gun was then used to launch a steel flyer plate backed by a Delrin® sabot at

approximately 130 m s^{-1}, impacting the plunger and transmitting a planar compaction wave into the powder.

The impact event was monitored using a Phantom v7.3 high speed camera at approximately 50000 and 220000 frames per second (fps) with an exposure of 1 µs, while the target was illuminated by a xenon arc lamp. Streak image analysis of the captured images allowed measurement of the compaction wave and particle velocities as well as the reaction front propagation rate.

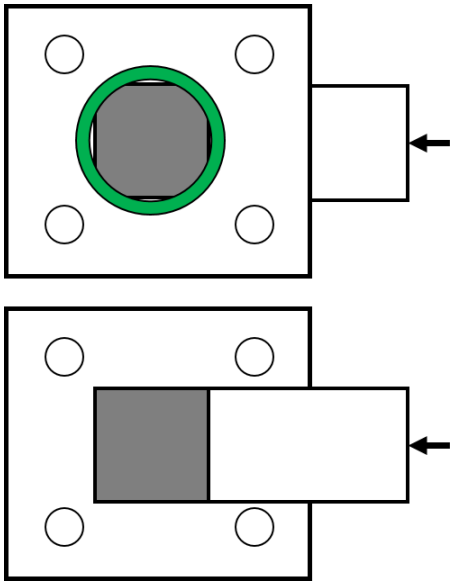

Figure 3.1. Diagram of Asay shear experiment. Top: Full assembly with quartz window and Turcite® retainer. Bottom: Assembly with window removed showing square powder compact in contact with plunger.

The sensitivity of the powders to friction was measured using a BAM friction tester. In the BAM apparatus, a sample is ground between a ceramic pin and disc. The normal force is adjusted by varying the weight applied. This provided the 50% probability threshold for reaction with a 90% confidence interval as evaluated using Neyer statistics [66]. Microindentation was performed on individual particles suspended in an acrylic based epoxy in order to measure composite hardness. The samples were polished up to a 0.05 µm diamond solution to provide an even surface for indentation.

3.3 Results and Discussion

3.3.1 Morphology and Microstructure

SEM illustrating representative particle morphology for both HEBM and NL Ni-Al can be seen in Fig. 3.2(a,b) with Fig. 3.2(c,d) showing unique morphology indicative of brittle failure found in the NL material. The overall shape of both powders were plate-like with the NL Ni-Al having sharper features compared to the HEBM Ni-Al. The microstructures of both powders imaged using SEM and STEM are presented in Fig. 3.3. A detailed characterization of the microstructure of the HEBM Ni-Al can also be found in Manukyan et al. [62] as well as a similar system characterized through nanotomagraphy [67]. It is evident from Fig. 3 that both powders have nano-scale features. The HEBM Ni-Al is composed of a lamellar microstructure, with typical individual phase layer thicknesses varying from 30-200 nm throughout the particle. SEM of the NL powder indicates that the milling process did not appreciably alter the microstructure from the original material. The microstructure remains highly ordered with an average bilayer thickness of approximately 50 nm. Both systems have intimate contact between the Ni and Al layers without the diffusion barriers present in physical mixtures of discrete particle mixtures (e.g. oxide layers and voids). XRD performed on both the NL and HEBM milled powders indicated no evidence of pre-reaction, as presented in Fig. 3.4.

For the Ni-Al system, it is unknown whether the impact driven initiation is governed by the smallest length scales or the average diffusion distance. Previous work on solid explosives suggest that for impact initiation, hot spot sizes on the order of 10's to 100's of μm [12] are needed to sustain a reaction. While the properties and behavior of intermetallic composites differ greatly from explosives, it would be reasonable to expect the critical hot spot sizes to be comparable. If the critical hot spot size for ignition in an intermetallic system is significantly larger than the minimum length scales, then initiation would be expected to be governed by the average atomic diffusion distance. This would suggest that the HEBM and NL Ni-Al could behave differently solely as a result of the microstructure.

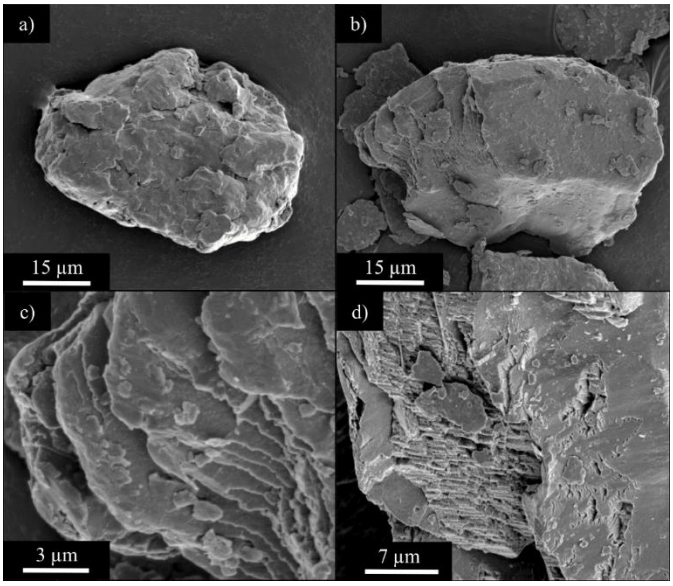

Figure 3.2. SEM images showing typical particles for a) HEBM Ni-Al and b) NL Ni-Al. (c,d) Unique features indicative of brittle failure in the NL Ni-Al after milling.

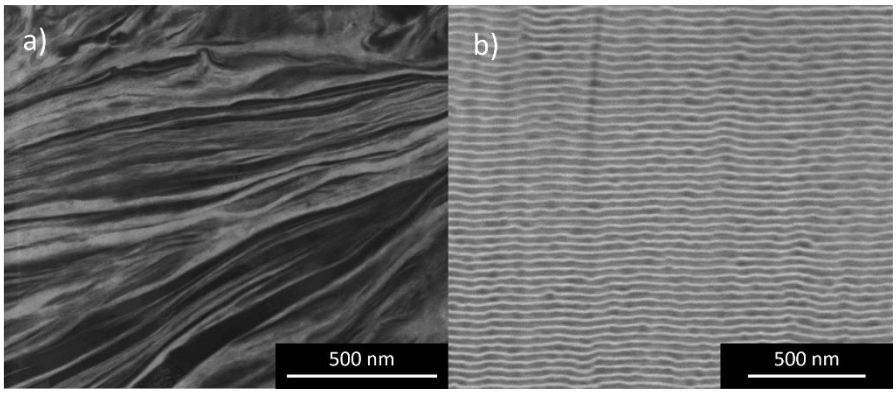

Figure 3.3. a) STEM of HEBM Ni-Al b) SEM of FIB cross-section of milled NL tilted at 45° with respect to the horizontal.

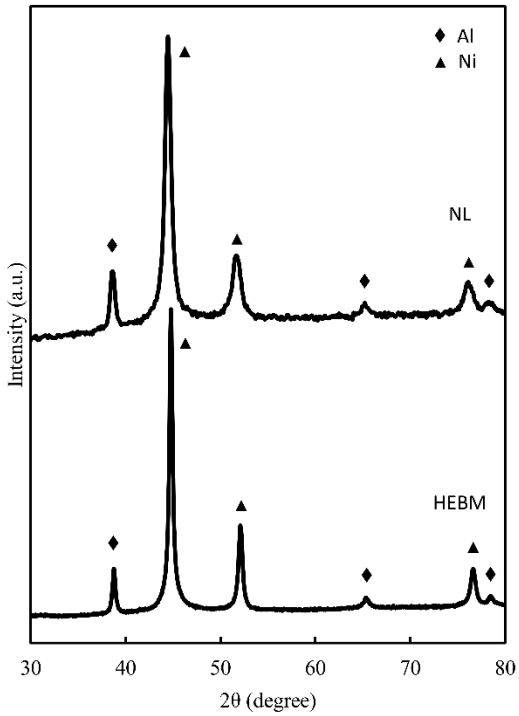

Figure 3.4. Only Ni and Al peaks observed in XRD of the NL and HEBM Ni-Al powders.

3.3.2 Impact Experiment

To study the response of the powders to high-rate impact loading, impact experiments were performed using the Asay shear experiment with a flat faced plunger. A summary of the experimental trials and values of impact velocity, relative density, shock velocity, particle velocity, burning rate and ignition delay is presented in Table 3.1. The reported pressure was estimated from the measured compaction wave speed and particle velocities using the Rankine-Hugoniot jump relations. It should be noted that the burning rate was reported relative to the particle velocity and is not an absolute velocity.

Select frames of the high-speed imaging at 50000 fps of the NL and HEBM Ni-Al powders in response to the impact stimulus of the Asay shear test is presented in Fig. 3.5. The difference in the response of the two materials to identical loading conditions is distinct, and the large difference in the timescales of reaction should be noted. In the HEBM material, the compaction progresses through the sample without any evidence of significant reaction occurring near the compaction front; however, an initial bright zone was observed near the plunger face.

Approximately 12 ms after impact, a low luminosity reaction wave propagates through the sample from the bright zone at a velocity of approximately 20 cm s^{-1}. This result is similar to previous studies of HEBM Ni-Al impacted at higher initial density [36], as well as propagating at a similar velocity to compacts ignited thermally [68]. XRD performed on the recovered compacts, presented in Fig. 3.7, indicate complete conversion to NiAl and was found to be independent of location within the compact.

When the experiment was conducted without external illumination a separate reaction front was observed preceding the reaction wave previously noted. This wave traveled at the same speed as the previously observed reaction front. It is unlikely that the second front is due to oxidation since there were no oxide peaks present in post-impact XRD. It is suggested that the two fronts could indicate a two-step reaction process as proposed in Gunduz et al. [69] and Justice et al. [70].

Table 3.1. Summary of impact experiments.

	Material	Impact Velocity (m/s)	%TMD	Wave Velocity (m/s)	Particle Velocity (m/s)	Estimated Pressure (MPa)	Burn Rate (cm/s)	Ignition Delay (ms)
1	HEBM	133	41%	266	---	---	18	12
2	HEBM	135	38%	257	---	---	23	5
3	HEBM	127	44%	264	---	---	16	8
4	NL	130	40%	263	78	43	1.8×10^4,* 20-50**	0.017
5	HEBM	132	45%	260	80	43	23	12
6	NL	128	49%	250	78	50	1.7×10^4 *	0.018

*Burning rate measured relative to plunger velocity.

**Burning rate varies over hot spots.

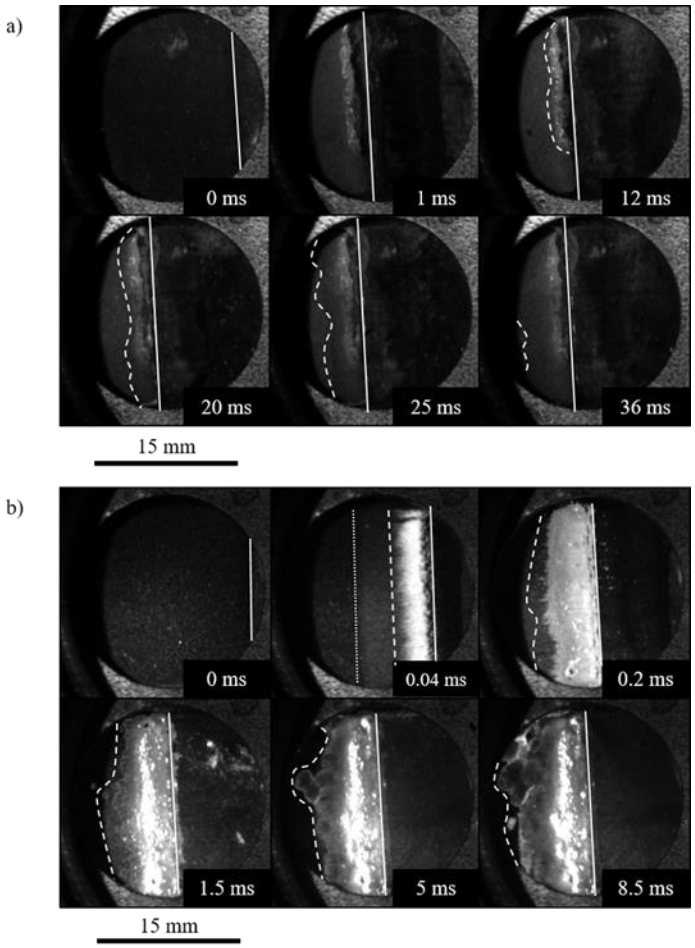

Figure 3.5. Image sequences comparing the impact response of the a) HEBM and b) NL Ni-Al powders with the plunger, compaction front and reaction front traced out by the solid, dotted, and dashed lines respectively at 50000 fps. Note the difference in the reaction timescale. The BM powder reacts on the ms timescale through a thermal propagation while the NL powder reacts on the μs timescale before transitioning to a similar thermal propagation.

Streak imaging analysis, taken at 220000 fps, was used to further study the behavior of the initial compaction, and selected results for the HEBM and NL Ni-Al are presented in Fig. 3.6. The compaction wave propagates from the plane of impact at a constant velocity until it reflects from the back of the sample holder which is obscured by a shadow. The particle velocities were measured by tracking speckles in the compacted material. As presented in Fig. 3.6, it is evident that both the compaction wave and particle velocity were constant, indicating steady and uniform loading.

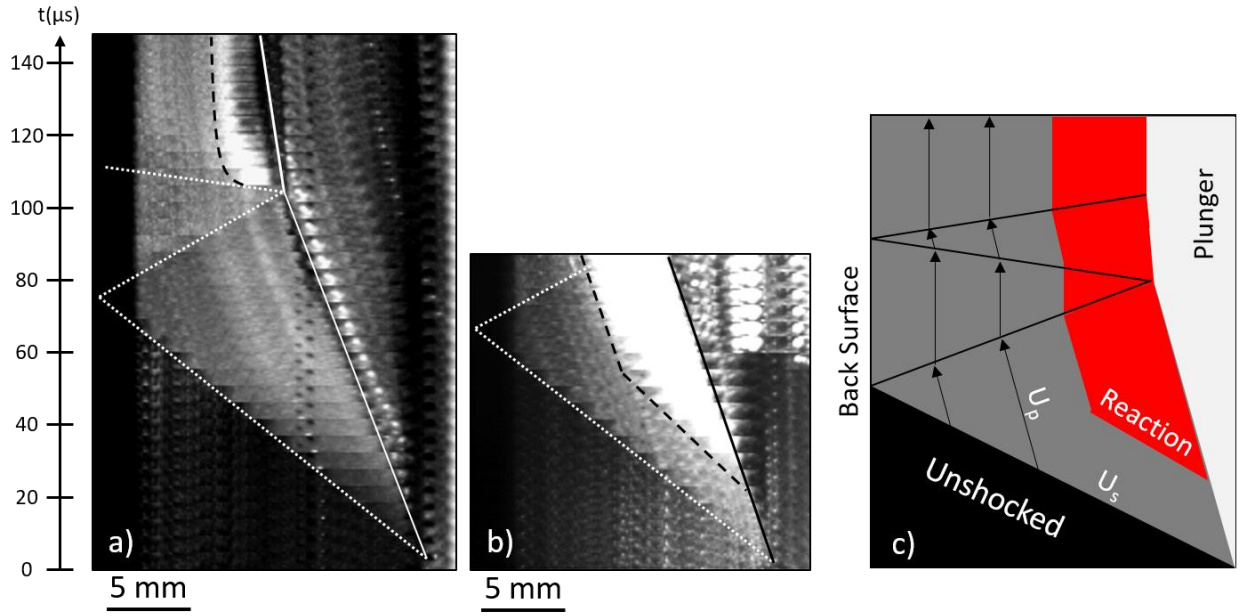

Figure 3.6. This pair of streak images taken at 220000 fps presents the reaction process in much more detail. The plunger, compaction front and reaction front traced out by the solid, dotted, and dashed lines respectively. a) HEBM powder is observed to briefly react when the compaction wave reflects off of the back of the sample holder and then off the plunger. b) The NL powder reacts and travels with the initial passage of the compaction wave. c) The schematic shows where the compaction wave velocity (U_s) and particle velocity (U_p) were measured as well as the zone where reaction is observed.

From the streak imaging analysis, the velocity of the compaction wave in the HEBM powder was measured to be approximately 260 m s^{-1} for a nominal impact velocity of 130 m s^{-1}. A bright zone of reaction was observed in the material near the plunger face after the reflected compaction wave reached the plunger. This reaction was limited to a small region near the plunger face and appeared to quench. It should be noted that this reaction was not the result of the initial passage of the compaction wave, but due to the reflected leading wave off of the plunger face. It is suggested that the initial compaction wave preheats the HEBM Ni-Al such that the additional plastic deformation caused by the returning wave is enough to initiate reaction locally. This reaction was short lived, and stalled for 12 ms before the slow reaction mode propagated from that point.

In contrast to the HEBM Ni-Al, the response of the NL Ni-Al to the compaction front was immediate. As presented in the second frame of Fig. 3.5(b), the reaction front was observed to

follow the compaction front. The delay between the passage of the compaction wave and visible reaction was 17 μs. This ignition delay is *3 orders of magnitude lower* in the NL Ni-Al as compared to the HEBM Ni-Al. The reaction front follows the compaction wave for approximately 1 cm at which point the reaction front decouples from the compaction wave, slowing to a propagation rate that is on the order of 20-50 cm/s. After the experiment, it was observed that the quartz window had melted near the region where the prompt reaction occurred. This was not observed in the HEBM powders, or where low speed reactions were observed.

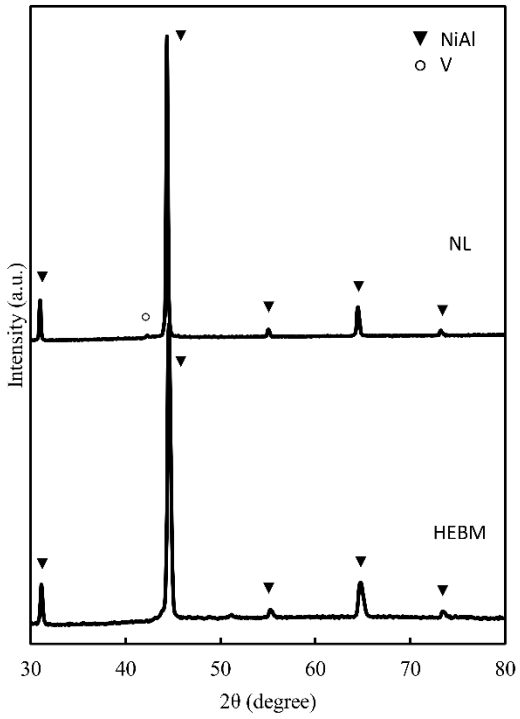

Figure 3.7. XRD of the post-impact material shows complete conversion to NiAl without the presence of oxides.

The streak imaging analysis of the NL material as presented in Fig. 3.6(b) indicates that the compaction wave and particle velocities were nearly identical to what was measured in the HEBM material. Initially the indicated reaction front propagated in the prompt reaction mode at a velocity equal to that of the compaction wave, but then transitioned to the slow reaction mode, decoupling from the compaction wave.

The response observed in the NL Ni-Al under impact is similar to observations of nanoparticle mixtures of Ni-Al [57]. Two distinct reaction modes are reported in such a system, a

prompt reaction mode and a slow reaction mode. The prompt reaction mode was observed in the nanoparticle mixtures at impact velocities no lower than 840 m s^{-1} and not observed in for the HEBM powders used in that study at velocities up to 940 m s^{-1} [35]. Comparatively, for the NL Ni-Al used in this study, the prompt reaction mode was observed at the far lower impact velocity of 130 m s^{-1}. Reeves et al. [35] suggested that the key difference between HEBM Ni-Al and nanopowder Ni-Al was the distribution of porosity in the two systems. Since the HEBM and NL powders are of equal size distributions with intimate contact between the reactants, this is not the case in this work.

The transition from the prompt reaction mode to the slow reaction mode is not well understood. In an ideal configuration the peak pressure would decay with the square of the distance travelled [5]. If the compaction wave were to broaden, then this could alter the heating rate and result in the observed transition in reaction rate. However, the constant particle and compaction wave velocities indicates that the compaction was fully supported and is supported by the observed movement of the plunger. This result suggests that the pressure is constant until the wave is reflected back. However, it's also possible that the leading edge of the front remains approximately the same while the remaining part of the wave evolves, which is consistent with the constant wave and particle speeds.

The Asay shear test as used in this study restricts motion perpendicular to the plunger and compaction wave through the use of a window. However, the window was observed to move once a significant load was placed upon it via the compaction wave, allowing the Ni-Al material to expand in the trans-axial direction. This phenomenon allows the reactive powder to rearrange without fracture or significant plastic deformation, and would mitigate the μs timescale reaction. The constant particle velocity measured is not readily explained through this suggestion; however, it appears to be the most likely cause for the transition from the rapid microsecond timescale reaction after initiation was observed in the NL Ni-Al system.

The results in Figures 5 and 6 clearly indicate that the NL and HEBM Ni-Al reactive systems with similar particle morphology and size distribution can react in highly disparate timescales under identical impact loading. It is suggested that the ability of the NL Ni-Al ability to fracture on impact is a key mechanism governing the microsecond timescale reaction. The ability to highly concentrate energy through fracture and friction on newly formed interfaces is not expected to be as dominant in the more ductile HEBM Ni-Al as compared to the NL Ni-Al. Deposition of enough

energy through fracture and friction at freshly formed interfaces would induce a thermal explosion at the locations of concentrated heating. In the bulk material, this mechanism would appear as a travelling reaction front occurring immediately behind the compaction wave.

3.4 Thermal Analysis

DSC was performed on the powders to investigate the effects of milling time on the NL Ni-Al. The representative heat release curves for 3 separate milling times can be presented in Figure 8(a). The results indicate no significant change in onset temperature or peak broadening with increased milling time; however, the heat of reaction was reduced from 120 J/g to 107 J/g with increased milling time. The microstructure of the milled NL Ni-Al as evaluated with SEM as well as the measured thermal response indicate the properties of the original foil were maintained throughout the milling process.

A comparison of the measured heat release of HEBM and NL Ni-Al powders as evaluated through DSC, presented in Fig. 8(b), shows that the NL Ni-Al had three distinct reaction peaks with an onset temperature of approximately 460 K, while the HEBM Ni-Al has three reaction peaks with the second and third overlapping and an onset temperature of approximately 450 K. Additionally, the ignition temperatures of the HEBM and NL Ni-Al were measured through hot plate ignition experiments to be approximately 555 K [62] and 525 K [71] respectively. The similarity in the ignition temperatures indicate that if the same temperature was reached on impact the materials would behave similarly.

The energy deposited through compaction (P-V work) as calculated from the initial and final states would lead to a temperature rise of only 25 K over the compact volume. Additionally, due to the low pressure induced via the impact, the majority of densification was likely a result of rearrangement, suggesting that the volume change of the solid is low. Consequently the average temperature rise of the compact should be insufficient to ignite the compact.

Due to the highly heterogeneous nature of the composite powders it is expected that many mechanical processes act to concentrate the energy to specific locations through the impact processes [10,11]. If the ignition temperature is conservatively assumed to be on the order of 250°C (this value would increase with heating rate [72]) the required heating rate to reach this

temperature in 1-10 μs would be 10^7-10^8 K s^{-1}. Heating rates of this order are achievable through dynamic friction and fracture [73].

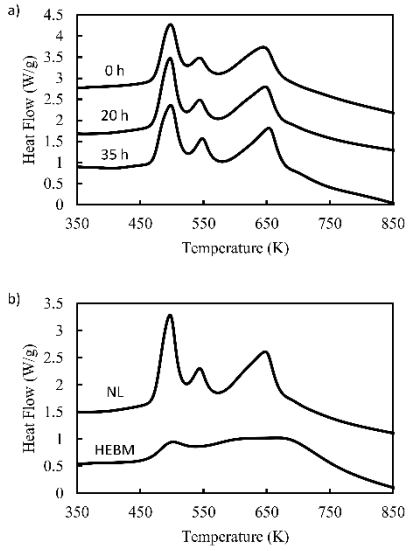

Figure 3.8. a) DSC traces of heat flow in neat (top), 20 h milled (middle), and 35 h milled (bottom) foils. b) DSC traces of HEBM and NL powders at 10°C/min heating rate.

3.5 Mechanical Characterization

To evaluate the mechanical properties of the composite particles, microindentation was performed on the HEBM and NL Ni-Al powders. The HEBM Ni-Al and NL Ni-Al had measured hardnesses of 2.2 ± 0.2 GPa and 4.3 ± 0.9 GPa respectively. Tabor's relation H ~ 3Y, where H is the Vickers hardness and Y is the materials yield strength, allows estimation of a metals yield strength from indentation hardness [74]. The yield strength of the particles can be approximated as 0.7 GPa and 1.4 GPa for the HEBM and NL Ni-Al powders respectively.

The maximum contact pressure, p, experienced between two particles as approximated using assuming Hertzian contact is,

$$p = \frac{1}{\pi}\left(\frac{12FE'^2}{R^2}\right)^{\frac{1}{3}}, \tag{3.1}$$

$$E' = \frac{E}{2(1-\upsilon^2)}, \tag{3.2}$$

where E is the elastic modulus, υ is Poisson's ratio, F is the applied load, and R is the radius of the two particles. Using a volume averaged elastic modulus and 50 μm particles, the peak pressure experienced during impact would be significantly greater than the local yield strength of either the NL or HEBM material. Comparing the yield strength of the HEBM and NL Ni-Al composite particles with the estimated bulk pressure suggests that there was limited bulk plastic deformation during compaction; however, localized deformation is still expected at particle contacts.

It was observed that the HEBM Ni-Al could be statically pressed to form a compact, while the NL Ni-AL powders fell apart after compaction. The ability to form a compact from the HEBM indicates that it is much easier to deform HEBM Ni-Al at particle junctions than the NL Ni-Al. This suggests the possibility of the HEBM Ni-Al yielding locally to reach the increased density during impact. Studies have shown that Ni-Al NL exhibit minimal plastic deformation [75]. Additionally, the increased hardness of the NL Ni-Al as compared to the HEBM Ni-Al would result in the NL Ni-Al having a reduced fracture toughness. Due to the limited amount of deformation in the NL powders, the heating resulting from plastic deformation would be minimal and the particles would likely fracture during rearrangement. This would increase the total area experiencing frictional loading and rapidly releasing energy in highly localized spots.

Considering that interparticle friction is a likely source of heating during the compaction process, the friction sensitivities of the powders were evaluated using a BAM friction apparatus. The HEBM Ni-Al powder did not react under the highest load possible (360 N); however, the NL Ni-Al had a 50% probability of reacting at 60 ± 5 N. Flash heating at point contacts during loading would cause rapid local temperature rises which can be approximated by

$$\Delta T = 2q\left(\frac{t}{\pi\rho Ck}\right)^{\frac{1}{2}}, \tag{3.3}$$

where q is the heat flux, t is the time duration, ρ is the density, C is the specific heat, and k is thermal conductivity [76]. For frictional heating the flux is given by $q = \mu\sigma v$ where μ is the friction

coefficient, σ is the applied stress, and v is the slip velocity. The frictional stress is limited by the shear strength of the material which is estimated to be $\tau = 0.577Y$, based on von Mises yield criterion. Given $\mu = 1$, $v = u_p$, $t = D/u_p$ (particle diameter, D) and volume averaged properties for the material constants, results in contact surface temperature rises in excess of 1000 K for both materials; however, it is unlikely that frictional loading would result in a temperature rise exceeding the melting point of Al. Once Al melts, the material would no longer be able to sustain a significant frictional load. Taking an Arrhenius form for the diffusion of Ni-Al with prefactor $D_0 = 2.18\times10^{-6}$ m^2/s and activation energy $E_A = 137$ kJ/mol [77], the diffusivity at 660°C is on the order of 10^{-13} m^2/s. The relevant distance for diffusion in 17 μs is given by $x\sim((10^{-13}\ m^2/s)(17*10^{-6}))^{1/2} \sim 1$ nm which would result in an insignificant amount of energy release due to reaction.

The bulk heating averaged over an individual particle due to friction can be approximated by

$$\Delta T = \frac{\mu\sigma v}{\rho C} A_H N_c t, \tag{3.4}$$

given,

$$A_h = \left(\frac{3FR}{8E'}\right)^{\frac{1}{3}}, \tag{3.5}$$

where A_h and N_c are the Hertz contact area and packing coordination number. Conservatively assuming a coordination number of 12 and 1 μs for rearrangement to occur during compaction, a temperature rise of 50 K and 100 K can be found for the HEBM Ni-Al and NL Ni-Al respectively. This indicates that while friction is a significant source of bulk heating, alone it is not enough to explain the difference in the behavior of the NL and HEBM Ni-Al.

For large propagation velocities, the maximum temperature rise at the crack tip is given by,

$$\Delta T = \sqrt{2}\frac{\left((1-\upsilon^2)KY\sqrt{u}\right)}{E\sqrt{\rho C k}}, \tag{3.6}$$

where K is the fracture toughness and u is the crack velocity [78,79]. Assuming a $K \sim 10$ $MPa/m^{1/2}$ and $u \sim 500$ m/s, the temperature rise would be on the order of 130 K for the NL Ni-Al, which is significantly lower than the flash rise associated with heating due to friction. The conclusion is that neither frictional heating nor fracture are enough to solely explain the rapid initiation and reaction observed in the NL Ni-Al; however, the NL powders do have a propensity to fracture as indicated by the fracture surfaces observed in Figure 1. Once the particles fracture, a significant

amount of surface area will experience frictional loading. Additionally, the smaller particles would result in a larger temperature rise within individual particles.

It is evident that the difference in the sensitivities of the HEBM and NL Ni-Al composite powders to mechanical stimulus is a result of the increased hardness and brittle behavior of the sputtered NL Ni-Al. The increased impact and friction sensitivity of the NL powder is readily explained by the increased hardness of the NL Ni-Al. Interparticle friction contributes to the sensitivity of the NL material, but neither friction nor fracture contribute enough to be solely responsible for the prompt reactions observed in the NL powders. This suggests that understanding and accurately modelling fracture may be key to understanding impact initiation of not only Ni-Al materials, but other brittle energetic systems as well.

3.6 Conclusions

The response of both HEBM and NL Ni-Al composite powders to impact loading are presented. The results indicate that fracture and interparticle friction are the dominant mechanisms governing the μs timescale reaction in NL Ni-Al powders. Two chemically equivalent powders with similar ignition temperatures were produced through HEBM and ball milling of magnetron sputtered NL Ni-Al. Having been produced through DC magnetron sputtering, the NL Ni-Al would be brittle as a result of porosity near the Ni grain boundaries [80], while the HEBM Ni-Al would remain ductile. The NL Ni-Al powders reacted on the μs timescale before transitioning to a slower reaction mode when impacted in the Asay shear experiment. The prompt reaction mode was observed at 130 m s^{-1} and 40 MPa, which is significantly lower than what has been previously reported in literature. In contrast, the HEBM Ni-Al powder reacted on the ms timescale.

The estimated impact pressure was significantly lower than the hardness of either powder, indicating that limited plastic deformation occurs during the initial passage of the compaction wave. Additionally, SEM imaging of the NL Ni-Al showed evidence of brittle failure that was not present in the HEBM Ni-Al. Together these results suggest that the three order magnitude difference in the ignition delay between the HEBM and NL Ni-Al may result from the NL Ni-Al powders fracturing during rearrangement, introducing a rapid local heating mechanism as well as greatly increasing the surface area experiencing friction which is not present in the HEBM Ni-Al. This

results in a reaction front that travels at the same velocity as the compaction front in the NL Ni-Al powder.

The observed influence of fracture in the impact initiation of NL Ni-Al composite particles suggests that formulation and production processes that result in a more brittle material may actively increase the sensitivity of the material to impact. Under weak loadings, where the impact pressure is lower than the bulk strength of the powder, reaction can still occur on the μs timescale. This implies that accurate modeling of the ignition of energetic materials at low impact velocities should include physics that detail and account for intraparticle fracture and associated heat generation mechanisms.

CHAPTER 4. DYNAMIC COMPACTION OF BALL MILLED AL GREEN BODIES

4.1 Introduction

Historically, interest in the dynamic compaction of porous solids has been used to investigate the behavior of the Mie-Gruneisen parameter (γ) at high pressures for solids as well as producing fully dense samples of high strength materials [16,81,82]. By shocking to the same pressure from different initial densities, evaluation of the relationship between the change in internal energy and the volume change allows measurement of γ. More recently, interest in porous materials and granular compaction stems from their application in blast attenuation [83,84] and understanding the behavior of granular explosives [85].

In a steadily propagating shock, the width of the shock wave is experimentally determined by the product of the shock velocity, Us, and the time it takes for the pressure to rise from 10% to 90% of the peak pressure, Δt. Grady observed that measurements on monolithic solids results in a fourth-power relationship between the strain rate (calculated as $u_p/ U_s\Delta t$) and the pressure rise in a shock, or $\varepsilon_t \propto \sigma^4$ [86,87]. Work since has shown that porous materials deviate from this behavior, and that the relationship between strain rate and driving pressure rise is nearly linear, or $\varepsilon_t \propto \sigma$. While discussing this behavior in powders, Grady suggested a dimensionally based dependence of the shock viscosity, η, related to the ratio of the density of the distended powder, ρ_0, and crystal density ρ_t, the crush strength of the powder, σ_c, and the particle size, a. From this Grady constructed the proportionality

$$\eta \sim \left(\frac{\rho_0}{\rho_t}\right)^m \sqrt{\rho_s a^2 \sigma_c}, \tag{4.1}$$

where m is a unitless exponent. Since the crush strength of a powder is necessarily a function of the strength of the parent material [8,82,88], the shock viscosity and shock width must also be a function of the strength of the parent material. As a result, equation (4.1) would indicate an increase in apparent viscosity with increasing crush strength.

This work seeks to investigate the effect of grain size refinement (ball milling) on the structure of propagating shock waves through porous Al and the characteristic time of pore collapse. It is generally known that the strength and viscosity of a material has little effect on the

state achieved following a supported shock or compaction wave in the hydrodynamic limit, where the pressure is approximately an order of magnitude higher than the yield strength. However, a heuristic argument would suggest that an increase in crush strength would be expected to result in a broadening of the compaction front when the pressure is low enough that the compaction time is not dominated by inertial effects.

The results presented in this work indicate that the argument in the previous paragraph is incorrect. While the Mie-Gruneisen equation of state is found to accurately predict the response of all porous materials tested, the strain hardening resulting from the ball milling process is found to result in a reduced Δt and reduced η compared to the unmilled Al. The rise time is found to decrease with increasing pressure for all conditions. It is proposed that the rise time is the result of the stress percolating ahead of the compaction front and interacting. Observations of the rise time as a function of sample thickness found the wave to be broadening at a rate close to the rate an elastic precursor would lead the wave front velocity, supporting the above interpretation of front width.

4.2 Experimental Methods

Three different initial powders were used in this work. Al powder with an initial size range of 44-420 μm (99.8% purity, metals basis) was purchased and sieved to a range of 106-355 μm over a 24 hour period. This powder is referred to as the unmilled (UM) powder. Al powder with an initial size range of less than 44 μm (99.5% purity, metals basis) with a listed average particle size between 7-15 μm was used as a precursor for the two milled Al powders used in this work. This powder was milled in a PM100 planetary ball mill (Retsch) at a ball to powder mass ratio of 10:1. The 9.5 mm 440C stainless steel milling media was used with a total mass of between 172-173 g. A process control agent (PCA), 20 ml Hexane, was added during the milling process to reduce cold welding. The powder was milled in an argon environment at 650 RPM for either 3 min (3WG) or 10 min (10WG). The powder was then dried for 24 hours before being sieved to the same 106-355 μm range over a 24 hour period.

The milled powders were then cold-pressed to a set height at densities from 80%-90% relative density (ρ/ρ_t). The pressed diameter was 12.7 mm with heights varying from 0.8-1.4 mm. All pellets used to measure Hugoniot points were taken at a minimum of a 12:1 diameter to

thickness ratio in order to achieve uniaxial strain. Micro computed tomography (CT) was performed on pressed pellets using a Skyscan 1272 X-ray Micro-CT (Bruker) with a reconstructed voxel having a side length of 12.7 µm. This allowed reasonable reconstruction of pore structures with effective diameters larger than 30 µm. Reconstruction from the tomographic imaging was performed using the CTan software. Thresholding was performed so that the average density of the reconstructed pellet matched the macroscopically observed density.

Plate impact experiments were performed in the transmission geometry. A copper flyer was launched using a single stage light gas gun at velocities between 250 and 800 m-s. This struck a copper base plate which then transmitted a shock into the Al pellets. The pellets were backed with a 9 µm Al mirror attached to an acrylic (PMMA) window. The flyer plate tilt and impact velocity was measured using an array of 12 shorting pins as well as a single photonic Doppler velocimetry (PDV) probe. The target arrangement is shown schematically in Figure (4.1). Three pellets were arranged in an equilateral triangle centered on the target and tested simultaneously. The tilt and arrival time of the incoming shock transmitted from the Cu base plate into the Al powder compacts was measured by 3 PDV probes arranged in an identical triangle rotated 60° to the sample orientation. The Al-PMMA interface velocity was monitored on the centerline of each sample by a single PDV probe. The known shock response of Cu and PMMA allowed the shocked state of the Al compacts to be calculated using impedance matching. The PDV signals were analyzed using Matlab and SIRHEN (Sandia InfraRed HEtrodyne aNalysis).

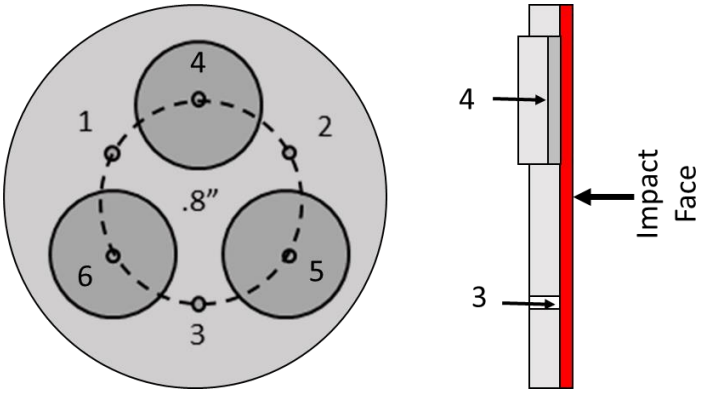

Figure 4.1. Up barrel and section view of target plate. Three Al compacts are mounted on a copper driving plate and held in place by PMMA. The windows are press fit to secure the pellet and sealed on the back surface with epoxy.

4.3 Results and Discussion

4.3.1 Compact Morphology

Analysis of the pore geometry is presented in Figure (4.2). The values plotted are the diameter of the pore for an equivalent sphere with the same volume (DV) and surface area (DA). Additionally, the sphericity is defined as the ratio of the surface area of a sphere with the same volume as the given pore to the measured surface area of the particle. As a result, the sphericity is a measure of the compactness of the pore, with larger values approaching a sphere in geometry and smaller values becoming more elongated and distorted. The results presented in Figure (4.2) show that the pore geometry does not vary significantly between the UM, 3WG, and 10WG Al compacts at a fixed density and height. At all densities, it was found that a logarithmically increasing bin size results in a constant rate of occurrence up to a certain size. At that point, the rate of occurrence rolls over, then decays as a power law. For the major diameter, this roll over occurs between 200-300 μm for the UM and 10WG and 300-400 μm in the 3WG. The sphericity for pore diameters above 100 μm is preferentially distributed between 0.4 and 0.8, with pore diameters below 100 μm the sphericity is biased towards lower values. This indicates that smaller pores are more distended and larger pores more compact.

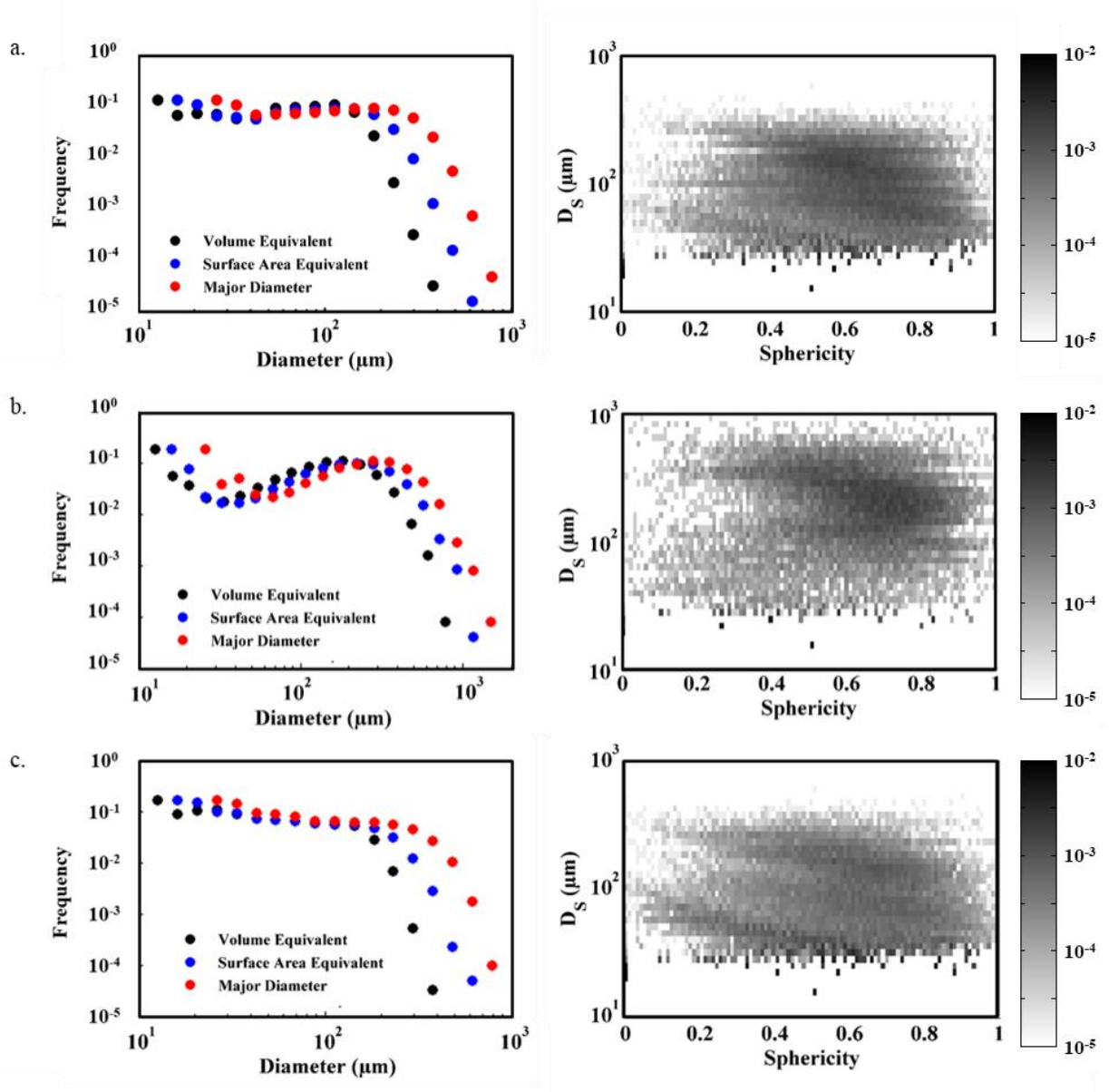

Figure 4.2. Pore diameter and sphericity as a function of pore dimater for a. UM, b. 3WG, and c. 10WG Al compacts pressed to 85% relative density. The results indicate a similar distribution of pore size and geometry for the UM and 10WG, with the 3WG having a larger fraction of pores larger than 200 µm in comparison. The shading indicates the frequency of occurance.

A reconstruction of the pore geometry is presented in Figure (4.3). The pores are colored based on their volume equivalent diameter. The results show a radial gradient with a preferential distribution of larger pores to one side of the pellet. This is indicative of an observed density gradient as a result of pressing, with the density varying from 85% to 95% moving across the

pellet diameter. The density in the region of interest for the PDV probe (a central cylinder with a diameter of approximately 3 mm) has increased uncertainty in density. For a pellet pressed to 90% this amounted to an uncertainty in density of 2%. This uncertainty is apparent in the observations made about the equation of state in the following sections and contributes to the uncertainty in the observed rise time, as a larger average pore size would be expected to result in an increased rise time.

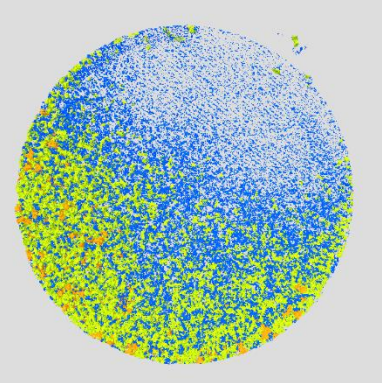

Figure 4.3. Image of the reconstructed pore space for a sample of 3WG Al pressed to 90% density. The pores are color coded by D_V, with blue pores being < 100 µm, yellow 100-200 µm, orange 200-400 µm and red >400 µm.

4.3.2 Plate Impact Experiments

4.3.2.1 Impedance Matching

An x-t diagram is presented in Figure (4.2) illustrating the position of the leading edge of the shock throughout the experiment. The flyer plate initial impacts the sample at impact velocity (v_f). This transmits a shock into the copper base plate travelling at U_s^{Cu}. The wave is then transmitted into the Al compact, driving the compact from the resting state, S0, to the shocked state, S_1. Once the wave interacts with the Al-PMMA interface, a release wave is reflected into the Al (since the impedance Al is larger than that of PMMA) sending the aluminum from S_1 to S_2.

The impact experiments directly measured the impact velocity (v_f), tilt, velocity of the Al-PMMA interface (u_p^{int}), and arrival time at the front and back face of every sample. This allows three methods of impedance matching using a combination of the impact velocity, interface particle velocity, and the average shock velocity (U_s) determined by the differences in the time of

arrival and the sample thickness. These methods are presented schematically in Figure (4.3). Method 1 utilizes the Rayleigh line of the impacted material and the reflected Hugoniot of the flyer plate to solve for S_1. The Rayleigh line in P-u_p space is given by the pressure jump, equation (2.7). Since the P_0 is negligible compared to the peak pressure, the Rayleigh line is the straight line intercepting the origin with a slope of $\rho_0 U_s$. The condition reflected into the driving plate is given by a left facing Cu Hugoniot centered at the flyer velocity. The intersection of these two curves sets the pressure and particle velocity at S_1.

Since the shock is fully supported throughout the duration of the test, the flyer plate velocity and particle velocity at the Al-PMMA interface can be used to solve for S_1 assuming the release path can be approximated by the left facing Hugoniot of Al. This assumption has been shown to be reasonable in previous work on sintered Al at similar densities [84] and the error introduced is expected to be small relative to the error observed. The pressure at S_2 can be found using the principal Hugoniot of PMMA centered at the origin. Conservation of momentum requires that the pressure at the Al-PMMA interface be equal in both materials. As a result, the left facing Hugoniot of Al passing through S_2 (u_p^{int}, P^{int}) approximates a release path. The intersection of this release path with both the flyer plate Hugoniot and Rayleigh line described in Method 1 provide separate measures of S_1 and constitute Method 2 and Method 3 respectively. A summary of the plate impact experiments is presented in Table 6.1 with u_p, U_s, and P being averages of the resulting impedance matching and Δt being the measured 10%-90% rise time. Reference Hugoniot data for Cu, PMMA, and Al 1100 was taken from either Cooper [22] or Marsh [89].

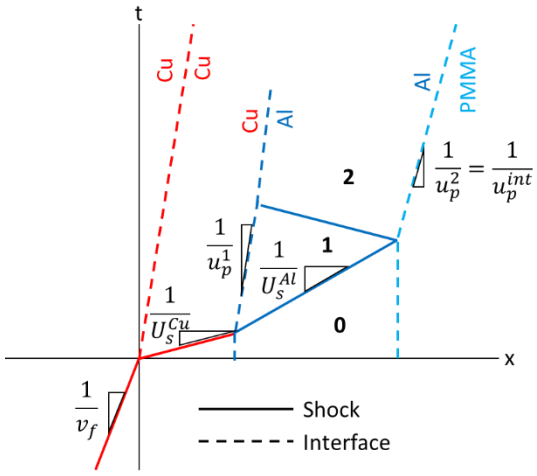

Figure 4.4. x-t diagram of the Al plate impact experiments. Dashed lines indicate interfaces with the sample being driven from the resting state (S_0), to the shocked state (S_1), and finally the state after the wave transmits into the PMMA (S_2).

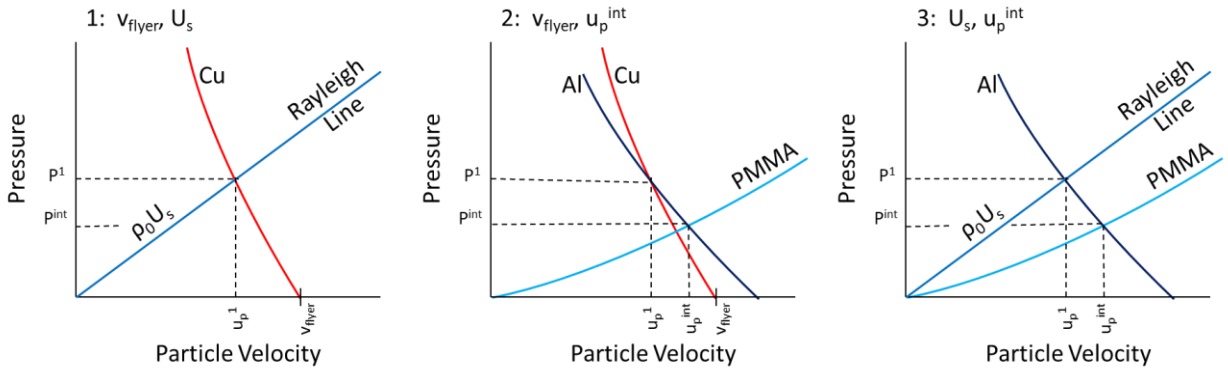

Figure 4.5. Impedance matching used to determine average shock parameters.

Table 4.1. Summary of impact experiments with calculated shock parameters.

	v_f (km/s)	Sample	Material	t (mm)	ρ_0/ρ_t	Δt (ns)	u_p (km/s)	Us (km/s)	P (GPa)
1	0.254	19	UM	1.00	0.91	36	0.22 ± 0.01	1.96 ± 0.08	1.08 ± 0.04
		20	10WG	1.00	0.89	18	0.20 ± 0.01	4.07 ± 0.42	1.97 ± 0.15
		21	3WG	1.00	0.89	20	0.22 ± 0.02	1.83 ± 0.74	0.96 ± 0.35
2	0.485	1	UM	1.00	0.89	14	0.40 ± 0.01	3.31 ± 0.17	3.19 ± 0.12
		2	10WG	1.00	0.90	10	0.41 ± 0.03	2.90 ± 0.67	2.89 ± 0.51
		3	3WG	1.00	0.90	10	0.38 ± 0.01	4.09 ± 0.37	3.75 ± 0.25
3	0.710	4	UM	1.00	0.91	25	0.60 ± 0.04	3.27 ± 0.76	4.74 ± 0.82
		5	10WG	1.00	0.89	12	0.58 ± 0.02	3.77 ± 0.46	5.76 ± 0.47
		6	3WG	1.00	0.90	26	0.56 ± 0.01	3.97 ± 0.09	5.41 ± 0.09
4	0.817	7	UM	1.00	0.90	15	0.66 ± 0.02	3.73 ± 0.40	6.02 ± 0.47
		8	10WG	1.00	0.89	8	0.65 ± 0.02	4.14 ± 0.43	6.49 ± 0.49
		9	3WG	1.00	0.90	11	0.62 ± 0.01	5.02 ± 0.16	7.57 ± 0.17
5	0.707	10	UM	1.00	0.80	7	0.63 ± 0.01	1.95 ± 0.03	2.67 ± 0.04
		11	10WG	1.00	0.81	32	0.63 ± 0.02	2.31 ± 0.33	3.16 ± 0.37
		12	3WG	1.00	0.81	32	0.63 ± 0.04	2.53 ± 0.83	3.43 ± 0.90
6	0.705	13	UM	1.00	0.85	35	0.60 ± 0.01	2.75 ± 0.03	3.79 ± 0.03
		14	10WG	1.00	0.86	18	0.61 ± 0.03	2.94 ± 0.61	4.11 ± 0.66
		15	3WG	1.00	0.86	11	0.59 ± 0.01	3.05 ± 0.27	4.13 ± 0.29
7	0.710	16	10WG	1.40	0.90	18	0.57 ± 0.01	3.76 ± 0.31	5.58 ± 0.32
		17	10WG	1.21	0.90	21	0.51 ± 0.05	4.44 ± 0.31	5.55 ± 0.97
		18	10WG	0.80	0.90	7	0.59 ± 0.04	3.61 ± 0.75	5.96 ± 0.77

4.3.2.2 Hugoniot Measurements and Equation of State

Shots 1-4 were performed in order to measure the P-u_p Hugoniot for all material samples as well as study the effect of increasing pressure on the structure of the wave front. The resulting P-u_p Hugoniots are presented in Figure (4.4). The data shows no significant trend between the milling condition and the shocked state. This is expected since the crush strength for the UM and 10WG powder pressed to 90% relative density was found to be no more than 160 MPa and 260 MPa respectively at strain rates from 1000-2500 s^{-1} [90]. The pressures observed in the plate impact experiments are approximately an order of magnitude greater than this, which would indicate a state of hydrodynamic flow with strength effects being negligible.

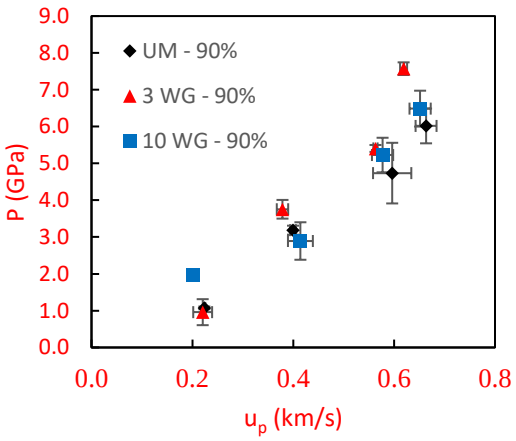

Figure 4.6. P-u_p Hugoniots at different milling conditions. Error bars represent the scatter resulting from the methods of impedance matching.

A number of previous works have shown that the P-v Hugoniot a porous material composed of a ductile parent material with a linear U_s-u_p relationship can be predicted using a Mie-Gruneisen equation of state and the shock conservation relations [1,5]. In this case, the P-v Hugoniot of the porous material is given by

$$P = \frac{[2v-\gamma_0(v_0-v)]\, c_0^2(v_0-v)}{[2v-\gamma_0(v_{00}-v)][v_0-s(v_0-v)]^2}, \tag{4.2}$$

where γ_0 is the reference state Gruneisen parameter, v_0 and v_{00} are the reference specific volume of the parent material and the specific density of the distended powder, and c_0 and s are the intercept and slope of the linear U_s-u_p relationship for the parent material. Parameters for Al

1100 were used to solve for P-v states and then the jump equations were then used to convert to P-u_p Hugoniots at various densities. The resulting curves are compared to the experimental results from this work as well as results from the literature in Figure (4.5) and Figure (4.6). It can be observed that the relationship in equation (4.2) accurately predicts the pressure response of a diverse set of materials (sintered and cold-pressed) over a broad density range (60-90% relative density). A closer view of the Hugoniot measurements from this work, shown in Figure (4.6), indicates that all data points, excluding the lowest point corresponding to 10WG, fall within the 85% and 95% relative density Hugoniots.

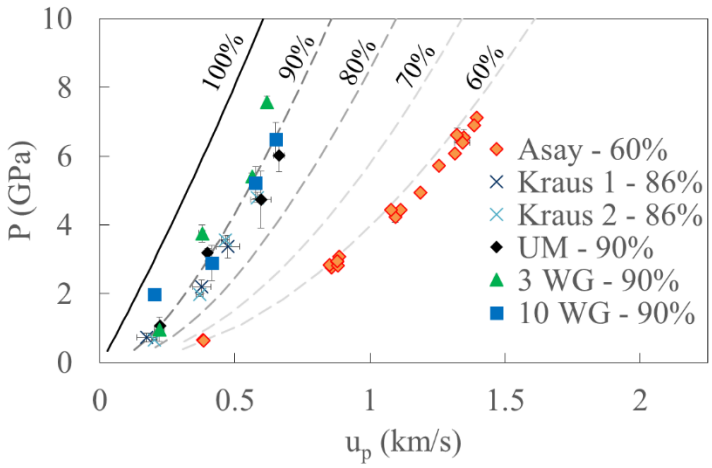

Figure 4.7. P-u_p Hugoniots for various porous Al experiments at relative densities from 60% to 90%. Data on sintered Al at 86% relative density was taken from Kraus et al [84] and hot pressed Al 1100 at 60% relative density was taken from Asay [91]. Curves at various starting densities were determined using equation (4.2).

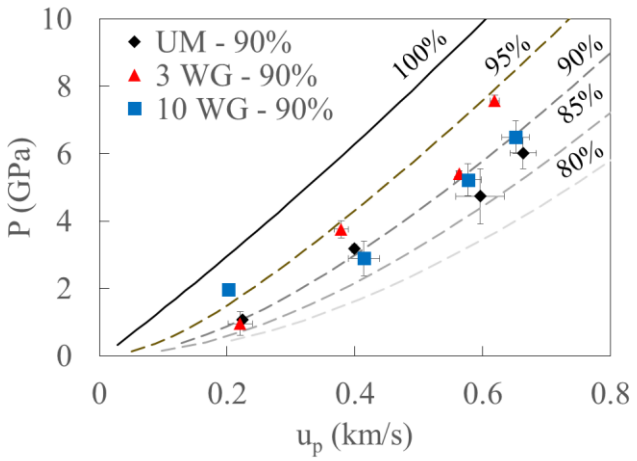

Figure 4.8. View of the Hugoniot measurements taken at an initial relative density of 90% performed in this work. The results are reasonable represented by a Mie-Gruneisen equation of state with deviations likely stemming from the initial sample preparation.

4.3.2.3 Wave Structure and Shock Rise time

Time resolved measurement of the Al-PMMA interface velocity through PDV allows inference of the shape of the shock wave. Particularly, the 10%-90% rise time in interface particle velocity corresponds to a temporal measurement of the shock width. Figure (4.7) presents the measured interface velocity for samples 2, 5, 8, and 20. In all experiments performed, the particle velocity rose to a maximum value in under 50 ns. This state was held for approximately 200 ns. All state measurements were made during this steady state.

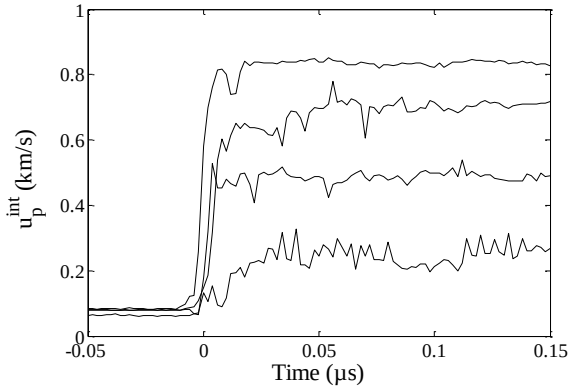

Figure 4.9. Pressure traces for samples 2, 5, 8, and 20. Notice the decreasing rise time with increased peak pressure.

A plot of rise time as function of peak pressure is presented in Figure (4.8). In general, it can be observed that the rise time decreases with increasing pressure and that the UM material has a longer rise times at all pressures compared to the 10WG material. The STFT performed to analyze the PDV frequency spectrum resulted in a temporal uncertainty of 2 ns. Assuming a steady shock velocity, the shock width is given by the product of the rise time and shock velocity and is found to be between 30-150 μm. Quantitatively there appears to be no significant difference between the 3WG and 10WG milled materials excluding the point at 5.4 GPa for the 3WG material.

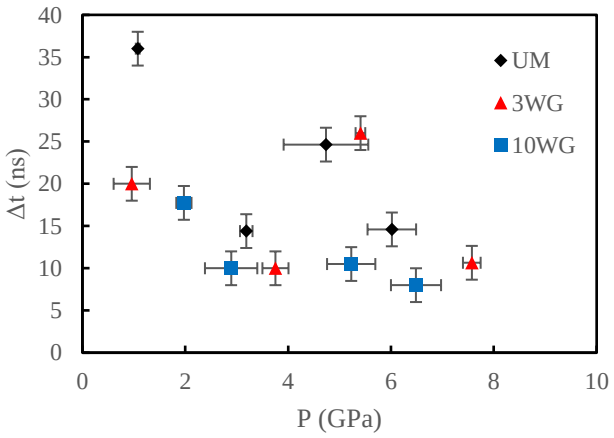

Figure 4.10. Shock width as a function of input pressure for 90% relative density compacts.

The strain going from S_0 to S_1 is equal to the ratio of the steady particle velocity (u_p) and the wave speed (U_s). Assuming a reasonably steady wave speed over the thickness of the pellet and a linearized pressure rise, the strain rate experienced in the shock rise is given by

$$\varepsilon_t = \frac{u_p}{U_s \Delta t}. \tag{4.3}$$

Figure 6.9 plots the strain rate as a function of the peak pressure. Uncertainty in the shock velocity and rise time results in large error bars on the strain rate; however, an overall trends can still be observed. The UM and 10WG materials have a reasonably linear response between peak pressure and strain rate. Scatter in the 3WG response prevented a meaningful fit for viscosity. The apparent shock viscosity is given by the slope of the lines of best fit represent with values from 300-600 Pa·s.

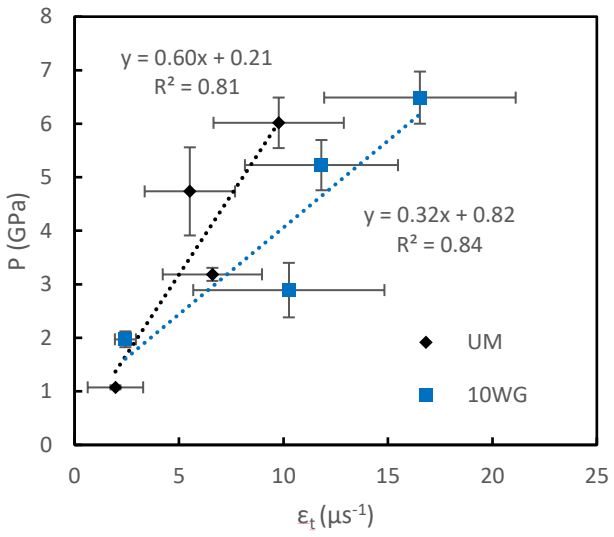

Figure 4.11. Plot of pressure rise as a function of strain rate. Uncertainty in the strain rate is large; however, the results indicate a reasonable linear dependence between pressure rise and strain rate for the UM and 10WG compacts.

The trends indicate approximately a two-fold reduction in effective viscosity with an increase in crush strength. This result runs contrary to equation (4.1), which would indicate an increase in viscosity with increasing crush strength. However, this result may stem from the increased strength of the ball milled material. Since the wave speed for all but one impact condition was below the sound speed of bulk aluminum (c_0 = 5.38 km/s), the wave front travels slower than an elastic wave travelling the shortest distance between two points. In a porous material, the shortest distance between points is frustrated by the pore structure and stress waves are require to percolate through points of contact before crush-up. The interaction of stress percolating through different paths results in the compaction wave and defines its width. In a matrix composed of a stiffer material, a larger number of wave interactions and peak stress is necessary for the front of the wave to be resolved and crush-up to begin. As a result, a material with a lower crush-strength would appear to have a broader wave and the resulting linearized strain rate would be lower at the same pressure compared to a stiffer material.

4.3.2.4 Shock Width as a Function of Propagation Distance

To further validate the above interpretation of the shock width in the 90% relative density compacts of Al, an experiment was performed with 3 samples with different thicknesses (shot 7,

samples 16-18). A comparison of the peak pressure as a function of sample thickness (x) is given in Figure (4.10). It is apparent that the peak pressure is within the experimental error for all samples. The plateaued state achieved for all 4 samples is constant to within reason, with all samples having a wave speed of approximately 4.6 km/s except sample 17 which was 4.9 km/s. A plot of the observed rise times is presented in Figure (4.11). In the event that the interpretation presented in the preceding subsection is accurate and that the wave is dispersive, the leading edge would be travelling at approximately c_0 and the peak would be assumed to travel at U_s. In this case, an upper limit for the wave thickness, *w*, as a function of position would be given by

$$w = (c_0 - U_s)\frac{x}{U_s}, \tag{4.4}$$

where *x* is the distance from the point at which the waves overlapped. The derivative of equation (4.3) with respect to *x* gives the rate at which the wave broadens. For c_0 = 5.38 km/s and U_s = 4.6 km/s, $\frac{dw}{dx} = 0.17$. The observed increase in thickness with position is ($21.23 \cdot 10^{-3}$ μs/mm)·(4.6 mm/μs) = 0.10. The observed value is reasonably close to the predicted value considering the simple nature of the analysis with no attempt being made to account for the increased percolation path length. If the measured value for $\frac{dw}{dx}$ is used to solve for an effective sound speed in the porous material, the result is found to be $1.1U_s$ = 5.06 km/s.

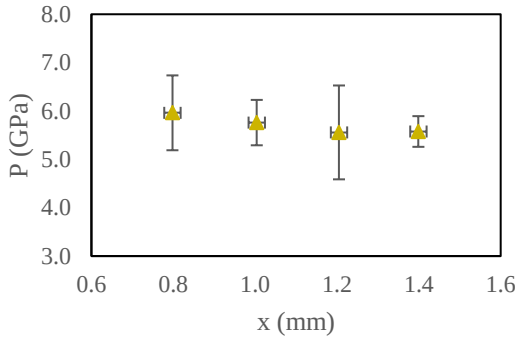

Figure 4.12. Peak pressure as a function of propagation distance for 90% relative density 10WG Al compacts. The result indicates that the pressure is constant within error for the propagation distances considered.

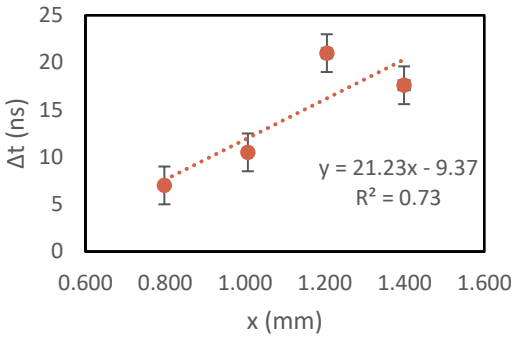

Figure 4.13. Rise time as a function of sample thickness. Note the nearly linear increase in rise time with propagation distance.

4.4 Conclusion

Grain size reduction through ball milling of Al was found to have no effect on the equation of state of Al. The shocked state of the porous material was reasonably predicted by a Mie-Gruneisen equation of state for all conditions evaluated in this work. This result is expected considering the stresses observed for all but the lowest impact velocity are an order of magnitude greater than the crush strength of the hardest compact (260 MPa, [90]).

The structure of the compaction front was found to vary with milling condition and peak stress. The rise time was found to decrease with increasing peak stress for all milling conditions. This result is in line with what has been generally observed in other dynamic compaction studies [82]. Furthermore, a linear relationship between peak stress and strain rate was observed in the UM and 10WG materials, as had been previously observed in the compaction of other powder systems [87]. Previously, this relationship had been observed in highly distended powders (granular compaction). This study showed that this behavior persists in porous materials with relative densities as high as 90%.

Interestingly, ball milling and the associated increase in crush strength was found to result in a reduction in apparent viscosity and rise time as a function of pressure. This is contrary to the expected behavior indicated by equation (4.1), where increasing the crush strength would be expected to result in an increase in the apparent viscosity. This result is attributed to the porous nature of the sample, with the shock width resulting from stress percolation. Since the wave

front travels at a velocity lower than the acoustic velocity of the parent material, stress waves percolate ahead of the compaction front. In this case, the width of the compaction front is determined by the point at which the leading stress begins to compact the material. This would explain the reduction in compaction width with increasing strength of the parent material, as a greater stress would need to be reached for compaction to begin. As a result, the width of the compaction front and apparent viscosity would reduce with increasing crush strength. The variation in rise time with propagated distance results in a rate of broadening at the same order of magnitude as what would be predicted by a leading edge propagating at c_0 for the parent material and a peak travelling at the observed wave speed. This further serves to validate the interpretation of the compaction front thickness.

CHAPTER 5. THE IGNITION KINETICS AND SELF-PROPAGATING REACTION OF 2AL+3NIO REACTIVE MULTILAYER THIN FILMS

5.1 Introduction

While the capacity for aluminum to reduce metal oxides has been known for over 150 years [92,93], the fundamental reactions occurring in the ignition and propagation of thermite reactives are not well understood. Commercially, thermite reactions have been critical in the recovery of many metals from their oxides through combustion synthesis, as well as a means for large scale welding of railroad ties [94]. Despite the high energy density of these materials the reaction and energy release rate is limited, to the point that many micron-scale powder mixtures require significant preheating to initiate and often are not self-sustaining [95]. The development of reactive multilayer thin films (RMTF) [63] and nanoscale powders [96,97] have reduced the diffusion length-scale to 10s of nm resulting in a significant increase in the rate of energy release. This has resulted in thermites being used as localized heat sources for bonding electronic components [98–100], to eliminate biological agents [101], as well as microthrusters in microelectromechanical systems [102,103] making it more important than ever to understand the reaction pathways of thermites.

RMTF provide an ideal geometry for studying reaction mechanisms of condensed phase reactives. In the most common form, RMTF are produced through magnetron sputtering by alternating between sputtering targets. Control of individual layer thicknesses is approximately 1-10 Å, allowing the diffusion distances to be tailored throughout the RMTF. In a binary system with a periodic geometry, the stoichiometry is set by the thickness ratio of the two components. Additionally, since RMTF are produced under high vacuum, the materials deposited are in direct and intimate contact without the complication of native oxide layers acting as diffusion barriers. This has been shown to increase the ignition sensitivity of reactive materials resulting in ignition occurring well below any known melt temperature or eutectic temperature (Ni-Al for example) [62,104,105].

The vast majority of studies utilizing RMTF have focused on binary formation reactions (alloying reactions) [63]. This is in part due to the difficulty in depositing stoichiometric oxides

in addition to the sensitivity of nanoscale thermites, resulting in films that react during deposition or handling [103]. Studies on thermite RMTF have primarily focused on the Al-CuO_x system due to its high exothermicity (4.08 kJ/g [106]) and rapid propagation velocity (over 70 m/s) [99,103,107–111]. Additionally, propagation velocities from 40-60 m-s have been reported for films on substrate [109,111]. Differential thermal analysis (DTA) with rapid quench has been used to show that oxygen migration from CuO_x is the limiting process in Al/CuO_x, forming a diffusion barrier composed of alumina with a copper rich region on the CuO_x side [107]. It is yet to be seen if these properties are representative of thermites as a whole outside of the Al-CuO_x system.

Al/NiO thermites have similar exothermicity to Al/CuO (3.44 kJ/g versus 4.08 kJ/g respectively [106], but have an increased adiabatic flame temperature being limited by the vaporization temperature of Ni (3187 K) as opposed to Cu (2843 K). Furthermore, it has been suggested that the reaction temperature may not exceed the vaporization point of Cu_2O (2070 K) due to gas generation resulting in the disintegration of the multilayer. The lowest vaporization point expected in the Al-NiO system corresponds to Al at 2790 K [112]. However, nickel and aluminum are known to form several intermetallic phases, which may provide intermediate reaction steps in the thermite reaction and result in significant diffusion barriers. Previous work to create dense Al/NiO composites through deposition of Al around oxidized Ni nanowire resulted in a composite with a DTA onset temperature of approximately 400°C and a 2200 kJ/g heat of reaction [113]. The low heat of reaction was attributed to oxygen contamination as well as a nonstoichiometric ratio of Al to NiO.

In this paper, we explore the deposition and reaction of Al-NiO RMTF. The first section details the characterization of the as deposited RMTF. It is shown that stoichiometric, crystalline NiO is deposited through magnetron direct current (DC) sputtering using a NiO target. Examination of the Al and NiO interface with transmission electron microscopy (TEM) and electron dispersive spectroscopy (EDS) shows a complex intermixed zone, with Ni rich regions on either sized of a zone composed of Al and O. The second section addresses phase transformations occurring in the thermite at low heating rates through differential scanning calorimetry (DSC) and hot-stage X-ray diffraction (HS-XRD). DSC shows that at bilayer thicknesses above 300 nm the reaction is reliant on the Al melt for the majority of reaction to occur, while at lower bilayer thicknesses significant reaction occurs in the solid state, similar to

what has been observed in RMTF and mechanically activated Ni-Al [31,62]. HS-XRD shows the formation of $NiAl_3$ at temperatures as low as 180°C, which corresponds to the onset temperature for the 125 nm bilayer thickness. The final section examines the combustion of the Al-NiO RMTF. The observed self-propagating exothermic reactions are characterized as a function of bilayer thickness, and preheat temperature. Additionally, the ignition characteristics of the RMTF are examined through hot plate ignition and laser ignition delay with activation energies for ignition being determined.

5.2 Experimental Methods

Al/NiO multilayers were deposited by DC magnetron sputtering at a 2:3 molar ratio onto 25.4 mm NaCl windows purchased from Edmund Scientific, Si wafers thermally oxidized to have a 400 nm layer of SiO_2 and 5 mm diameter fused silica discs purchased from ESCO. Table 5.1 presents a summary of the deposition parameters. The deposition chamber was evacuated to a pressure of 10^{-7} Torr before being backfilled to 10 mTorr with ultra-high purity Ar. Multilayers were grown by alternating between sputtering of Al and NiO targets at a rate of 35 nm/min. The NiO target was turned off during Al deposition in order to avoid cross contamination. Deposition of stoichiometric, crystalline NiO was verified through wavelength dispersive X-ray spectroscopy (WDS) as well as X-ray diffraction (XRD). A constant bilayer thickness (λ, the combined thickness of one Al layer and one NiO layer) was maintained throughout deposition to a total film thickness of 4 μm, with Al being the initial layer and ending with NiO. The overall temperature remained below 50°C throughout the deposition process. Freestanding films were recovered from the NaCl by soaking in water.

Table 5.1. Deposition parameters.

	Al	NiO
Working distance (mm)	10.16	10.16
Base pressure (Torr)	10^{-7}	10^{-7}
Sputtering pressure (Torr)	10^{-2}	10^{-2}
Deposition rate (nm/min)	13.5	10

As-deposited multilayers and one reacted film were evaluated using cross-section TEM. Cross section TEM samples were prepared in a FEI Co. DB-235 dual beam scanning electron microscope/focused ion beam system. TEM and EDS were performed with a FEI Co. Titan G2 80-200 transmission electron microscope, which was operated at 200 kV. Unreacted samples were loaded into the microscope to examine the structure and composition of the reactant interfaces. Full-thickness images of the as-deposited multilayers were taken through scanning transmission electron microscopy (STEM) using a FEI Helios 3B scanning electron microscope operated at 30 kV, and included EDS elemental mapping of the multilayer structure.

DSC was used to characterize the heat release characteristics and thermal response of the RMTF using a DSC-8500 differential scanning calorimeter (PerkinElmer). Samples deposited on 6 mm fused silica discs were placed, sample side down, in copper crucibles with copper lids crimped to the pan and heated from 50°C to approximately 750°C at 40°C/min. After the initial heating ramp, the sample was allowed to cool and then reheated in order to subtract the baseline response. A N_2 gas flow at 20 ml/min maintained an inert environment throughout the experiment. Additionally, hot stage x-ray diffraction (HS-XRD) was performed using a Scintag PAD X diffractometer equipped with a Peltier-cooled Ge solid state detector and a Buehler Pt/Rh hot stage. The temperature was ramped from 25°C to 500°C a heating rate of 40°C/min with scans being taken at 20°C increments from 40°C to 500°C. Each scan was taken over a range of 10-65° 2θ with a 32 minute duration and 0.04° 2θ step size. During heating, the sample was held at a 0.02 mTorr vacuum.

The thermal ignition temperature was measured through hot plate ignition experiments. In these experiments, a steel plate brought to a steady temperature using an IKA C-Mag HS 7 hot plate monitored with a K-type thermocouple. For temperatures above 450°C, a steel hot knife was used in place of the hot plate to reach temperatures up to 800°C. Small foils, approximately 9-25 mm^2 in area, were then rapidly dropped from approximately 1-2 cm onto the hot plate, making sure not to linger in the hot convective region above the plate. Ignition was evident, resulting in a bright flash and the foil disintegrating. Failure to ignite resulted in curling and discoloration of the multilayer foil. A series of measurements were taken allowing a 50% probability of ignition threshold to be determined with a 95% confidence interval as determined using Neyer statistics [66]. The experiments were repeated in an argon environment and found to be within the margin of experimental error.

Laser ignition of the RMTF was performed using a Northrop-Grumman eDrive™ laser controller driving a 20 W 1-bar diode laser array in continuous wave mode at an 810 nm wavelength and a flat top spatial distribution, as presented in Figure 5.1. A 70R:30T beam splitter divided the beam into two paths such that the free standing multilayer foils could be laser preheated with the 30 percent of the beam transmitted. A 40 cm PCX lens reduced the other beam to a 5 mm spot size and preheated the film. The preheat temperature was measured using a FLIR SC7650 observing the Al side of the foil. The foils were ignited with a 500 µm FWHM beam focused onto the NiO side of the foil by a Mitutoyo 5x objective. A hot plate allowed calibration of the emissivity of the deposited Al and transmittance of the cold mirror up to 500°C. The propagation was imaged using a Phantom® v12 high-speed camera. Experiments were completed in air and argon.

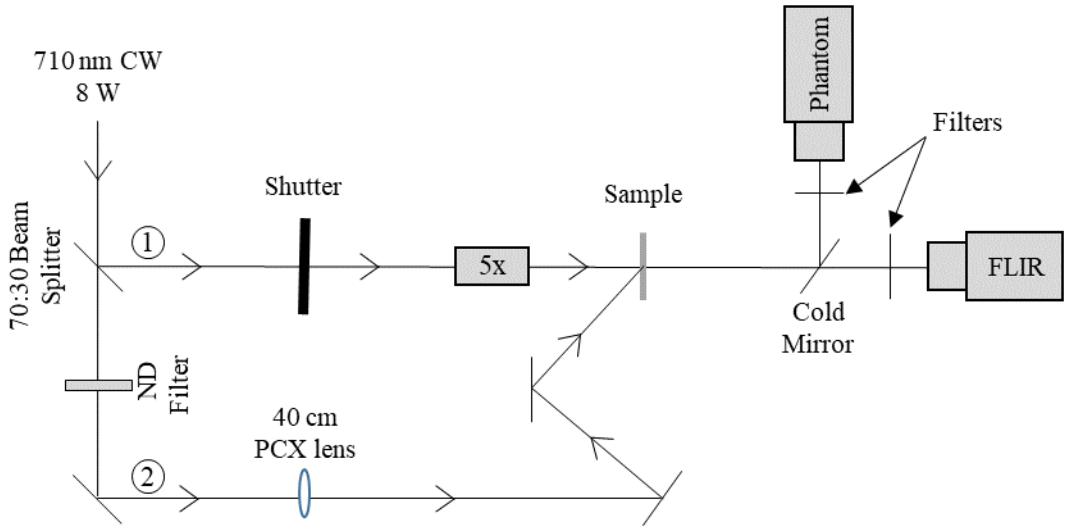

Figure 5.1. Laser line used to simultaneously preheat and ignite RMTF. 1) Beam separated for ignition. 2) Beam separated for preheat.

Freestanding RMTF with areas of approximately 5 mm by 5 mm were tested. The multilayers were mounted in the center of washers using polyimide tape, in a manner similar to Reeves et al [114]. The preheat beam was centered on the multilayer and provided even heating (±7°C) across the entire sample. The ignition beam was focused on one side of the film to allow sufficient propagation distance at a steady velocity. Heating was performed in two cycles, the first allowed measurement of the steady state temperature using the FLIR and lasted no more than 30 s. The Phantom and ignition beam shutter were all triggered simultaneously using a

Berkley Nucleonics Corporation Model 575 pulse/delay generator. Absorbing neutral density filters purchased from Newport Corporation were used to vary the preheat temperature from 50°C to 125°C without varying the ignition beam power.

5.3 Results

5.3.1 Microstructure and Composition

It is well known that the propagation and ignition of RMTF are dependent on the degree of premixing at the reactant interfaces as well as overall stoichiometry [63]. To evaluate the degree of premixing, the Al/NiO interface was investigated using STEM-EDS, which is presented along with images of the multilayer cross-section in Figure 5.2. Since the intermixed zone is an order of magnitude less than the finest bilayer thickness considered and all films were deposited at the same nominal temperature it is expected that this interface is independent of bilayer thickness. It is evident from the composition maps that cross contamination between the NiO and Al is insignificant, with oxygen confined to regions containing NiO, excluding the interfacial region. Close examination of the interface between the Al and NiO reveals a layered intermixed region approximately 8-9 nm in thickness. Line profile measurements of this region presented in Figure 3 show Ni rich regions on either side of a region composed primarily of Al and O. Additionally, the Ni(111) lattice spacing is observable through TEM. Trace Ni was also detected in the as deposited multilayers through XRD. When taken with the EDS line profile in Figure 5.3, this suggests that the interface transitions from NiO (region 1), to metallic Ni with some aluminum and oxygen (region 2), a layer of mostly aluminum oxide (region 3), a layer that contains a nickel aluminum solid solution with dissolved oxygen (region 4) and finally the aluminum layer (region 5). This interfacial structure is similar to that observed in Al/CuO bilayers produced through atomic layer deposition [115].

WDS and XRD were used to verify that stoichiometric, crystalline NiO was deposited. A separate 2 μm-thick NiO layer deposited on a Si wafer was examined through WDS and found to have a 1:1 molar ratio of Ni:O. Additionally, XRD confirmed that NiO layers, both monolithic and those in the multilayer, were single phase NiO with a NaCl structure (bunsenite). Al had a

face centered cubic structure. This confirms that the as deposited laminates consist of crystalline NiO and Al except for the intermixed region.

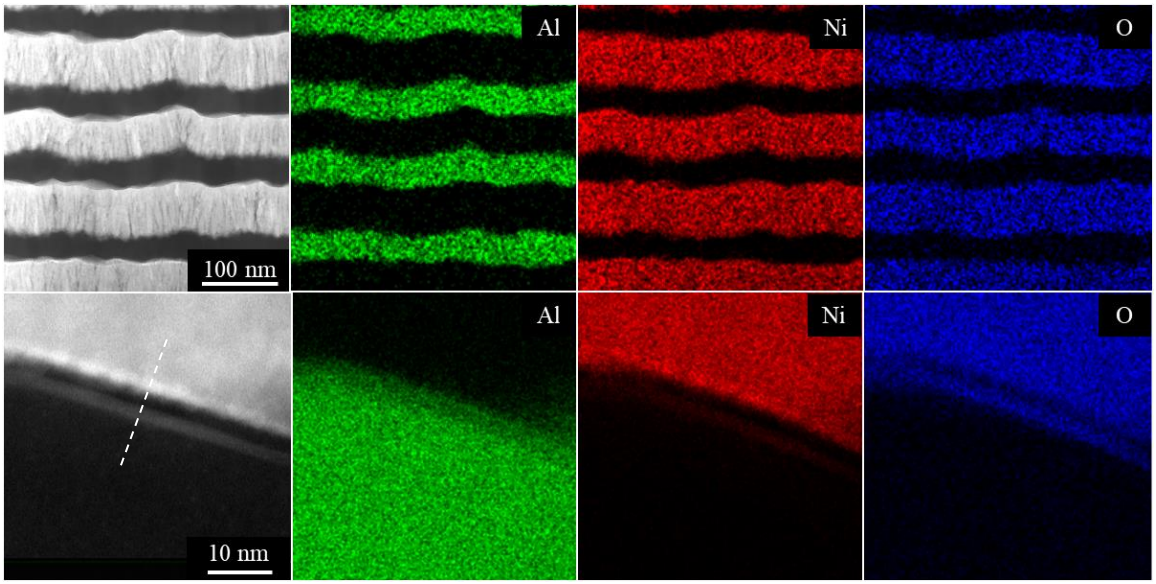

Figure 5.2. Top: Annular dark field image of STEM-EDS of a multilayer cross-section. Bottom: STEM-EDS of the Al-NiO interface taken through high-angle annular dark-field imaging with the dashed white line representing the location corresponding to the line trace in the following figure. Colored images are elemental maps of Al (green), Ni (red) and O (blue).

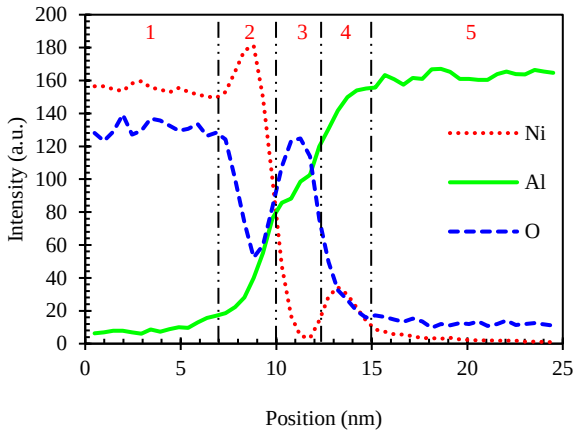

Figure 5.3. EDS line scan of interface between Al and NiO obtained in the transmission electron microscope. Regions transition from: 1. NiO, 2. Ni with O and Al, 3. Al_xO_y, 4. Al-Ni solid solution with O, to 5. Al with the boundaries approximately labelled by the vertical lines.

5.3.2 Thermal Analysis

In order to accurately interpret the ignition and propagation kinetics of these RMTF, the thermodynamics of the system must be understood. The behavior of the Al-NiO system at low heating rates was examined through a combination of calorimetry and HS-XRD. In order to evaluate the exothermicity of the deposited films and investigate the low heating rate reaction pathway, DSC was performed on multilayers with 125 nm, 666 nm, and 800 nm bilayer thicknesses and is presented in Figure 5.4. The thermograms of the multilayers with 666 nm and 800 nm bilayer thicknesses have a similar structure with an initial exothermic peak near 570°C. This is followed by the Al melt endotherm at approximately 660°C and a series of exothermic reactions, with the most notable exotherm being between 720-750°C. In comparison, the 125 nm film exhibits a broad exotherm starting at approximately 230°C that extends to nearly 400°C. This is followed by a small exotherm at 560°C and one at 680°C. Interestingly, there is not a significant Al melt endotherm in the finest bilayer thickness, which indicates that Al has largely reacted before 660°C. Integration of the response curves yield exothermicities between 0.7-1.0 kJ/g, which is significantly lower than the theoretical value of 3.14 kJ/g (3.44 kJ/g for 2Al+3NiO [106]). This result suggests that significant exotherms occur above 750°C, which is consistent with Zhang et al [113].

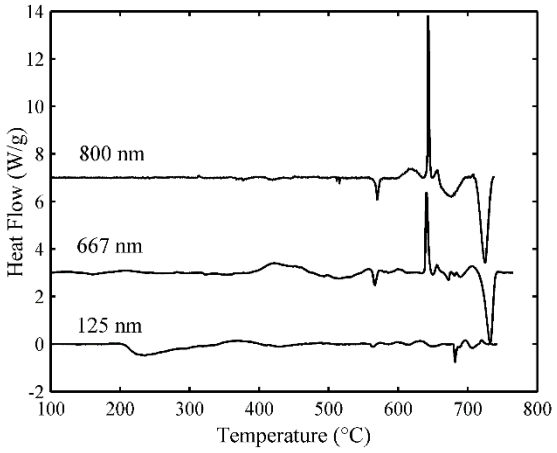

Figure 5.4. DSC thermograms of Al-NiO RMTF as a function of bilayer thickness. Plotted exotherm down.

As indicated by the DSC measurements, reaction proceeds at temperatures much lower than the melting point of Al when utilizing finer bilayer thicknesses. HS-XRD was performed at

similar heating rates to probe the reaction process that leads to these low temperature reactions, a representative case (125 nm bilayer thickness) is presented in Figure 5.5 with experiments being performed on designs with 125 nm, 167 nm, 333 nm, and 667 nm bilayer thicknesses and schematically represented in Figure 5.6. The 25°C scan further confirms that the RMTF is initially composed of crystalline Al and NiO.

In general, the first product phase ($NiAl_3$) is observed to form as low as 180°C. The 667 nm bilayer thickness Al/NiO shows limited reduction in Al or NiO peak intensity below 500°C; however, evidence of $NiAl_3$ appears at 300°C with Ni formation at 380°C. The increase in the onset temperature for $NiAl_3$ in this bilayer thickness is expected to result from the reduced number of interfaces in the 667 nm design and detectability limits of the HS-XRD given the consistency in observation temperatures in the 3 finer designs. The 125 nm bilayer thickness Al/NiO shows evidence of reaction at 200°C with the appearance of peaks corresponding to $NiAl_3$ and the onset of crystalline Ni formation at 240°C. As the sample is heated further, the Ni and $NiAl_3$ peak intensity increases as Al and NiO peaks weaken. At 440°C an additional transition occurs in the 125 nm bilayer thickness. The Al peaks are no longer measurable and the $NiAl_3$ has been consumed in the formation of Ni_2Al_3. At 500°C, NiO is still present, albeit with reduced intensity, as well as Ni_2Al_3 and Ni. A similar process occurs in the other designs; however, Al is not completely consumed and $NiAl_3$ persists up to 500°C as well as the first appearance of Ni being shifted to between 340°C and 380°C. The lack of cracking or crazing suggest that there was not outgassing, as a result it is expected that the oxygen liberated from the Ni forming $NiAl_3$ has reacted with Al. It is suspected that amorphous aluminum oxide forms during the initial reaction in all bilayer thicknesses and continues to grow throughout the experiment. This would be consistent with previous work on the Al-CuO_x system did not observe diffraction peaks through broad-beam XRD, but did observe an alumina growth layer forming at the Al-CuO_x interface through TEM [107].

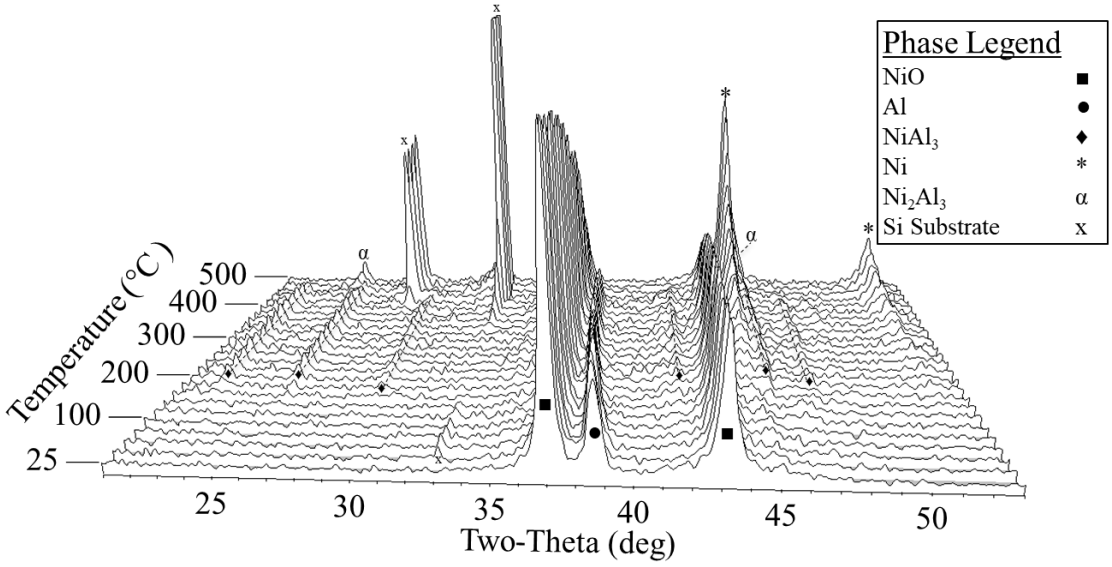

Figure 5.5. HS-XRD of 125 nm Al-NiO deposited on silicon substrate.

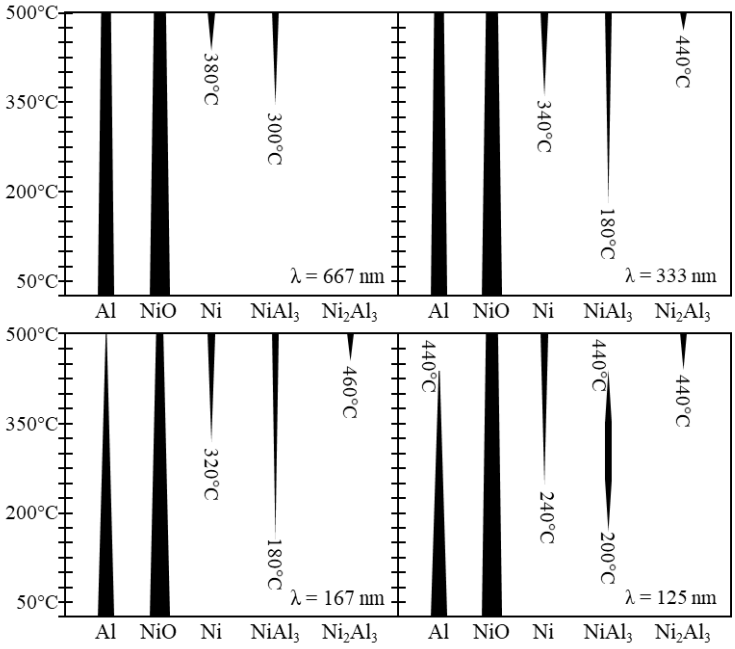

Figure 5.6. Schematic representation of phase formation in HS-XRD.

5.3.3 Characterization of Ignition Temperature and Self-Propagating Reaction

The ignition behavior of the Al/NiO multilayer foils was evaluated through hot-plate ignition experiments with the results presented in Figure 5.7. Ignition temperatures were found to vary from 260°C to greater than the melting point of Al. It is interesting to note that this is

commonly observed in Al based reactives, and has been observed also in Al-CuO nanothermites [103]. The sharp change in ignition temperature (~300°C) between 305 nm and 333 nm bilayer thicknesses indicates a change in reaction mechanism with melting being required for ignition at larger bilayer thicknesses. The error bars are representative of the 95% confidence interval for a 50% probability of ignition. The associated uncertainty in the temperature was accounted for in determining this value. Samples with bilayer thicknesses 500 nm and above did not ignite below 800°C.

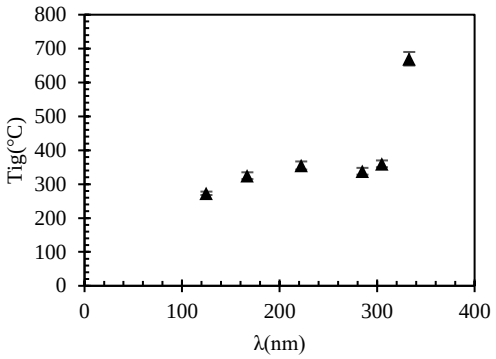

Figure 5.7. Ignition temperature of Al-NiO as a function of bilayer thickness. Bilayer thicknesses tested at or above 330 nm reacted have ignition temperatures greater than the melting point of Al. Error bars represent the 95% confidence interval for a 50% probability of ignition.

A representative laser-stimulated ignition and propagation event is presented in Figure 5.8 where the laser preheat line presented in Figure 1 was utilized. It is apparent from the images in Figure 5.8a and quantifiably evident in Figure 5.8b that the preheating is even and a steady, stable propagation is observed. Figure 8b plots the wave front position versus time within the ignition beam, freely propagating through the preheated foil, and into the mounting Kapton tape. The steadily propagating front releases a large amount of gas, which leads the reaction front. The bright front eventually propagates past the end of the un-taped edge of the foil, verifying that it is a gas phase and not a separate reaction front. Since testing of the samples occurred in a vertical orientation, it is important to note that the propagation front traveled at a constant velocity in all directions, indicating that any effect of buoyancy on preheating was negligible for the results in question. Molten droplets track with the reaction front with a large amount of gas emission trailing the steady propagation. The emitted gas is thought to be either vaporized Ni or a finely distributed aerosol of condensed phase products.

The measured effect of preheat on 125-667 nm bilayer thicknesses propagation velocity is shown in Figure 5.9. As expected, the propagation velocity is found to increase with preheat temperature for all bilayer thicknesses. All reactions propagated stably and steadily after propagating over one beam diameter from the point of first light. Thermal gradients through the film thickness are expected to be negligible, since the Biot number ($Bi = hL_c/k$, where h is the heat transfer coefficient for free convection, L_c is the film thickness, 4 μm, and k is the mass averaged thermal conductivity, 135 W/m^2K) is expected to be several orders of magnitude less than 1. Initial tests run in an argon environment propagated within 5% of the velocity observed in air for preheats below 125°C. The effect of preheat temperature were not investigated at higher temperatures to avoid effects of prereaction as indicated in the HS-XRD. The ignition delays trend as expected with increasing time to first light with increasing bilayer thickness. Preheat temperature has little effect on the ignition delay at bilayer thicknesses below 400 nm, with a significant increase in delay effects at higher bilayer thicknesses.

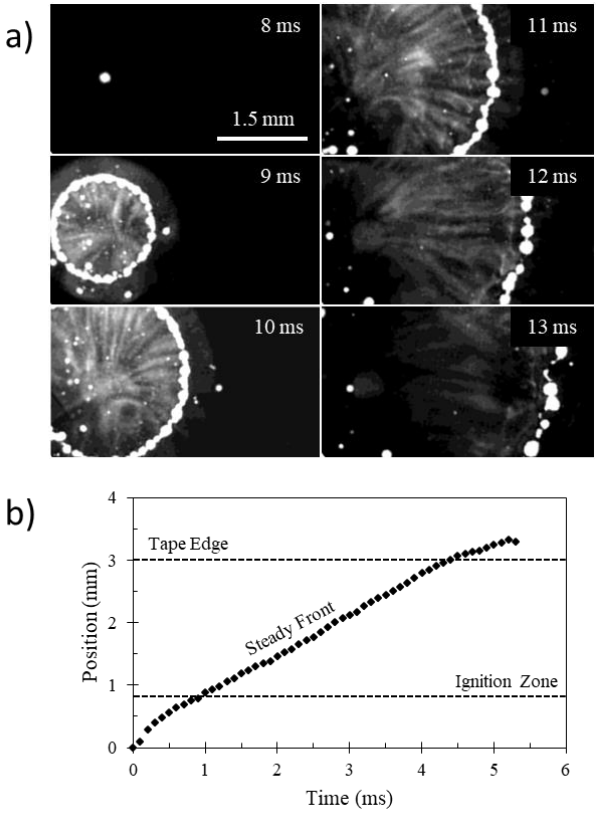

Figure 5.8. a) Reaction front propagation in λ = 571 nm Al-NiO at 80°C preheat temperature. Ignition occurred after an 8 ms delay and the propagation is indicated by the bright leading edge

and is followed by hot gas. b) Plot showing the reaction front transitioning from the zone affected by the ignition beam to a steady propagation front, then encountering substrate.

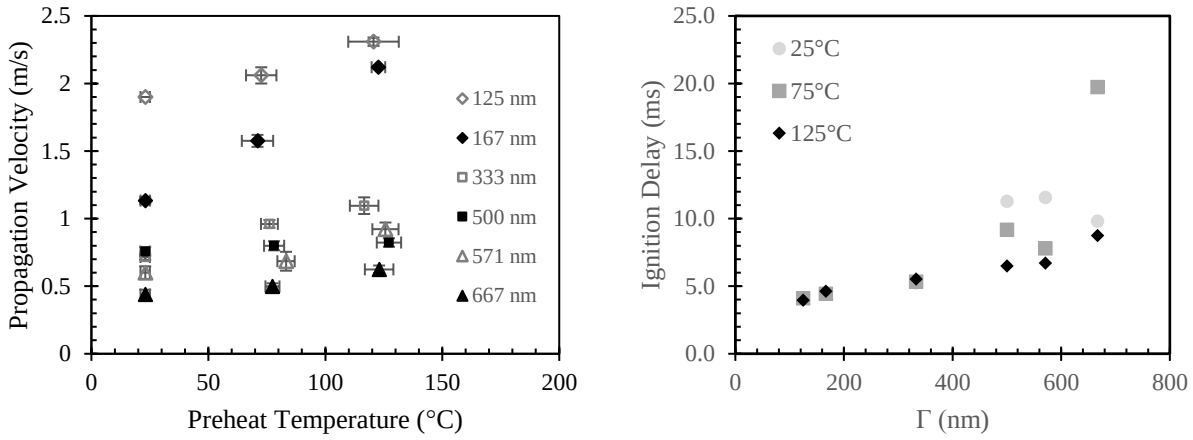

Figure 5.9. (Left) Propagation velocity and (right) time to first light as a function of preheat temperature for bilayer thicknesses ranging from 125-667 nm. Note how the ignition delays at bilayer thicknesses below 400 nm are less dependent on preheating.

Material that reacted under vacuum during deposition was evaluated using cross-section TEM. A focused ion beam (FIB) was used to create a thin specimen that allowed the final product phase to be identified. Figure 5.10 shows the observed elemental maps and indicates that oxygen is mixed primarily with Al as well as large areas that are primarily Ni. Voids also indicate that a gas phase formed during reaction. STEM selected area diffraction (Appendix A) indicates that Al_2O_3 and Ni are the final products of this reaction, with the measured lattice parameters corresponding to a cubic alumina phase, either η or γ.

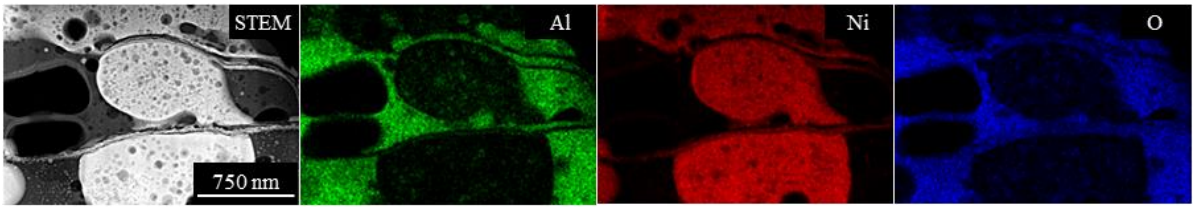

Figure 5.10. STEM and elemental maps of Al/NiO multilayer that reacted during deposition. Al (green) and O (blue) appear to occupy the same regions with Ni (red) in separate locations. Voids are present in products, indicating that a gas phase formed during product formation.

5.4 Discussion

5.4.1 Phase Evolution Subject to Low Heating Rates

The effect of varying heating rate on the reaction kinetics of thermite RMTF is currently unknown. As such, this discussion seeks to address the behavior of the Al-NiO system at a wide range of heating rates. In this section, we begin with a limiting case where slow growth of product phases passivates the interface. Following the discussion of the kinetics of interface growth, we discuss the kinetics of ignition at two different heating rates (~10^2 K/s and 10^5 K/s). We then conclude with observations about the behavior of self-propagating reactions (~10^7-10^8 K/s) and a general discussion about the reaction behavior of the Al-NiO system at heating rates spanning at least 8 orders of magnitude.

The formation of nickel aluminides during HS-XRD suggests that Ni diffusion outpaces oxygen diffusion, as it is unlikely that Ni would reduce aluminum oxide. This is similar to what has been observed in the Al-CuO_x system [107]. The formation of intermetallics, particularly $NiAl_3$ at 200°C as observed through HS-XRD of the 125 nm Al/NiO, indicates that reactions observed in the solid state through DSC are the result of Al reducing NiO to form Al_xO_y and Ni with diffusion of Ni into the Al matrix, as commonly observed in the Ni-Al system [116,117]. It is well known that in the initial stages of aluminum oxidation the oxide is amorphous, and transitions through a series of metastable phases to form α-Al_2O_3 at higher temperatures [118]. As a result, the lack of peaks for any oxides along with the sample remaining intact throughout the experiment suggests growth of an amorphous aluminum oxide, denoted Al_xO_y. The lack of exotherms at low temperatures in the 666 and 800 nm bilayer materials, as well as the Al reflection persisting to 500°C in the HS-XRD (excluding the 125 nm bilayer thickness), suggests that the initial reaction forming $NiAl_3$ for all bilayer thicknesses (as seen in Figure 5.6) is the result of a diffusion limited reaction confined to a region near Al/NiO interfaces.

Previously, DSC and XRD of quenched samples have been used in conjunction to infer phase formation related to sharp exotherms (particularly in binary systems) [116]. However, the DSC response of the Al/NiO RMTF appear to be more complex, with broad exotherms corresponding to the formation of several phases including nickel aluminides, metallic Ni, and aluminum oxides. By plotting the normalized integrated intensity of the NiO (111) reflection for different multilayer designs (Figure 5.11), it becomes apparent that reaction occurs in 3 separate stages, schematically presented in Figure 5.12. Stage 1 (Figure 5.12a) is an incubation period

with little change in peak intensity up to approximately 200°C. After this, stage 2 (Figure 5.12b) is characterized by the formation of $NiAl_3$ reflections at the expense of NiO and Al. This is then followed by stage 3 (Figure 5.12c), were a rapid decay in the intensity of the (111) peak correlates with the appearance of peaks for metallic Ni as well as the formation of Ni_2Al_3 in the 125 nm and 167 nm bilayer thickness multilayers (Figure 5.12c). In the 125 nm bilayer thickness, crystalline Al reflections are longer observed by 440°C, suggesting that it has been completely converted into intermetallic or oxide phases. It is impossible to tell from the results what side of the interface the metallic Ni forms on during stage 3. However, given the increase in the Ni_2Al_3 reflections at the expense of $NiAl_3$ in the finer bilayer thicknesses it is reasonable to suggest that Ni is 'piling up' on the NiO side of the interface with transport limited by an aluminum oxide product layer, since Ni transported to the Al layer forms nickel aluminide.

The presence of an exotherm at 560°C for all bilayer thicknesses (as observed in Figure 5.4) suggests a process that is independent of bilayer thickness. This temperature corresponds reasonably to the transition temperature of a-Al_2O_3 to γ-Al_2O_3 observed in thermogravimetric analysis (TGA) of aluminum powders [118]. In this previous work, an increase in mass gain was observed at 550°C which correlated with recovery XRD showing the formation of γ-Al_2O_3. It was suggested that the volume reduction (3.05 g/cm^3 to 3.6 g/cm^3) [119] could result in cracks forming in the passivating oxide shell, exposing fresh Al to the oxidizing atmosphere. It is suggested that the exotherm observed at 560°C is the result of a similar process, where Al_xO_y transitions to γ-Al_2O_3 and the corresponding volume reduction results in the formation of diffusion paths that have a smaller barrier to diffusion, enabling transport of Ni and O to the Al layer. Unfortunately, the peak temperature in the HS-XRD setup was limited to 500°C.

The strong endotherm observed in DSC of the 667 nm and 800 nm bilayer thickness multilayers corresponds to the melting of Al. The lack of this endotherm in the 125 nm design further confirms the observation from HS-XRD that Al has been completely consumed through solid state reactions in this multilayer design. Above the melting point of Al, there is a series of exotherms of unknown origin followed by a strong exotherm above 700°C in the 667 nm and 800 nm bilayer thickness designs. The lack of this exotherm in the 125 nm design suggests that it may result from the formation of nickel aluminum intermetallics; however, further verification of this is required.

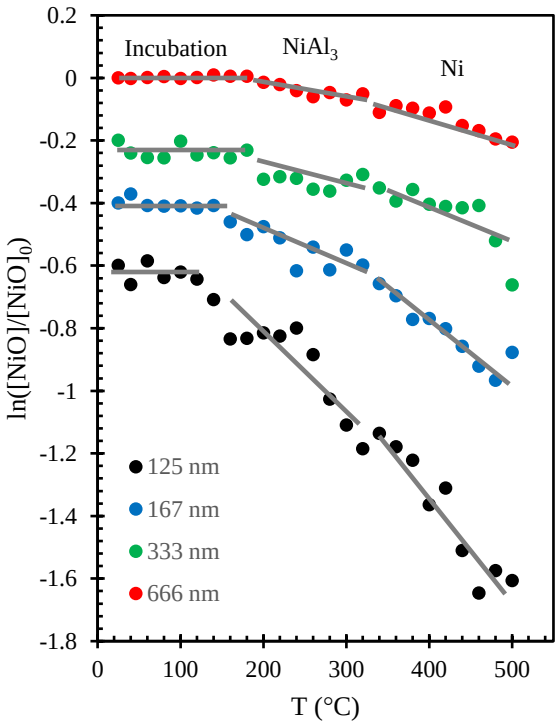

Figure 5.11. Plot of the ratio of the normalized NiO (111) integrated reflection intensity for the bilayer thicknesses examined through HSXRD. Intensities have been shifted vertically in increments of -0.2 for viewing. The gray lines are intended as visual aids.

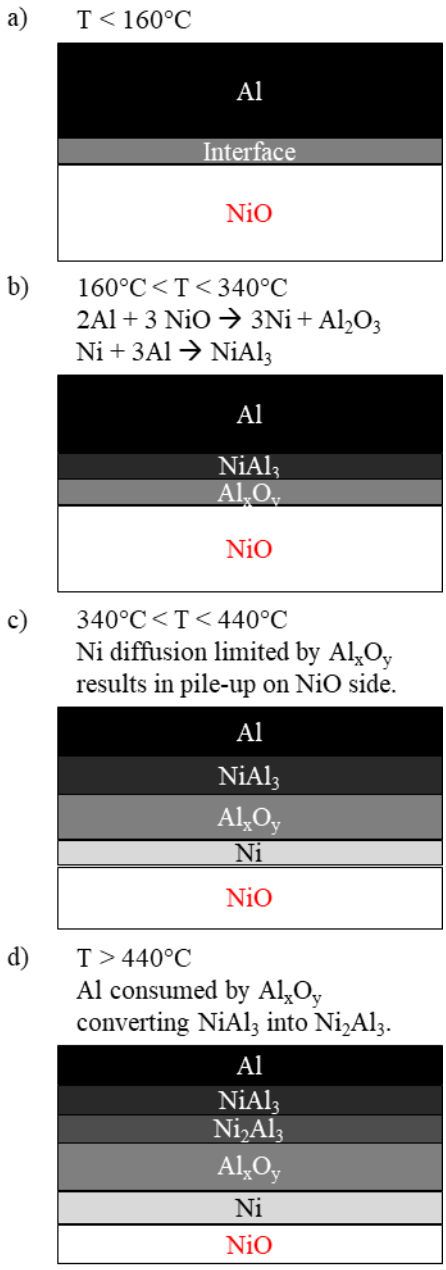

Figure 5.12. Schematic representation of 1D phase evolution expected at the Al/NiO interface for large bilayer thicknesses at low heating rates up to 500°C.

5.4.2 Low Heating Rate Activation Energy

During XRD, the diffracting volume is proportional to the integrated peak intensity, $V_{NiO} \propto [NiO]$. In a multilayer system, assuming planar, one dimensional, diffusional limited reaction, $V_{NiO} \propto t_{NiO}$. Since the initial NiO layer thickness is known, the data presented in Figure 10 can be used to determine the NiO layer thickness at a given temperature observed during heating through the following equation,

$$\frac{[NiO]}{[NiO]_0} = \frac{V_{NiO}}{V_{0,NiO}} = \frac{t_{NiO}}{t_{0,NiO}}. \tag{5.1}$$

Since there was no evidence of outgassing or crazing during the HS-XRD, it is safe to assume that there is negligible loss of oxygen to the surroundings. As a result, the reduction in the thickness of the NiO layer with temperature, combined with the conservation of mass, can be used to determine the growth of an Al_xO_y product layer. Assuming that the product phase is a-Al_2O_3 with a density of 3.05 g/cm^3 [119], and a 3:1 ratio of oxygen atoms to moles Al_xO_y the thickness of the oxide layer is given by

$$t^{Al_xO_y} = t_0^{Al_xO_y} + \frac{1}{3}\frac{\rho^{NiO}}{\rho^{Al_xO_y}}\frac{MW^{Al_2O_3}}{MW^{NiO}} t_0^{Al_xO_y}\left(1 - \frac{[NiO]}{[NiO]_0}\right). \tag{5.2}$$

with ρ and MW being density and molecular weight respectively. The initial thickness of the oxide layer is taken from the EDS trace presented in Figure 3 to be 5 nm, and assumed to be representative of the interface for all bilayer thicknesses. The calculated oxide thicknesses are presented in Figure 5.13. As can be seen, the independence of the calculated oxide thickness with bilayer thickness is physically consistent with a diffusion limited reaction mechanism and serves to justify some of the assumptions made in equations (1) and (2), as well as the observations in the previous section being limited to the reaction interface.

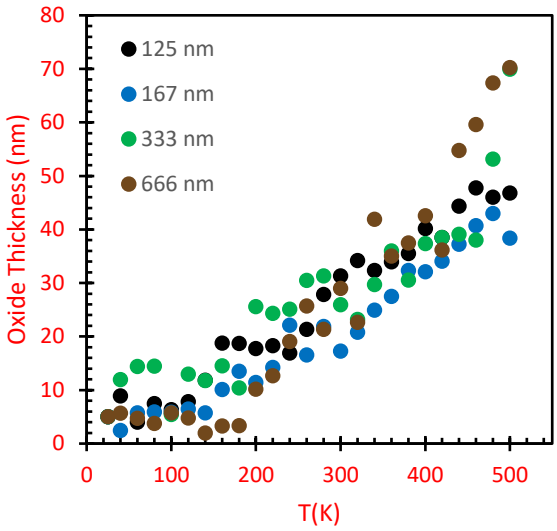

Figure 5.13. Calculated oxide thickness as a function of temperature.

Given that the hold time during each scan is 32 minutes and the step size is 20°C, it is expected that a steady state is reached at each step and the HS-XRD data represents a limiting case for the given temperature with the oxide layer self-passivating as observed in gas phase oxidation of aluminum [120]. Several works have indicated that thermite multilayers are limited by the diffusion of oxygen from the oxide into the Al [107,121]. In this case, the growth of the oxide layer, w, is described by a parabolic growth law given by

$$\frac{dw}{dt} = \sigma_{Al_2O_3} \frac{[O]}{w} D_0 \exp\left(-\frac{E_a}{RT}\right), \tag{5.3}$$

where $\sigma_{Al_2O_3}$, $[O]$, D_0, E_a, and R are the volume growth of Al_2O_3 per O ion, the initial O concentration gradient (assumed to be linear), mass diffusivity, activation energy, and ideal gas constant. Defining limiting thickness, w_{lim}, as the point where the growth rate at the limited thickness, $\frac{dw}{dt}$, is equal to $10^{-15}\frac{m}{s}$ as in Juergens et al. [120] the following equation can be derived

$$\ln w_{lim} = -\frac{E_a}{RT} + \ln\left(\frac{10^{-15}\frac{m}{s}}{\sigma_{Al_2O_3}[O]D_0}\right). \tag{5.4}$$

As indicated by equation (5.4), a linear relation is predicted between the natural log of the limiting oxide thickness and the inverse of the temperature, with the slope of the curve being the ratio of the activation energy to the universal gas constant. Taking the growth rate as 10^{-15} m/s is the same as assuming that the growth at the interface is independent of bilayer thickness at these

heating rates, which is justified up to the point that a reactant layer is fully consumed. A plot of the $\ln(w_{lim})$ vs $1/T_{ig}$ for the 125 nm bilayer thickness is presented in Figure 5.14.

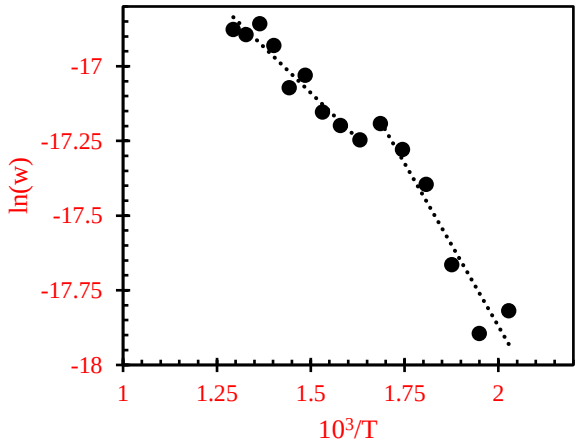

Figure 5.14. Plot of the natural log of the limiting oxide thickness versus temperature. The plot shows a bilinear response with a discontinuity at approximately 320°C.

As can be seen in Figure 5.14, the ln(w) for the 125 nm bilayer thickness is bilinear when plotted against inverse temperature. This response is observed in the 166 nm and 667 nm bilayer thicknesses as well, while the response of the 333 nm bilayer thickness was too noisy at lower temperatures to accurately evaluate a slope. Table 5.2 presents the activation energies determined from the slopes fitted to the low temperature region (200°C to 320°C) and the high temperature region (340°C to 500°C).

Table 5.2. Activation energies fit to HSXRD data. The uncertainty, σ, is determined from the standard deviation in the slope.

λ (nm)	200-320°C		340-500°C	
	E_a (kJ/mol)	σ (kJ/mol)	E_a (kJ/mol)	σ (kJ/mol)
125 nm	18.8	3.0	10.4	1.1
166 nm	16.9	6.8	14.3	1.5
333 nm	----------	----------	17.6	3.1
667 nm	24.4	4.4	20.2	3.5
Average	20.0	6.1	15.6	4.8

The transition in slope observed in Figure 5.14 corresponds to the transition from stage 2 to stage 3 in the HS-XRD. It is interesting to note that both the onset of reaction and the transition point at 320°C correlate with the measured DSC onsets for the formation of $NiAl_3$ (near 200°C) and Ni_2Al_3 (near 330°C) for Ni/Al multilayers with bilayer thicknesses of 23 nm and 58 nm [122].

5.4.3 Activation Energy for Hot-plate Ignition

While the HS-XRD and DSC heating was dictated by the experimental setup at all stages, the hot-plate experiments are not. The initial heating rate is determined by the temperature of the hot plate; however, after ignition it is governed by self-heating. The hot plate ignition experiments showed a bilayer thickness dependence on whether ignition is dependent on the melting of Al. The HS-XRD and DSC showed that this system forms product phases in the solid state given sufficient time for reaction, and suggest the formation of Al_xO_y and $NiAl_3$ independent of Al melting at the lowest heating rates. However, the exact phase formation sequence is expected to be heating rate dependent [123,124]. While solid state reaction has been observed through calorimetric studies for thermites previously [103,107,113], none of these previous studies investigated the ignition of the thermites in question. The examination of hot plate ignition temperatures allows a distinction between a region where melting of Al is required for ignition to occur and a region where ignition occurs in the solid state. This is analogous to what has been termed as a ‘micro-scale’ and ‘nano-scale’ response in powder systems and other RMTF [95,103]. Since reaction is diffusion limited, the amount of reacting material is limited to that within a characteristic diffusion length from an Al/NiO interface. In the case of large bilayer thicknesses, the specific interfacial surface area (interfaces per unit volume) are limited. As the bilayer thickness decreases, the specific interfacial surfaces area increases, allowing a larger fraction of the volume to react before a passivating boundary can form at the interface. In the case of large bilayer thicknesses, the heating rate is not sufficient to result in thermal runaway before a diffusion limiting layer can form, preventing further reaction. In hot plate ignition of Al/NiO RMTF this transition occurs between the 306 and 333 nm bilayer thicknesses.

The dependence of ignition temperature on bilayer thickness allows determination of an effective activation energy corresponding to solid state mixing. The following is identical to the

derivation from Fritz et al. [71] except for the use of a different growth law for the product phase formed. The energy equation gives the following

$$C\dot{T} = \dot{Q}_s + \dot{Q}_{RXN} - \dot{Q}_L, \tag{5.5}$$

where C is the laminate heat capacity, and the right side of the equation consists of the heat input from the laser ($\dot{Q}_s$) and reaction ($\dot{Q}_{RXN}$) and a loss term ($\dot{Q}_L$). As in Fritz et al. [71], we define T_{ig} as the point at which the temperature increases without any contribution from an external source. This results in an inflection point where the foil has equilibrated to the temperature of the source (i.e. $\dot{Q}_s = 0$) and the heating rate is momentarily zero. At this instant, equation (5.5) reduces to

$$\dot{Q}_{RXN} = \dot{Q}_L. \tag{5.6}$$

The thermal losses ($\dot{Q}_L$) can be modelled as a combination of conductive (Cond) and convective (Conv) losses and is given as the following equations for a hot plate experiencing unforced convection

$$\begin{aligned} \dot{Q}_{Cond} &= \frac{k}{t}\frac{\Delta T}{\Delta x} = \frac{1}{tR_{Cond}}\Delta T \\ \dot{Q}_{Conv} &= \frac{1.32}{tL^{\frac{1}{4}}}\Delta T^{\frac{5}{4}} = \frac{1}{tR_{Conv}}\Delta T^{\frac{5}{4}} \\ \dot{Q}_L &= \frac{1}{tR_{cond}}\Delta T + \frac{1}{tR_{Conv}}\Delta T^{\frac{5}{4}} = \frac{1}{tR_t}\Delta T^m, \end{aligned} \tag{5.7}$$

where k, t, h, ΔT, Δx, and L are the thermal conductivity, sample thickness, convective heat transfer coefficient, temperature difference with the local surroundings, thickness of the thermal interface, and characteristic length scale such as the ratio of perimeter to area. The R terms are thermal resistance with R_t being the combined resistance resulting from convective and diffusive losses. The exponent m varies from 1.0 for purely conductive losses to 1.25 for purely convective losses.

The reaction term in equation (5.8) takes the form

$$\dot{Q}_{RXN} = \frac{dw}{dt}\frac{\Delta H_{RXN}}{\frac{\lambda}{2}}, \tag{5.8}$$

where w is the thickness of the product phase formed and ΔH_{RXN} is the heat of reaction. The growth of the product phase thickness is assumed to follow a parabolic growth law limited by thermal diffusion of oxygen ions through an Al_2O_3 product phase and is given by equation (5.3). Substituting equations (5.3), (5.7), and (5.8) into equation (5.6) and evaluating at T_{ig} can be shown to result in the following equations,

$$\exp\left(-\frac{E_a}{RT_{ig}}\right) = \frac{w}{2\Delta H_{RXN}\sigma_{Al_2O_3}C_O D_0}\,\frac{1}{tR_t}\left(\lambda\Delta T_{ig}^m\right). \tag{5.9}$$

$$ln\left(\lambda\Delta T_{ig}^m\right) = -\ln\left(\frac{w}{2\Delta H_{RXN}\sigma_{Al_2O_3}C_O D_0}\,\frac{1}{tR_t}\right) - \frac{E_a}{RT_{ig}}. \tag{5.10}$$

It can be seen that equation (5.11) represents a linear relation between $ln\left(\lambda\Delta T_{ig}^m\right)$ and $1/T_{ig}$ with the slope being $-E_a/R$ and that this value is independent from the intercept. Figure 5.15 shows the results of this analysis performed on the measured values of hot plate ignition temperature. The activation energy, E_a, resulting from this analysis is calculated to be 36-38 kJ/mol with R being 8.314 J/mol-K.

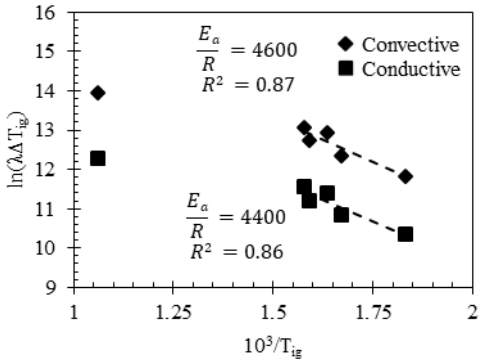

Figure 5.15. Fits for activation energy based on ignition temperature as a function of bilayer thickness. Note that only the three points to the right (with T_{ig} below the melting point of Al) are used in the analysis with the left point being included to emphasize the change in reaction mechanism.

5.4.4 Activation Energy for Laser Ignition

Laser heating provides a controlled way to probe the reaction kinetics that govern ignition at characteristic heating rates of approximately 10^5 K/s. The plot in Figure 5.15 indicates a discontinuity between the lower bilayer thicknesses and the highest bilayer thickness that ignited (333 nm). Since all bilayer thicknesses tested were found to be self-propagating, this

indicates that the ignition temperatures were in excess of the highest temperature tested (800°C). It is possible to estimate the difference in the ignition temperatures at varying bilayer thicknesses from the observed ignition delays presented in Figure 5.9. Starting from equation (5.5), it is assumed that negligible reaction occurs before ignition ($\dot{Q}_{RXN} = 0$). The length scale for thermal diffusion is given by $x \propto (\alpha t)^{1/2}$ by a mass averaged thermal diffusivity for Al/NiO (42 mm2/s) and a time on the order of the measured ignition delays (1-10 ms). This gives 0.2-0.6 mm, which is on the order of the beam diameter. As a result, at the center of the beam diameter it is expected that the temperature gradient is small compared to the source term due to the small Biot number and assuming a limited degree of thermal and chemical diffusion. Additional losses due to free convection are assumed to be small as well. Assuming that reaction is negligible before ignition, equation (5.5) can be simplified to the following form,

$$C(T)\dot{T} = \varepsilon P_l, \tag{5.11}$$

where ε and P_l are the NiO emissivity and laser irradiance respectively. Assuming variations in the heat capacity is small up to the melting point of NiO (1966°C), equation (5.11) can be integrated assuming a constant emissivity, resulting in

$$(T_{ign} - T_0) = \frac{\varepsilon}{C} P_l t_d. \tag{5.12}$$

By dividing equation (5.12) by a reference condition, the following ratio allows determination of the change in T_{ign} as a function of ignition delay (T_d):

$$\frac{T_{ign} - T_0}{\left(T_{ign} - T_0\right)_{ref}} = \frac{P_l t_d}{(P_l t_d)_{ref}} \tag{5.13}$$

At the point of ignition, heating due to the runaway reaction should overwhelm heating from the laser, with negligible conductive losses as in equation (5.12) and ignoring the laser heating source term, equation (5.5) becomes

$$C\dot{T} = \dot{Q}_{RXN} = \frac{\Delta H_{RXN}}{\frac{\lambda}{2}} \sigma_{Al_2O_3} \frac{[O]}{w} D_0 \exp\left(-\frac{E_a}{RT}\right). \tag{5.14}$$

For a non-reacting heating at a constant laser intensity, the heating rate leading into ignition is a constant for all bilayer thicknesses. In this case, equation (5.15) can be rearranged to show

$$\ln(\lambda) = \ln\left(\frac{\Delta H_{RXN}}{C\dot{T}} \sigma_{Al_2O_3} \frac{[O]}{w} D_0\right) - \frac{E_a}{RT_{ign}}. \tag{5.15}$$

The assumption of negligible reaction before ignition results in all terms in the above equation being constants except for T_{ign} and λ. Substitution of the ratio in equation (5.14) into equation (5.16) allows the activation energy to be determined directly from ignition delays, as follows

$$\ln(\lambda) = \ln\left(\frac{\Delta H_{RXN}}{C\dot{T}}\ \sigma_{Al_2O_3}\frac{[O]}{w}D_0\right) - \frac{E_a}{R}\left(\frac{1}{T_0+\left(T_{ign}-T_0\right)_{ref}\frac{P_l t_d}{(P_l t_d)_{ref}}}\right). \tag{5.16}$$

Since ignition temperatures were not directly measured, a reference T_{ign} was assumed for the 125 nm bilayer thickness and the analysis was carried out for ignition temperatures between the hot plate ignition temperature, 550 K, and 1200 K. It will be shown that reasonable assumed values of this initial ignition temperature results in small changes in the calculated activation energies. Temperatures above 1060 K were found to result in predicted ignition temperatures for the larger bilayer thicknesses approaching the vaporization temperature of Al, which represents a reasonable upper limit, as vaporization of Al was not observed during ignition. Figure 5.16 presents this analysis performed with initial temperatures of 550 K, 800 K, and 1060 K. First, it is apparent that two reaction regimes exist with the 125-333 nm bilayer thickness designs reacting through one mechanism and the 500-671 nm designs reacting through another. Second, the activation energy for the mechanism governing the lower bilayer thicknesses is greater than that governing the larger bilayer thicknesses. The activation energy of the lower bilayer thicknesses is bound between 46 and 51 kJ/mol as calculated assuming reference ignition temperatures of 550 K and 1060 K respectively. The activation energy governing the ignition of the larger bilayer thicknesses under these same conditions is between 26 and 33 kJ/mol. It is interesting to note that the activation energy governing the ignition kinetics of Al-CuO nanolaminates through laser ignition was iteratively determined to be approximately 49 kJ/mol at a heating rate of 10^5 K/s, indicating that the low activation energies observed here are consistent with previous work on thermites [121].

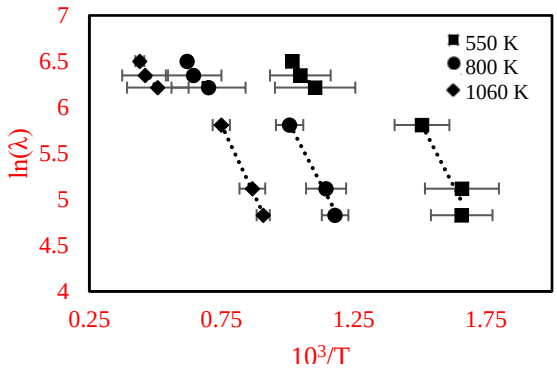

Figure 5.16. Analysis of activation energy for various assumed reference ignition temperatures showing a delineation between two reaction mechanisms where designs with bilayer thicknesses greater 333 nm reacting with one mechanism and designs with bilayer thicknesses equal to or less than 333 nm reaction in another.

5.4.5 Self-Propagating Reactions in Multilayer Thermites and a Length Scale Dependence in Behavior

Whether the reaction kinetics observed at different heating rates relate to the high heating rates observed in a self-propagating reaction front has been a long-standing question in the field of condensed phase reactives. The processes governing ignition and propagation in a condensed phase reaction can rarely be attributed to a single reaction mechanism and are a combination of fundamental reaction processes and phase transformations (i.e. melting, solid-solid transformations). As a result the activation energy measured for a given condensed phase reaction event is effective in nature, spanning a series of processes that occur at their individual rates. Therefore, it is possible that the activation energy for a rate limiting process is very much dependent on the heating rate in RMTF. This section seeks to evaluate the capability of the current analytical theory for condensed phase RMTF to predict the behavior of multilayer thermites as well as address what behaviors observed at intermediate heating rates (heating rates observed in hot-plate and laser ignition) translate to the behavior of self-propagating reactions.

In Armstrong and Koszykowski [125], the following quadratic relationship between propagation velocity and bilayer thickness is given as:

$$u^2 = \frac{3Ae^{-\frac{E_a}{RT_f}\left(\frac{RT_f}{E_a}\right)\alpha^2}}{\delta^2\frac{\left(T_f-T_0\right)}{T_f}}, \tag{5.17}$$

where the inverse Lewis number, Le^{-1}, has been assumed to follow an Arrhenius dependence

$$Le^{-1} = \frac{D}{\alpha} = A\mathrm{e}^{-\frac{E_a}{RT_f}}, \tag{5.18}$$

with propagation velocity, u, Arrhenius prefactor, A, initial temperature T_0, flame temperature T_f, thermal diffusivity, α, mass diffusivity, D, and quarter bilayer thickness, $\delta = \lambda/4$. While subsequent studies have illustrated the need to account for the intermixed zone formed during deposition [126,127], this relationship has been shown to reasonably predict the propagation velocity in metallic RMTF at bilayer thicknesses much larger than the premixed zone. Considering that the ratio of all bilayer thicknesses to the intermixed region observed in Figure 5.3 are above 10, the effect of premixing was expected to be negligible.

For a fixed bilayer thickness and mixing mechanism, all terms in equation (5.15) are constant except T_f and T_0. As a result, the ratio of the propagation velocity at an elevated temperature to the propagation velocity at room temperature is found to be

$$\frac{u^2}{u_{RT}^2} = e^{-\frac{E_a}{R}\left(T_f^{-1} - T_{f,RT}^{-1}\right)} \frac{T_f^2}{T_{f,RT}^2} \frac{(T_f - T_0)_{RT}}{(T_f - T_0)}, \tag{5.19}$$

where the subscript RT has been used to refer to the values for a propagation foil with T_0 = 296 K. Recent work has shown that Al-CuO thermites can be numerically modelled through the utilization of a 'ceiling' temperature referencing the vaporization temperature of Cu_2O as a cutoff point, at which energy is lost to the environment through disintegration of the multilayer [128]. The model was shown to reasonably match experimental propagation velocities and ignition delays.

If a ceiling temperature (T_c) is utilized with Armstrong's solution, equation (5.17) reduces to

$$\frac{u^2}{u_{RT}^2} = \frac{(T_c - T_0)_{RT}}{(T_c - T_0)}. \tag{5.20}$$

Solving for T_c with the measured values from Figure 5.9 results in unreasonably low values for T_c (below 700 °C) for all bilayer thicknesses. Setting T_c to the vaporization temperature of Al (2790 K) in equation (5.18) predicts changes in propagation velocity with initial temperatures of 75°C and 125°C compared to 23°C of only 1-2%, which is, at minimum,

an order of magnitude lower than what is observed in Figure 5.8. This difference is only made worse by using the vaporization temperature of Ni (3187 K). Furthermore, given the small change in initial temperature compared to expected flame temperatures, the expected flame temperature would be expected to be on the same order of magnitude as the As a result, current analytical methods of evaluating the propagation velocity of condensed phase RMTF appear to be inadequate to describe the propagation of thermite multilayers, particularly the temperature dependence.

An important characteristic of equation (5.15) is that is that u^2 is inversely related to δ^2. Figure 5.17 presents u^2 as a function of $1/\delta^2$. It is evident from this plot that the propagation velocity scales with reducing bilayer thickness; however, the relationship is bilinear for 25° and 75°C preheat temperatures, with a change in slope between the 333 nm and 500 nm bilayer thicknesses with the larger bilayer thickness region enclosed by the dashed line in Figure 5.17. The slope of the higher bilayer thicknesses is greater compared to the slope for the region of finer bilayer thicknesses. Additionally, a fit curve to both regions have non-negligible intercepts. At a preheat temperature of 125°C, the bilinear behavior is not as apparent; however, this may be a result of the uncertainty in the initial temperature coupled with the sensitivity in propagation velocity with preheat temperature. The characteristic reaction time for a propagating front can be approximated as the ratio of the thermal diffusivity to the squared propagation velocity, or $\Delta t \sim \alpha/u^2$. Taking a change in temperature across the front to be between 2600-2800 K with an in plane thermal diffusivity based on a rule of mixtures of 42 mm^2/s, the characteristic heating rate is found to be between 10^7 and 10^8 K/s for these propagating thermite reactions.

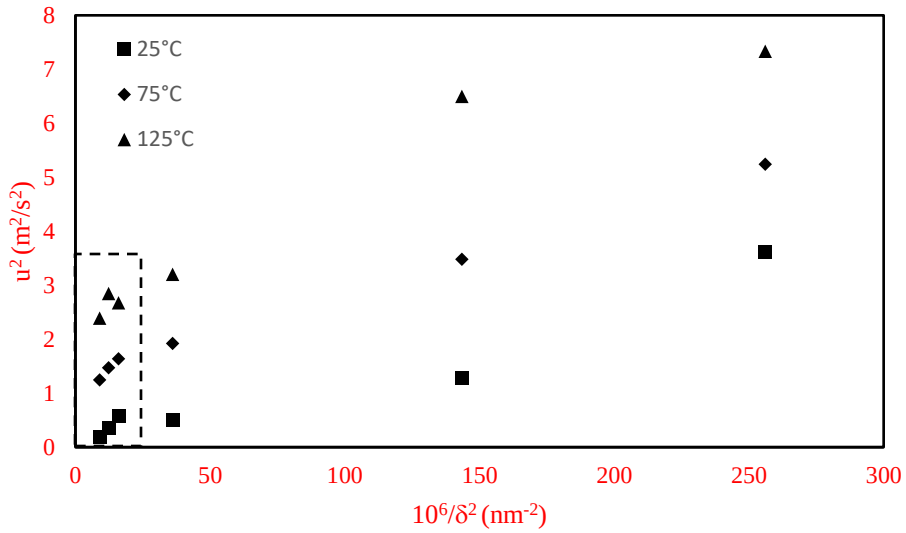

Figure 5.17 Plot of squared propagation velocity (u) versus the inverse of the squared quarter bilayer thickness (δ) showing that bilayer thicknesses suggesting that reaction velocity is again divided into two regimes. The lower propagation regime, indicated by the dashed box, exhibits a different scaling with δ than that of bilayer thicknesses of the higher regime, suggesting a change in mixing mechanisms. The values for preheat temperatures of 75°C and 125°C have been offset for clarity.

5.4.6 Reaction Behavior at Different Heating Rates

A summary of the measured activation energies as a function of the source heating rate is presented in Table 3. It is included here for interest and summary; however, the activation energies determined at low heating rates corresponding to the growth of an Al_xO_y should not be directly compared to the activation energies determined for ignition, as the energy jumps associated are not necessarily for the same process.

For both the hot plate ignition experiments and the laser ignition experiments, the ignition behavior is separated into two separate regimes. In the hot plate ignition experiments, the division results from multilayers with bilayer thicknesses below 333 nm having a large enough number of interfaces that reaction occurring through solid state diffusion mechanisms is enough to induce ignition below the melting point of Al and those that require the increased mobility resulting from the melting of Al for ignition to occur. The characteristic heating rate of hot plate ignition is approximately 10^2 K/s, and this results in an activation energy for the processes governing solid state ignition of 37.4 kJ/mol for bilayer thicknesses 306 nm and below. If the heating rate is increased to approximately 10^5 K/s, the characteristic heating rate of the ignition

experiments, the reactions governing ignition for bilayer thicknesses below 333 nm has increased to 48.5 kJ/mol. If the same mechanism limited the reactions at higher rate as at lower heating rates, the activation energy would be identical; however, given how low the activation energy is for the hot plate experiments, a significant shift in peak temperature would be expected with a change in heating rate of 3 orders of magnitude. Kissinger's analysis [129] relating heating rate and activation energy can be used to estimate a shift in ignition temperature with heating rate through the following relation,

$$\frac{d\left(\frac{\varphi}{T^2}\right)}{d\left(\frac{1}{T}\right)} = -\frac{E_a}{RT}, \tag{5.21}$$

where φ is the heating rate. A reaction occurring at 275°C at 102 K/s with an activation energy of 37 kJ/mol would shift to approximately 1370°C at a heating rate of 10^5 K/s. Comparably, a reaction pathway independent of the previously discussed reaction occurring at a higher temperature at lower heating rates, but with a higher activation energy would shift less with heating rate and could become dominant. As a result, at higher heating rates, higher activation energy mechanisms may become limiting.

Additionally, the activation energy decreasing with an increase in bilayer thickness can be explained by a transition from a solid state ignition mechanism to a melt dependent mechanism, a reduced activation energy would be expected as a result of the increased mobility of a liquid compared to a crystalline phase.

Table 5.3 Summary of measured E_a.

	E_a (kJ/mol)	σ (kJ/mol)
HS-XRD 200-320°C	20.0	6.1
HS-XRD 340-500°C	15.6	4.8
Hot Plate	37.4	1.5
Laser 125-333 nm	48.5	2.5
Laser 500-671 nm	29.5	3.5

While the results indicate that even a change from 10^2 K/s (hot-plate) to 10^5 K/s (laser) resulted in a 60% increase in activation energy, a length scale dependency is observed across all

heating rates beyond the self-limiting case (HS-XRD). For the hot-plate ignition experiments, Figures 7 and 15 show that reaction occurs under a solid-state reaction mechanism for bilayer thicknesses below 333 nm with melt dependent reaction for laminates with a thickness 333 nm and above. Increasing the heating rate to 10^5 K/s results in RMTF with bilayer thicknesses 333 nm and below to react through the same mechanism with an increased activation energy compared to that observed in the hot-plate experiments. Figure 16 would indicate that the activation energy of the process limiting ignition is observed to decrease with increased bilayer thicknesses. This suggests a process occurring (a phase transformation, such as melting in the case of the hot-plate experiments) that provides a reaction pathway with a reduced energy barrier for ignition to occur at larger bilayer thicknesses. This transition is found to occur at a bilayer thickness between 333 nm and 500 nm at heating rates on the order of 10^5 K/s. This behavior appears in the propagation velocity as well, persisting up to heating rates of approximately 10^7-10^8 K/s. While the exact nature of the change in reaction mechanism cannot be determined at this time for the higher heating rate conditions, it is interesting to note the correlation between the length scale where the transition occurs and the heating rate.

5.5 Conclusions

The reaction mechanism, ignition behavior and self-propagating reaction of Al-NiO RMTF have been examined. The results show two regions of behavior as a function of bilayer thickness. At larger bilayer thicknesses ignition and exothermic release occur above the melting point of Al and propagation velocities having little dependence on the bilayer thickness, similar to micron-scale reactives. Finer bilayer thicknesses exhibit ignition and substantial exothermic release below the melting point of Al. The transition point between these two regions is heating rate dependent and occurs between 300-500 nm at the heating rates studied in this work.

Examination of the phase evolution and heat release at low heating rates through HS-XRD and DSC revealed that formation and growth of nickel aluminides and Al_xO_y result in significant exothermicity below the melting point of Al. The first crystalline phase to form is $NiAl_3$ at 180°C with Al_xO_y expected to form as well. This initial phase of reaction continues until approximately 320°C at which point crystalline Ni is observed in all examined designs and Ni_2Al_3 all but the thickest bilayer thicknesses examined. These reactions result in a drawn out exotherm observed in DSC of the 125 nm bilayer thickness with an onset temperature of 200°C.

Analysis of the integrated peak intensity of the NiO(111) reflection in HS-XRD indicated a multi-stage reaction with incubation up to approximately 200°C, followed by a region characterized by the formation of $NiAl_3$ with an activation energy of approximately 20 kJ/mol. At approximately 320°C, the reaction transitions to a region characterized by the formation of Ni as well as Ni_2Al_3 with an activation energy of approximately 16 kJ/mol. In the 667 nm and 800 nm bilayer thicknesses, a significant melt endotherm was observed corresponding to the melting of Al. This was followed by a strong exotherm at approximately 700 °C. In the finest bilayer thickness examined, Al was completely consumed by 500°C in the HS-XRD, which was corroborated by a lack of an endotherm at 660°C in DSC and a lack of the strong exotherm observed at 700°C. This suggests that, in larger bilayer thicknesses and low heating rates, Ni reduced from the thermite reaction rapidly diffuses into the molten Al layer at 700°C.

Significant solid state reaction in DSC and the formation of $NiAl_3$ correlates with a significant reduction (300°C) in the hot plate ignition temperature to well below the melting point of Al. It is within reason to state that solid state reactions resulting the formation of $NiAl_3$ and Al_xO_y are what govern the ignition of Al-NiO RMTF with bilayer thicknesses below 300 nm. The activation energy for multilayers igniting below the melting point of Al (660°C) was found to be 37 kJ/mol. Laser ignition of the Al-NiO RMTF indicated a similar behavior with two regions of response as a function of bilayer thickness. The RMTF with finer bilayer thicknesses (those 333 nm and below) where found to have an activation energy of approximately 48.5 kJ/mol with a heating rate on the order of 10^5 K/s. The results indicate an increase in activation energy with heating rate.

Attempts to model the propagation of Al/NiO RMTF as a condensed phase propagation represented by Armstrong's solution at a far field temperature equal to a ceiling temperature set by the lowest vaporization point in the system is shown to not accurately predict the variation in propagation velocity with the initial temperature. This is taken as an indication of the inadequacy of Armstrong's equation to predict the behavior of thermite reactions, and points to the need for more sophisticated modelling to understand the propagation of these reactions [128,130]. However, the propagation velocity is observed to have a length scale dependence with two regions of reaction with RMTF with bilayer thicknesses 500 nm and above having a linear scaling between the squared bilayer thickness and squared propagation velocity and those

333 nm having a similar, but reduced scaling indicating a length scale dependent rate limiting step that spans a range of heating rates.

CHAPTER 6. SHOCK-INDUCED REACTION: DIRECT SYNTHESIS OF CUBIC BORON NITRIDE FROM A CONDENSED PHASE REACTION

A shockwave passing through a porous material results in a drastic increase in both pressure and temperature, which can induce solid-state polymorphic phase transformations [3], as well as shock-induced chemistry [4]. Detonation of a solid explosive is the most common example of shock induced chemistry, where, a shock wave propagates at a steady velocity and reaction travelling a short distance behind the shock sustains the propagation though acoustic feedback from the gas phase products. This rapid reaction is typically only possible in gas producing systems of energetic compounds; however, there has long been interest in whether a reaction can occur within a shockwave for a condensed phase reaction and form useful solid products [4,16].

Shock-induced reaction synthesis (SRS), which involves a combination of self-sustained, high-temperature (2000-3000 K) reactions and a shock wave, represents a unique method to produce advanced materials. SRS has been applied to many reactive systems resulting in the synthesis of a significant number of solid compounds including carbides [16,131], borides [132], silicides [133], and aluminides [35].

However, fundamentally there are two distinguishing cases for SRS [28]. In the first case, the shock wave heats the material enough that, after pressure release, the material reacts through a deflagration combustion wave with a characteristic reaction time on the order of several milliseconds. Numerous works have demonstrated the existence of such a route, through recovery experiments showing product formation after shock loading [31,32,36,134,135]. In the second case, a gasless reaction takes place directly in the shockwave within several microseconds [35,136]. In general, two methods have been suggested to prove the existence of such ultra-fast gasless reaction [137]. The more common approach involves in-situ measurement and comparison of the shock Hugoniot for reactive and inert mixtures that allows an inference of reaction occurring on the timescale of the shockwave [23,26,29,138,139]. The second approach is through the synthesis and recovery of a metastable phase, which can form only under high-pressure conditions. Throughout the history of SRS studies, this second approach has not been applied. The precise reaction conditions becomes even more intriguing for reactive systems with

an adiabatic combustion temperature (T_{ad}) below the melting points of all precursors, intermediates, and final products; a class of reaction known as the solid flame [140,141]. For such systems, solid-state mechanisms of mass transport govern the reaction process. The boron (B)-titanium nitride (TiN) system, investigated in this work, leads to the formation of boron nitride and adheres to the prerequisites for the solid flame class of reactions.

The high pressure behavior of boron nitride (BN) has fascinated researchers since the middle of the last century [53,142]. Being the second hardest known material, cubic BN (c-BN) possesses superior chemical and thermal stability (stable up to 1650 K), as compared to diamond (stable up to 950 K) [143], is rarely found in nature [144], and forms only under high-pressure and high-temperature (high P/T) conditions [142]. As a result, c-BN does not form below 6 GPa in quasistatic conditions [39] and is not expected below 12 GPa under shock loading [3]. It is important to note that a single shock loading of the hexagonal phase of BN (h-BN) results in a martensitic transformation to wurtzitic BN (w-BN) and not c-BN [43]. The thermal stability of c-BN makes it less susceptible to reversion to the graphitic form due to residual heat upon unloading as compared to diamond. This feature makes it a promising phase to use as an indicator to determine if reaction and product phase formation occurs during the shock.

In this work we provide direct evidence for the formation of the super hard c-BN as a result of shock-induced reactions using TiN as the nitrogen source for B. By this observation and taking into account that c-BN can be formed only at high P/T, we prove that under certain conditions condensed phase reactions may occur at ultra-fast rates in the time span 0.1-5 μs.

The reactive mixture of B and TiN at a 3:1 molar ratio was selected to synthesize c-BN under shock loading. Thermodynamic calculations show that BN and titanium diboride (TiB_2) are the equilibrium products for this exothermic reaction:

$$3B + TiN \rightarrow BN + TiB_2. \quad (6.1)$$

The calculated T_{ad} for the system is 1903 K, which is lower than the melting points of B (2353 K), TiN (3203 K), and TiB_2 (3503 K), as well as the dissociation temperature of BN (3246 K). This suggests that the considered 3B+TiN mixture is a solid flame system. Studies of this system have shown that, under locally initiated impulse heating, reaction front exhibits oscillatory propagation, and analysis of the product phase through XRD shows h-BN and TiB_2 to be the reaction products [145].

It was previously shown that direct SRS of BN from a virgin mixture of commercially available micron size beta-rhombohedral (β-r) B and TiN powders is essentially impossible, due to the high effective activation energy associated with mass diffusion kinetics for this solid-state reaction [145]. To overcome these difficulties, the reactivity was enhanced by the preparation of nanostructured composites through high-energy ball milling (HEBM) (see supporting information for material preparation).

XRD performed on the powder produced by this intensive mechanical treatment (Fig. 6.1a) reveals only TiN and β-r B phases, indicating that no other crystalline phases formed during the HEBM process. Electron micrographs show that the produced powder consists of micron scale composite particles (Fig. 6.1b), which consist of nanoscale (5-500 nm) crystallites of B suspended in a fine (10-100 nm) TiN matrix (Fig. 6.1c). These nanostructured B/TiN composite particles are highly reactive due to the significant increase in interfacial contact area and reduced diffusion distance as a result of the milling process (Fig. 6.1d). The parameters for the HEBM process as well as characteristics of initial reactants are listed in Table B.1.

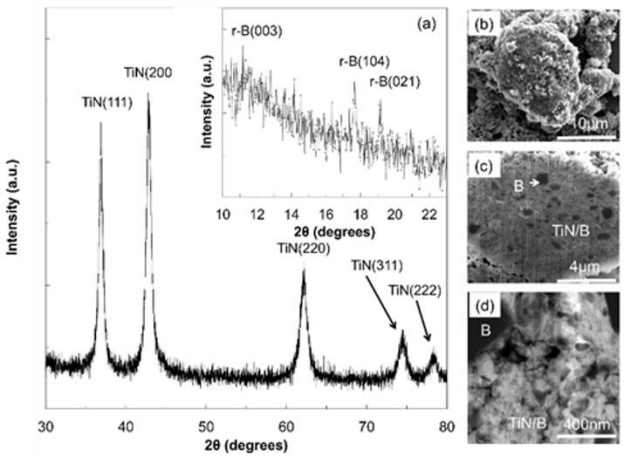

Figure 6.1. XRD data (a) and micrographs (b-d) for the initial HEBM material. SEM and STEM images of a composite particle (b) and particle cross-sections (c & d) in which the dark phase is B while the lighter phase is TiN.

The reactive nanocomposite powder was loaded into a recovery capsule (Fig. A.1) at a relative density of 50-55% and was shocked using approximately 25 g of PrimaSheet 1000 (a PETN based plastic explosive) to drive an outer copper shell at high velocities into a concentric copper tube that contained the powder. This method of powder compaction has been performed

in several configurations [5] and the particular design used was modeled after Meyers and Wang [21]. The capsule was selected to sustain the high pressure from the shockwave for a longer duration as compared to direct contact with an explosive [21]. After compaction, the diameter of the shocked portion of the capsule remained constant along the entire length, suggesting that the sample was loaded evenly (Fig. A.1). Simulations of the experiment were performed using a mixture equation of state developed using McQueen's mixture theory [81] from Hugoniot data for B [89] and TiN [146] in CTH [147] and are described in the supplemental material. The results indicate that the peak pressure achieved in the experiments is in the range of 15-20 GPa (Fig. A.2). A release time constant (τ) is taken for a shock to transit the thickness of the flyer twice. For a shock velocity between 4-6 km/s and a 2 mm flyer thickness, the time constant would be $\tau \sim 0.8\text{-}1.0$ μs. The pulse width Δt is estimated to be $5\tau = 4\text{-}5$ μs. This result is in line with the 1-2 μs pulse width observed in the simulations (Fig. A.2).

Both XRD and SEM/TEM data confirm the formation of c-BN as a result of SRS. We examined the crystallographic parameters (d-spacing, Miller indices, reflection angles and relative intensities) of the initial compounds (β-r B, TiN) and possible phases (TiB_2, TiB, h-BN, c-BN) resulting from the reaction in equation (4.1) (Table B.3). The detected strong TiB_2 peaks indicate that reaction occurred as a result of the shockwave. In addition to TiB_2 peaks, there are two peaks that can be attributed to the formation of BN phases, including c-BN (insert Fig. 6.2a). These peaks were found within samples taken from multiple cross-sections across several experiments at locations along the length of the recovery capsule, indicating repeatable formation of c-BN. However, due to the low intensities of the BN peaks, further characterization was required to verify the formation of c-BN. It should be noted that the low intensities of B and BN peaks are associated with their low scattering factors and weight fractions as compared to the Ti-based phases, as well as the small size of the synthesized crystals. As can be seen in the XRD of the initial material, despite the large volume fraction, the B peaks are substantially weaker than TiN peaks (Fig. 6.1a). As a result, detailed structure and composition analyses of the materials were performed by electron microscopy based methods to verify the composition of the recovered material.

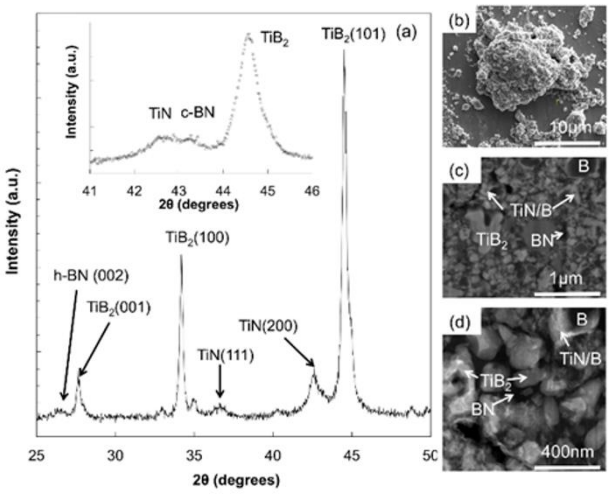

Figure 6.2. XRD (a) and micrograph (b-d) data for the shocked materials. SEM and STEM images of a composite particle (b) and particle cross-sections (c & d) in which the dark phase is BN with the lighter phase of TiB_2, some small regions consist of unreacted B surrounded by TiN.

Figure 4.2 shows typical SEM (b, c) and STEM (d) images of a reacted particle. The particle has been cross-sectioned using the focused ion beam (FIB) slice and view technique to observe its structure in reflection mode. Based on the SEM contrast, one can suggest the presence of four phases in the product material where light phases (B, BN) appeared with darker contrasts, while the phases with higher average atomic mass (e.g. TiN, TiB_2) have lighter contrasts. EDS analysis with nm scale spatial resolution in STEM mode (Fig. A.4) confirmed the elemental composition of the phases (Table B.4).

To analyze the morphology at the atomic level and crystal structure of the synthesized phases, high-resolution TEM (HRTEM) has been employed. Typical TEM images of a sample that has been subjected to the shock wave are shown in Figure 3. Analysis of over ten regions, where complete reaction occurred, reveals that all consist of the three phases: TiB_2, h-BN and c-BN. The h-BN nano-sheets are present in between the randomly oriented TiB_2 crystallites, while c-BN nano-crystals are primarily observed on the surface of the TiB_2 crystallites (see insert in Fig. 6.3a and Fig. 6.3b).

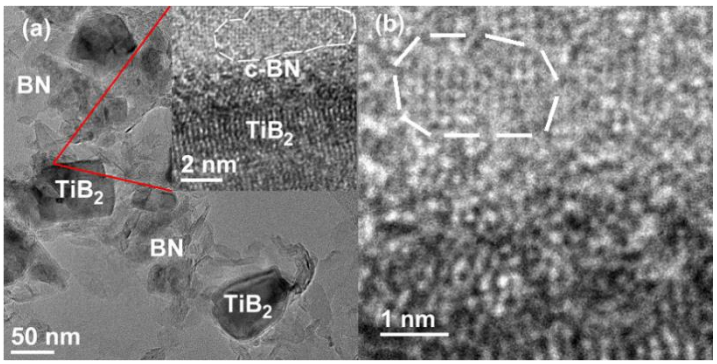

Figure 6.3. (a) TEM images of typical particles formed in Ti-B-N system after shock. Relatively large TiB_2 and h-BN crystallites are dominant within the field of view. Inset is a magnified TEM image of the surface area of large TiB_2 crystallite (70-100 nm in diameter) that has a thin layer of the c-BN phase. (b) Magnified area of c-BN crystal phase at the interface with TiB_2 crystalline particle.

During TEM imaging, the TiB_2 crystallite has been placed in low index orientation, e.g. close to <001> zone. This low zone orientation has been critical for reliable identification of c-BN, since other possible phases in the sample have d-spacings that are close (within 4%). HRTEM images have been used to identify the d-spacing with the required accuracy (down to 1%). It can be seen from Fig. 6.3(b) that 4-fold symmetry is recognizable.

It is known that the lattice parameters (d-spacing) of unstrained (perfect) crystals can be determined from HRTEM images with a relatively high accuracy of 0.2%.[148] The procedure typically involves analysis of intensity profiles taken from HRTEM images of the crystal structures. However, the accuracy of this method decreases in the case of nano-crystals. Figure 4 shows an HRTEM image of a nano-crystal in a low zone crystallographic orientation. The averaged intensity profiles were used to measure the d-spacing in both horizontal and vertical directions to increase the signal-to-noise ratio. To exclude the systematic error associated with some minor variations in magnification, the magnification for a particular HRTEM image with one of the nano-crystals in question was corrected by the measurements of the d-spacings of known crystal structures. In this work, h-BN and/or TiB_2 were used as reference crystals to determine the correction factor. For example, the (0002) d-spacing of h-BN crystallites, measured on the same HRTEM image for calibration, appeared to be 0.345 +/- 0.039 nm, instead of 0.333 nm (the database value) yielding a calibration factor of 0.96. The corrected d-spacing

value for this nano-crystal was estimated to be 0.183 +/- 0.014 nm, which fits within 1% accuracy of 0.181 nm, the (200) d-spacing of the c-BN crystal structure.

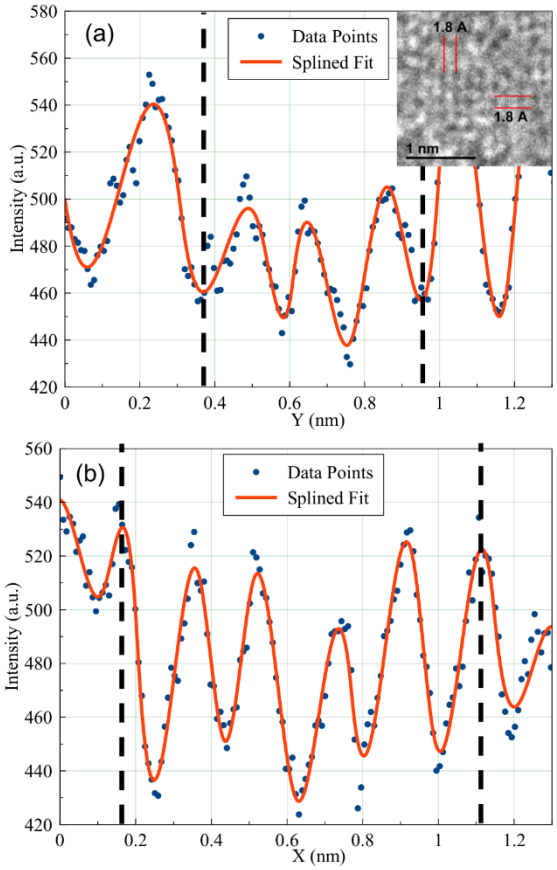

Figure 6.4. Intensity distribution on the magnified fragment of HRTEM image of c-BN phase from Fig. 3 in vertical (a) and horizontal (b) directions showing that d-spacings in both directions are close to 0.18 nm.

In order to provide further confirmation that the crystallites are the c-BN phase, we used JEMS[149] to simulate a HRTEM image and atomic model of c-BN crystallites oriented in the <001> zone (Fig. A.5a). The simulated atomic columns of B atoms (Fig. A.5b), which correspond to the white contrast on the HRTEM image taken at Scherzer focus (Fig. A.5c), fit well with the c-BN structure.

Thus it is clearly shown through XRD, HRTEM and TEM modeling that c-BN has been formed through reaction between B and TiN after the shockwave (15-20 GPa) was applied to the initial reactive nanostructured media. Since the formation of c-BN requires high P/T, there is no doubt that we have observed shock-induced reaction, i.e. the products were formed in the time

span of several μs. The maximum reaction temperature (~1900 K) in the considered system is well below melting and dissociation points for precursors and all possible product phases. An upper limit for the shock temperature at pressure can be estimated by calculating the energy deposited through shock loading, $\Delta e = \frac{1}{2} P\Delta V$ [1], and finding the temperature through integration of non-constant specific heats. Using data for β-B and TiN from the NIST Webbook [150] and a rule of mixtures, the temperature rise from a shock compressing the mixture to full density at 20 GPa would result in a temperature at pressure of approximately 2250 K. The lowest melting point in the B-TiN system is for B at 2350 K, which increases to approximately 2500 K at 20 GPa, as calculated using the Lindemann melting criteria [151,152]. This indicates that the equilibrium shock temperature would be insufficient to melt B. Additionally, the recovered powder, while having been fully compacted, maintained the overall morphology of the initial powder, and specifically showed no indication of melting. Furthermore, experiments performed on powder mixtures of 3B-TiN at identical initial densities showed that reaction did not occur (Fig. A.3). If the temperatures were sufficient to melt B, significant reaction would be expected to take place.

Cylindrical shock loading is known to be conducive to shear instabilities in the deformed mixture [153], this may result in the formation of c-BN from h-BN due to localized shearing; however, since BN is not present in any form in the initial material (as determined through high resolution TEM and XRD), reaction would need to have already rapidly occurred for any polymorph of BN to be converted into c-BN. Any residual stress would not exceed the shear strength of TiN, which can be estimated from the shear modulus to be $\tau_{max} = G/30$ [154]. Taking the elastic modulus and Poisson's ratio for TiN to be 251 GPa and 0.25, the shear modulus, G, is found to be approximately 100 GPa, giving a maximum shear strength of 3.3 GPa for a perfect TiN crystal. This suggests that any residual stress would be below the necessary 6 GPa to drive formation of c-BN. These results imply that mechanical stimulation permits the occurrence of ultra-fast chemical reaction, which may take place through solid-state mass transfer mechanisms.

CHAPTER 7. CONCLUSIONS

The results presented in this work show shock induced reaction synthesis to be a complex and highly coupled phenomenon. From nano-scale diffusion processes to meso-scale hot-spot generation and macro-scale wave propagation, every length scale is relevant in understanding and optimizing the synthesis process. This complexity makes it a scientifically rich field with the potential to produce novel materials, ensuring its continued relevance.

The importance of the mechanical properties of the powder being compacted was highlighted in both Chapter 3 and Chapter 4. In Chapter 3, two Ni-Al composite powders with nearly identical ignition temperatures were found to react on entirely different timescales as a result of a difference in mechanical properties. This is attributable to the intensity of hot-spots generated resulting from an increased hardness and brittleness of the Ni-Al nanolaminates compared to the HEBM Ni-Al. Additionally, it was shown that these hot-spots result in a phase-wave where reaction travels at a fixed delay behind a compaction front, with reaction occurring within 20 μs.

Chapter 4 showed that the rise time of a compaction front can be adjusted through ball milling. By increasing the strength of the parent material, the rise time of a compaction wave travelling through an Al compact was shortened without altering the final state achieved. The results show that a Mie-Gruneisen equation of state accurately predicts the response of all materials tested; however, the compaction width is found to change with milling condition. For all materials tested, the compaction width is found to decrease with increase pressure rise; however, the unmilled material is found to have a longer rise time compared to the ball milled material. This results in a reduction in apparent viscosity with increased crush strength. It is suggested that stress waves percolating ahead of the compaction front (since the velocity of the compaction wave is below the acoustic velocity of the parent material) and their interaction defines the compaction width. In a weaker material, a weaker stress is required to begin compaction, resulting in a broader front compared to a stronger material and an increased viscosity.

Chapter 5 addressed how the kinetics of a condensed phase reactive, Al-NiO specifically, varies with heating rate and diffusion length scale. The deposited material was found to have a complex intermixed zone after deposition, going from the NiO layer, to a metallic Ni phase, to an aluminum oxide phase, an intermetallic phase and finally the Al layer. At low heating rates,

reaction is found to occur at the layer interface and be diffusion limited, with a length scale independent growth rate of the product phase. Hot-plate ignition experiments began to show a distinct length scale dependence, with multilayers with finer thicknesses igniting below the melting point of Al. A similar response was observed at increased heating rates through laser ignition and in self-propagating reactions. With increased heating rate the observed activation energy corresponding to ignition was found to increase.

Chapter 6 applied shock induced reaction synthesis to the direct synthesis of c-BN. A limited conversion rate was observed; however, the results confirm the possibility of producing c-BN using the B-TiN system under shock loading. This result presents the first observation of a high-pressure polymorph being recovered as a product of a shock induced condensed phase reaction. The most important conclusion that can be drawn from the recovery of c-BN is that reaction and product phase formation must have occurred within the initial shock pulse, since c-BN is formed at pressures above 6 GPa. Simulation of the experimental apparatus and estimations based on the thickness of the flyer tube thickness show that the initial pulse is between 1 and 5 μs in duration. A physical mixture of B-TiN powders packed to the same density and loaded in the same manner did not react. The result shows that pretreatment through HEBM was necessary for reaction to occur. However, HEBM and diffusion distance reduction is not a panacea. During compaction of a heterogeneous mixture, energy is preferentially deposited on material interfaces [82]. As a result, further reduction of the diffusion distance results in an increase in the interfacial surface area. This results in a reduction in the peak temperature observed, with many hot-spots of lower intensity generated as opposed to a fewer number of higher temperature hot-spots. This may be remedied by loading to higher peak pressures, but there are practical limitations to this approach. This presents an optimization problem, where reduction in B crystallite size is necessary for reaction to occur, but simultaneously reduces the temperature observed at a given shock pressure.

LIST OF REFERENCES

[1] L. Davison, Fundamentals of shock wave propagation in solids, 2008.

[2] J.W. Forbes, Shock Wave Compression of Condensed Matter, Springer Berlin Heidelberg, Berlin, Heidelberg, 2012. doi:10.1007/978-3-642-32535-9.

[3] G. Duvall, R. Graham, Phase transitions under shock-wave loading, Rev. Mod. Phys. 49 (1977) 523.

[4] D.E. Eakins, N.N. Thadhani, Shock compression of reactive powder mixtures, Int. Mater. Rev. 54 (2009) 181–213.

[5] J.W. Forbes, Shock wave compression of condensed matter: A primer, 1st ed., Springer-Verlag Berlin Heidelberg, 2012.

[6] W. Herrmann, Constitutive Equation for the Dynamic Compaction of Ductile Porous Materials, J. Appl. Phys. 40 (1969) 2490. doi:10.1063/1.1658021.

[7] R.R. Boade, Principal hugoniot, second-shock hugoniot, and release behavior of pressed copper powder, J. Appl. Phys. 41 (1970) 4542–4551. doi:10.1063/1.1658494.

[8] M. Carroll, A.C. Holt, Suggested modification of the P-α model for porous materials, J. Appl. Phys. 43 (1972) 759–761. doi:10.1063/1.1661203.

[9] A.R. Nair, B.A. Mason, L.J. Groven, S.F. Son, A. Strachan, A.M. Cuitiño, Micro-RVE modeling of mechanistic response in porous intermetallics subject to weak and moderate impact loading, Int. J. Plast. 51 (2013) 1–32. doi:10.1016/j.ijplas.2013.06.009.

[10] F.P. Bowden, A.D. Yoffe, Initiation and growth of explosion in liquids and solids, CUP Archive, 1952.

[11] J.E. Field, Hot spot ignition mechanisms for explosives, Acc. Chem. Res. 25 (1992) 489–496. doi:10.1021/ar00023a002.

[12] C.M. Tarver, S.K. Chidester, A.L. Nichols III, Critical Conditions for Impact- and Shock-Induced Hot Spots in Solid Explosives †, J. Phys. Chem. 100 (1996) 5794–5799. doi:10.1021/jp953123s.

[13] M.A. Meyers, D.J. Benson, E.A. Olevsky, Shock consolidation: microstructurally-based analysis and computational modeling, Acta Mater. 47 (1999) 2089–2108. doi:10.1016/S1359-6454(99)00083-X.

[14] K. Kondo, S. Soga, A. Sawaoka, M. Araki, Shock compaction of silicon carbide powder, J. Mater. Sci. 20 (1985) 1033–1048. http://link.springer.com/article/10.1007/BF00585748 (accessed April 25, 2014).

[15] N.E. Elliott, K.P. Staudhammer, Effect of internal gas pressure on the shock consolidation of 304 stainless steel powders, Los Alamos National Lab., NM (USA), 1990.

[16] N.N. Thadhani, Shock-induced chemical reactions and synthesis of materials, Prog. Mater. Sci. 37 (1993) 117–226. doi:10.1016/0079-6425(93)90002-3.

[17] R.A. Graham, Solids under high-pressure shock compression: mechanics, physics, and chemistry, Springer Science & Business Media, 2012.

[18] Y. Horie, ShockWave Science and Technology Reference Library, Springer, 2007.

[19] K.E. Brown, W.L. Shaw, X. Zheng, D.D. Dlott, Simplified laser-driven flyer plates for shock compression science, Rev. Sci. Instrum. 83 (2012) 103901. doi:10.1063/1.4754717.

[20] Y. Horie, A.B. Sawaoka, Shock compression chemistry of materials, KTK Scientific Publishers, 1993.

[21] M.A. Meyers, S.L. Wang, An Improved Method for Shock Consolidation of Powders, Acta Metall. 36 (1988) 925–936.

[22] P.W. Cooper, Explosives Engineering, 1996.

[23] S.S. Batsanov, G.S. Doronin, S. V. Klochkov, A.I. Teut, Synthesis reactions behind shock fronts, Combust. Explos. Shock Waves. 22 (1987) 765–768. doi:10.1007/BF00751890.

[24] M.A. Meyers, Dynamic Behavior of Materials, J. Wiley, New York, NY, 1994.

[25] D. Eakins, N. Thadhani, Role of constituent configuration on shock-induced reactions in a Ni+Al powder mixture, MRS Proc. 896 (2005) 1–6. http://journals.cambridge.org/abstract_S1946427400045334 (accessed October 25, 2012).

[26] X. Xu, N.N. Thadhani, Investigation of shock-induced reaction behavior of as-blended and ball-milled Ni+Ti powder mixtures using time-resolved stress measurements, J. Appl. Phys. 96 (2004) 2000. doi:10.1063/1.1773380.

[27] R. Graham, R. Cheret, F. Eden, G. Britain, High Pressure Shock Compression of Condensed Matter, (1995). http://link.springer.com/content/pdf/10.1007/978-1-4612-1232-4.pdf (accessed December 7, 2014).

[28] N.N. Thadhani, Shock-induced and shock-assisted solid-state chemical reactions in powder mixtures, J. Appl. Phys. 76 (1994) 2129. doi:10.1063/1.357624.

[29] N.N. Thadhani, R. a. Graham, T. Royal, E. Dunbar, M.U. Anderson, G.T. Holman, Shock-induced chemical reactions in titanium–silicon powder mixtures of different morphologies: Time-resolved pressure measurements and materials analysis, J. Appl. Phys. 82 (1997) 1113. doi:10.1063/1.365878.

[30] D.E. Eakins, N.N. Thadhani, Mesoscale simulation of the configuration-dependent shock-compression response of Ni+Al powder mixtures, Acta Mater. 56 (2008) 1496–1510. doi:10.1016/j.actamat.2007.12.009.

[31] R. V. Reeves, A.S. Mukasyan, S.F. Son, Thermal and Impact Reaction Initiation in Ni/Al Heterogeneous Reactive Systems, J. Phys. Chem. C. 114 (2010) 14772–14780. doi:10.1021/jp104686z.

[32] I. Song, N. Thadhani, Shock-induced chemical reactions and synthesis of nickel aluminides, Metall. Mater. Trans. A. 23 (1992) 41–48. http://www.springerlink.com/index/T7V3U14034URW25G.pdf (accessed October 26, 2012).

[33] E. Dunbar, N. Thadhani, R. Graham, High-pressure shock activation and mixing of nickel-aluminium powder mixtures, J. Mater. Sci. 28 (1993) 2903–2914. http://www.springerlink.com/index/p68l8h854ukj2378.pdf (accessed October 25, 2012).

[34] E.B. Herbold, N.N. Thadhani, J.L. Jordan, Observation of a minimum reaction initiation threshold in ball-milled Ni+Al under high-rate mechanical loading, J. Appl. Phys. 109 (2011). doi:10.1063/1.3549822.

[35] R. V. Reeves, A.S. Mukasyan, S.F. Son, Transition from Impact-induced Thermal Runaway to Prompt Mechanochemical Explosion in Nanoscaled Ni/Al Reactive Systems, Propellants, Explos. Pyrotech. 38 (2013) 611–621. doi:10.1002/prep.201200193.

[36] B.A. Mason, L.J. Groven, S.F. Son, The role of microstructure refinement on the impact ignition and combustion behavior of mechanically activated Ni/Al reactive composites, J. Appl. Phys. 114 (2013) 113501. doi:10.1063/1.4821236.

[37] P.S. DeCarli, J.C. Jamieson, Formation of diamond by explosive shock, Science (80-.). 133 (1961) 1821–1822. doi:10.1017/CBO9781107415324.004.

[38] R. Haubner, M. Wilhelm, R. Weissenbacher, B. Lux, Boron nitrides—properties, synthesis and applications, 2002. http://link.springer.com/chapter/10.1007/3-540-45623-6_1 (accessed February 6, 2014).

[39] L. Vel, G. Demazeau, J. Etourneau, Cubic boron nitride: synthesis, physicochemical properties and applications, Mater. Sci. Eng. B. 10 (1991) 149–164. doi:10.1016/0921-5107(91)90121-B.

[40] S. Vepřek, The search for novel, superhard materials, J. Vac. Sci. Technol. A Vacuum, Surfaces, Film. 17 (1999) 2401. doi:10.1116/1.581977.

[41] F. Bundy, R. Wentorf Jr, Direct transformation of hexagonal boron nitride to denser forms, J. Chem. Phys. 38 (1963) 1144. http://scholar.google.com/scholar?hl=en&btnG=Search&q=intitle:Direct+Transformation+of+Hexagonal+Boron+Nitride+to+Denser+Forms#0 (accessed February 10, 2014).

[42] E. Rapoport, Cubic boron nitride: a review, in: Ann. Chim., Lavoisier, 1985: pp. 607–638.

[43] T. Akashi, A. Sawaoka, S. Saito, M. Araki, Structural changes of boron nitride caused by multiple shock-compressions, Jpn. J. Appl. Phys. 15 (1976) 891–892. doi:10.1143/JJAP.15.891.

[44] T. Soma, A. Sawaoka, S. Saito, Characterization of wurtzite type boron nitride synthesized by shock compression, Mater. Res. Bull. 9 (1974) 755–762. doi:10.1016/0025-5408(74)90110-X.

[45] T. Akashi, H.R. Pak, A.B. Sawaoka, Structural changes of wurtzite-type and zincblende-type boron nitrides by shock treatments, J. Mater. Sci. 21 (1986) 4060–4066. doi:10.1007/BF00553469.

[46] T. Sekine, T. Sato, Shock-induced mechanisms of phase transformation from rhombohedral BN to cubic BN, J. Appl. Phys. 74 (1993) 2440–2444. doi:10.1063/1.354680.

[47] T. Taniguchi, T. Sato, W. Ijtsumi, T. Kikegawa, In-situ X-ray observation of phase transformation of rhombohedral boron nitride under static high pressure and high temperature G-0, 6 (1999).

[48] N.L. Coleburn, J.W. Forbes, Irreversible Transformation of Hexagonal Boron Nitride by Shock Compression, J. Chem. Phys. 48 (1968) 555. doi:10.1063/1.1668682.

[49] S.S. Batsanov, L.J. Kopaneva, E. V. Lazareva, I.M. Kulikova, R.L. Barinsky, On the Nature of Boron Nitride E-Phase, Propellants, Explos. Pyrotech. 18 (1993) 352–355. doi:10.1002/prep.19930180608.

[50] A. V. Pokropivny, Structure of the boron nitride E-phase: Diamond lattice of B12N12 fullerenes, Diam. Relat. Mater. 15 (2006) 1492–1495. doi:10.1016/j.diamond.2005.11.003.

[51] A. Olszyna, J. Konwerska-Hrabowska, M. Lisicki, Molecular structure of E-BN, Diam. Relat. Mater. 6 (1997) 617–620. doi:10.1016/S0925-9635(96)00716-9.

[52] S.S. Batsanov, Features of phase transformations in boron nitride, Diam. Relat. Mater. 20 (2011) 660–664. doi:10.1016/j.diamond.2011.03.020.

[53] S.S. Batsanov, G.E. Blokhina, A.A. Deribas, The effects of explosions on materials - Structural changes in boron nitride, J. Struct. Chem. 6 (1965) 209–213. doi:10.1007/BF00745942.

[54] J. Wang, Y. Gu, Z. Li, W. Wang, Z. Fu, Growth and optical properties of explosion phase boron nitride octahedron crystals, Cryst. Growth Des. 13 (2013) 599–605. doi:10.1021/cg3012525.

[55] R. Liepins, K. Staudhammer, K. Johnson, M. Thomson, Shock-induced synthesis. I. Cubic boron nitride from ammonia borane, Mater. Lett. 7 (1988) 44–46. http://www.sciencedirect.com/science/article/pii/0167577X88900791 (accessed March 17, 2014).

[56] C. Collins, N. Thadhani, Z. Iqbal, Shock-compression of C–N precursors for possible synthesis of β-C3N4, Carbon N. Y. 39 (2001) 1175–1181. doi:10.1016/S0008-6223(00)00234-7.

[57] R. V. Reeves, A.S. Mukasyan, S.F. Son, Microstructural effects on ignition sensitivity in Ni/Al systems subjected to high strain rate impacts, in: Shock Compression Condens. Matter - 2011, 2012: pp. 539–542. doi:10.1063/1.3686335.

[58] P.E. Specht, N.N. Thadhani, T.P. Weihs, Configurational effects on shock wave propagation in Ni-Al multilayer composites, J. Appl. Phys. 111 (2012) 73527. doi:10.1063/1.3702867.

[59] I. Sraj, P.E. Specht, N.N. Thadhani, T.P. Weihs, O.M. Knio, Numerical simulation of shock initiation of Ni/Al multilayered composites, J. Appl. Phys. 115 (2014). doi:10.1063/1.4861402.

[60] M.B. Boslough, Shock-induced chemical reactions in nickel-aluminum powder mixtures: Radiation pyrometer measurements, Chem. Phys. Lett. 160 (1989) 618–622. http://www.sciencedirect.com/science/article/B6TFN-44XDV63-BB/2/104996342a3dbfdc9c09ee6c9a9b858d.

[61] D. Eakins, N.N. Thadhani, Discrete particle simulation of shock wave propagation in a binary Ni+Al powder mixture, J. Appl. Phys. 101 (2007) 43508. doi:10.1063/1.2431682.

[62] K. V. Manukyan, B.A. Mason, L.J. Groven, Y.-C. Lin, M. Cherukara, S.F. Son, A. Strachan, A.S. Mukasyan, Tailored Reactivity of Ni+Al Nanocomposites: Microstructural Correlations, J. Phys. Chem. C. 116 (2012) 21027–21038. doi:10.1021/jp303407e.

[63] D.P. Adams, Reactive multilayers fabricated by vapor deposition : A critical review, Thin Solid Films. 576 (2015) 98–128. doi:10.1016/j.tsf.2014.09.042.

[64] J. Wang, A. Misra, An overview of interface-dominated deformation mechanisms in metallic multilayers, Curr. Opin. Solid State Mater. Sci. 15 (2011) 20–28. doi:10.1016/j.cossms.2010.09.002.

[65] B.W. Asay, B.F. Henson, P.M. Dickson, C.S. Fugard, D.J. Funk, Direct measurement of strain field evolution during dynamic deformation of an energetic material, AIP Conf. Proc. 567 (1998) 567–570. doi:10.1063/1.55702.

[66] SenTest Probability Software, (n.d.).

[67] C.E. Shuck, M. Frazee, A. Gillman, M.T. Beason, I.E. Gunduz, K. Matou??, R. Winarski, A.S. Mukasyan, X-ray nanotomography and focused-ion-beam sectioning for quantitative three-dimensional analysis of nanocomposites, J. Synchrotron Radiat. 23 (2016) 990–996. doi:10.1107/S1600577516007992.

[68] B.A. Mason, T.R. Sippel, L.J. Groven, I.E. Gunduz, S.F. Son, Combustion of mechanically activated Ni/Al reactive composites with microstructural refinement tailored using two-step milling, Intermetallics. 66 (2015) 88–95. doi:10.1016/j.intermet.2015.06.009.

[69] I.E. Gunduz, S. Onel, C.C. Doumanidis, C. Rebholz, S.F. Son, Simulations of nanoscale Ni/Al multilayer foils with intermediate Ni2Al3 growth, J. Appl. Phys. (2015) 1–6. doi:10.1063/1.4921906.

[70] A. Justice, I.E. Gunduz, S.F. Son, Microscopic two-color infrared imaging of NiAl reactive particles and pellets, Thin Solid Films. 620 (2016) 48–53. doi:10.1016/j.tsf.2016.07.090.

[71] G.M. Fritz, S.J. Spey, M.D. Grapes, T.P. Weihs, Thresholds for igniting exothermic reactions in Al/Ni multilayers using pulses of electrical, mechanical, and thermal energy, J. Appl. Phys. 113 (2013) 14901. doi:10.1063/1.4770478.

[72] K.A. Philpot, Z.A. Munir, J.B. Holt, An investigation of the synthesis of nickel aluminides through gasless combustion, J. Mater. Sci. 22 (1987) 159–169.

[73] A.J. Rosakis, J.J. Mason, G. Ravichandran, The Conversion of Plastic Work to Heat Around a Dynamically Propagating Crack in Metals, J. Mech. Behav. Mater. 4 (1993). doi:10.1515/JMBM.1993.4.4.375.

[74] D. Tabor, The Hardness of Metals, Oxford, 1951.

[75] E. Vitali, C.T. Wei, D.J. Benson, M.A. Meyers, Effects of geometry and intermetallic bonding on the mechanical response, spalling and fragmentation of Ni-Al laminates, Acta Mater. 59 (2011) 5869–5880. doi:10.1016/j.actamat.2011.05.047.

[76] H.S. Carslaw, J.C. Jaeger, Conduction of heat in solids, 1959.

[77] S. Jayaraman, O.M. Knio, A.B. Mann, T.P. Weihs, Numerical predictions of oscillatory combustion in reactive multilayers, J. Appl. Phys. 86 (1999) 800–809.

[78] K.M. Flores, R.H. Dauskardt, Local heating associated with crack tip plasticity in Zr–Ti–Ni–Cu–Be bulk amorphous metals, J. Mater. Res. 14 (1999) 638–643.

[79] J.R. Rice, N. Levy, Physics of Strength and Plasticity, edited by AS Argon, (1969).

[80] R.C. Hugo, H. Kung, J.R. Weertman, R. Mitra, J.A. Knapp, D.M. Follstaedt, In-situ TEM tensile testing of DC magnetron sputtered and pulsed laser deposited Ni thin films, Acta Mater. 51 (2003) 1937–1943. doi:10.1016/S1359-6454(02)00599-2.

[81] R.G. McQueen, S.P. Marsh, J.W. Taylor, J.N. Fritz, W.J. Carter, The equation of state of solids from shock wave studies, Academic Press New York, 1970.

[82] V.F. Nesterenko, Dynamics of Heterogeneous Materials, Springer New York, New York, NY, 2001. doi:10.1007/978-1-4757-3524-6.

[83] R.G. Kraus, D.J. Chapman, P.D. Church, P. Gould, I.G. Cullis, R. Cornish, W.G. Proud, Equation of state of ductile granular materials, DYMAT 2009 - 9th Int. Conf. Mech. Phys. Behav. Mater. under Dyn. Load. 2 (2009) 1317–1323. doi:10.1051/dymat/2009186.

[84] R.G. Kraus, D.J. Chapman, W.G. Proud, D.C. Swift, Hugoniot and spall strength measurements of porous aluminum, J. Appl. Phys. 105 (2009) 2–8. doi:10.1063/1.3133237.

[85] S.A. Sheffield, R.L. Gustavsen, M.U. Anderson, Shock loading of porous high explosives, in: High-Pressure Shock Compression Solids IV, Springer, 1997: pp. 23–61.

[86] D.E. Grady, Strain-rate dependence of the effective viscosity under steady-wave shock compression, Appl. Phys. Lett. 38 (1981) 825–826. doi:10.1063/1.92146.

[87] D.E. Grady, Structured shock waves and the fourth-power law, J. Appl. Phys. 107 (2010). doi:10.1063/1.3269720.

[88] H. Fischmeister, E. Arzt, Densification of powders by particle deformation, Powder Metall. 26 (1983) 82–88. http://scidok.sulb.uni-saarland.de/volltexte/2009/2040/ (accessed October 22, 2012).

[89] S.P. Marsh, LASL shock Hugoniot data, Univ of California Press, 1980.

[90] A.W. Justice, The Dynamic Stress-Strain Response of High-Energy Ball Milled Aluminum Powder, (2017).

[91] J.R. Asay, Shock and release behavior in porous 1100 aluminum, 87115 (1975) 197–203.

[92] N.N. Beketov, A study of the substitution of one metal by others, Kharkov University, 1865.

[93] A. Merzhanov, History and recent developments in SHS, Ceram. Int. 21 (1995) 371–379.

[94] H. Goldschmidt, O. Weil, Method of manufacturing metals., (1908).

[95] R.A. Yetter, G.A. Risha, S.F. Son, Metal particle combustion and nanotechnology, Proc. Combust. Inst. 32 (2009) 1819–1838. doi:10.1016/j.proci.2008.08.013.

[96] E.L. Dreizin, Metal-based reactive nanomaterials, Prog. Energy Combust. Sci. 35 (2009) 141–167. doi:10.1016/j.pecs.2008.09.001.

[97] S.F. Son, B.W. Asay, T.J. Foley, R. a. Yetter, M.H. Wu, G. a. Risha, Combustion of Nanoscale Al/MoO3 Thermite in Microchannels, J. Propuls. Power. 23 (2007) 715–721.

[98] K. Woll, J.D. Gibbins, K. Slusarski, A.H. Kinsey, T.P. Weihs, The utilization of metal/metal oxide core-shell powders to enhance the reactivity of diluted thermite mixtures, Combust. Flame. 167 (2016) 259–267. doi:10.1016/j.combustflame.2016.02.006.

[99] A.H. Kinsey, K. Slusarski, K. Woll, D. Gibbins, T.P. Weihs, Effect of dilution on reaction properties and bonds formed using mechanically processed dilute thermite foils, J. Mater. Sci. 51 (2016) 5738–5749. doi:10.1007/s10853-016-9876-9.

[100] I.E. Gunduz, a. Kyriakou, N. Vlachos, T. Kyratsi, C.C. Doumanidis, S. Son, C. Rebholz, Spark ignitable Ni–Al ball-milled powders for bonding applications, Surf. Coatings Technol. (2014) 8–12. doi:10.1016/j.surfcoat.2014.06.068.

[101] J. Feng, G. Jian, Q. Liu, M.R. Zachariah, Passivated iodine pentoxide oxidizer for potential biocidal nanoenergetic applications, ACS Appl. Mater. Interfaces. 5 (2013) 8875–8880. doi:10.1021/am4028263.

[102] C. Rossi, K. Zhang, D. Esteve, Nanoenergetic Materials for MEMS: A Review, J. Microelectromechanical Syst. 16 (2007) 919–931. http://ieeexplore.ieee.org/xpls/abs_all.jsp?arnumber=4285648.

[103] M. Petrantoni, C. Rossi, L. Salvagnac, V. Conédéra, A. Estève, C. Tenailleau, P. Alphonse, Y.J. Chabal, A. Samples, Multilayered Al/CuO thermite formation by reactive magnetron sputtering : Nano versus micro, J. Appl. Phys. 108 (2010).

[104] D.P. Adams, M.A. Rodriguez, J.P. McDonald, M.M. Bai, E. Jones, L. Brewer, J.J. Moore, Reactive Ni/Ti nanolaminates, J. Appl. Phys. 106 (2009) 1–8. doi:10.1063/1.3253591.

[105] G.M. Fritz, J.A. Grzyb, O.M. Knio, M.D. Grapes, T.P. Weihs, Characterizing solid-state ignition of runaway chemical reactions in Ni-Al nanoscale multilayers under uniform heating, J. Appl. Phys. 118 (2015). doi:10.1063/1.4931666.

[106] S. Fischer, M. Grubelich, A survey of combustible metals, thermites, and intermetallics for pyrotechnic applications, in: 32nd Jt. Propuls. Conf. Exhib., 1996: p. 13. doi:10.2514/6.1996-3018.

[107] K.J. Blobaum, A.J. Wagner, J.M. Plitzko, D. Van Heerden, D.H. Fairbrother, T.P. Weihs, Investigating the reaction path and growth kinetics in CuOx/Al multilayer foils, J. Appl. Phys. 94 (2003) 2923–2929. doi:10.1063/1.1598297.

[108] K.J. Blobaum, M.E. Reiss, J.M. Plitzko Lawrence, T.P. Weihs, Deposition and characterization of a self-propagating CuOx/Al thermite reaction in a multilayer foil geometry, J. Appl. Phys. 94 (2003) 2915–2922. doi:10.1063/1.1598296.

[109] N.A. Manesh, S. Basu, R. Kumar, Experimental flame speed in multi-layered nano-energetic materials, Combust. Flame. 157 (2010) 476–480.

[110] R.W. Bickes, M.C. Grubelich, J.A. Romero, D.J. Staley, R.J. Buss, P.P. Ward, K.L. Erickson, A New Concept for Very Low Energy Detonators and Torches, 1996.

[111] L. Marín, C.E. Nanayakkara, J.F. Veyan, B. Warot-Fonrose, S. Joulie, A. Esteìve, C. Tenailleau, Y.J. Chabal, C. Rossi, Enhancing the Reactivity of Al/CuO Nanolaminates by Cu Incorporation at the Interfaces, ACS Appl. Mater. Interfaces. 7 (2015) 11713–11718. doi:10.1021/acsami.5b02653.

[112] V. Kuznetsov, M. Materials Science International Team, Al-Ni-O Ternary Phase Diagram Evaluation · Phase diagrams, crystallographic and thermodynamic data: Datasheet from MSI Eureka in SpringerMaterials

[113] K. Zhang, C. Rossi, P. Alphonse, C. Tenailleau, S. Cayez, J.-Y. Chane-Ching, Integrating Al with NiO nano honeycomb to realize an energetic material on silicon substrate, Appl. Phys. A Mater. Sci. Process. 94 (2009) 957–962.

[114] R. V. Reeves, D.P. Adams, Reaction instabilities in Co/Al nanolaminates due to chemical kinetics variation over micron-scales, J. Appl. Phys. 115 (2014) 1–10. doi:10.1063/1.4863339.

[115] J. Kwon, J.M. Ducéré, P. Alphonse, M. Bahrami, M. Petrantoni, J.F. Veyan, C. Tenailleau, A. Estève, C. Rossi, Y.J. Chabal, Interfacial chemistry in Al/CuO reactive nanomaterial and its role in exothermic reaction, ACS Appl. Mater. Interfaces. 5 (2013) 605–613. doi:10.1021/am3019405.

[116] K.J. Blobaum, D. Van Heerden, A.J. Gavens, T.P. Weihs, Al/Ni formation reactions: characterization of the metastable Al9Ni2 phase and analysis of its formation, Acta Mater. 51 (2003) 3871–3884. doi:10.1016/S1359-6454(03)00211-8.

[117] A.S. Rogachev, S.G. Vadchenko, F. Baras, O. Politano, S. Rouvimov, N. V. Sachkova, A.S. Mukasyan, Structure evolution and reaction mechanism in the Ni/Al reactive multilayer nanofoils, Acta Mater. 66 (2014) 86–96. doi:10.1016/j.actamat.2013.11.045.

[118] M.A. Trunov, M. Schoenitz, X. Zhu, E.L. Dreizin, Effect of polymorphic phase transformations in Al2O3film on oxidation kinetics of aluminum powders, Combust. Flame. 140 (2005) 310–318. doi:10.1016/j.combustflame.2004.10.010.

[119] I. Levin, D. Brandon, Metastable Alumina Polymorphs: Crystal Structures and Transition Sequences, J. Am. Ceram. Soc. 81 (1998) 1995–2012.

[120] L.P.H. Jeurgens, W.G. Sloof, F.D. Tichelaar, E.J. Mittemeijer, Growth kinetics and mechanisms of aluminum-oxide films formed by thermal oxidation of aluminum, J. Appl. Phys. 92 (2002) 1649–1656. doi:10.1063/1.1491591.

[121] G.C. Egan, E.J. Mily, J.P. Maria, M.R. Zachariah, Probing the Reaction Dynamics of Thermite Nanolaminates, J. Phys. Chem. C. 119 (2015) 20401–20408. doi:10.1021/acs.jpcc.5b04117.

[122] P. Swaminathan, M.D. Grapes, K. Woll, S.C. Barron, D.A. Lavan, T.P. Weihs, Studying exothermic reactions in the Ni-Al system at rapid heating rates using a nanocalorimeter, J. Appl. Phys. 113 (2013) 1–8. doi:10.1063/1.4799628.

[123] J.S. Kim, T. Lagrange, B.W. Reed, M.L. Taheri, M.R. Armstrong, W.E. King, N.D. Browning, G.H. Campbell, Imaging of transient structures using nanosecond in situ TEM., Science. 321 (2008) 1472–5. doi:10.1126/science.1161517.

[124] J.S. Kim, T. Lagrange, B.W. Reed, R. Knepper, T.P. Weihs, N.D. Browning, G.H. Campbell, Direct characterization of phase transformations and morphologies in moving reaction zones in Al/Ni nanolaminates using dynamic transmission electron microscopy, Acta Mater. 59 (2011) 3571–3580. doi:10.1016/j.actamat.2011.02.030.

[125] R. Armstrong, M. Koszykowski, Combustion theory for sandwiches of alloyable materials, Combust. Plasma Synth. High-Temperature Mater. (1988) 88–99.

[126] A.B. Mann, A.J. Gavens, M.E. Reiss, D. Van Heerden, G. Bao, T.P. Weihs, Modeling and characterizing the propagation velocity of exothermic reactions in multilayer foils, J. Appl. Phys. 82 (1997) 1178–1188. doi:10.1063/1.365886.

[127] A.J. Gavens, D. Van Heerden, A.B. Mann, M.E. Reiss, T.P. Weihs, Effect of intermixing on self-propagating exothermic reactions in Al/Ni nanolaminate foils, J. Appl. Phys. 87 (2000) 1255. doi:10.1063/1.372005.

[128] G. Lahiner, A. Nicollet, J. Zapata, L. Marín, N. Richard, M.D. Rouhani, C. Rossi, A. Estève, A diffusion-reaction scheme for modeling ignition and self-propagating reactions in Al/CuO multilayered thin films, J. Appl. Phys. 122 (2017) 0–1. doi:10.1063/1.5000312.

[129] H.E. Kissinger, Variation of peak temperature with heating rate in differential thermal analysis, J. Res. Natl. Bur. Stand. (1934). 57 (1956) 217. doi:10.6028/jres.057.026.

[130] V. Baijot, D.R. Mehdi, C. Rossi, A. Estève, A multi-phase micro-kinetic model for simulating aluminum based thermite reactions, Combust. Flame. 180 (2017) 10–19.

[131] W. Yang, G.M. Bond, H. Tan, T.J. Ahrens, G. Liu, Dynamic consolidation of superhard materials, J. Mater. Res. 7 (1992) 1501–1518. doi:10.1557/JMR.1992.1501.

[132] T. Kurita, H. Matsumoto, K. Sakamoto, T. Shimada, T. Osada, K. Ojima, H. Abe, Effects of shock compression on powder mixtures of nickel and boron, J. Alloys Compd. 396 (2005) 133–138. doi:10.1016/j.jallcom.2004.12.014.

[133] B.R. Krueger, A.H. Mutz, T. Vreeland, Correlation of shock initiated and thermally initiated chemical reactions in a 1:1 atomic ratio nickel-silicon mixture, J. Appl. Phys. 70 (1991) 5362–5368. doi:10.1063/1.350217.

[134] Y. Horie, R.A. Graham, I.K. Simonsen, Synthesis of nickel aluminides under high-pressure shock loading, Mater. Lett. 3 (1985) 354. http://www.sciencedirect.com/science/article/pii/0167577X85900758 (accessed October 21, 2012).

[135] M.T. Beason, I.E. Gunduz, S.F. Son, The Role of Fracture in the Impact Initiation of Ni-Al Intermetallic Composite Reactives during Dynamic Loading, Acta Mater. 133 (2017) 247–257. doi:10.1016/j.actamat.2017.05.042.

[136] D. Eakins, N.N. Thadhani, Shock-induced reaction in a flake nickel + spherical aluminum powder mixture, J. Appl. Phys. 100 (2006) 113521. doi:10.1063/1.2396797.

[137] A.N. Dremin, O.N. Breusov, Processes Occuring in Solids under the action of powerful shock waves, Russ. Chem. Rev. 37 (1968) 392–402. http://www.turpion.org/php/paper.phtml?journal_id=rc&paper_id=1643 (accessed October 26, 2012).

[138] D.L. Gur'ev, Y.A. Gordopolov, S.S. Batsanov, A.G. Merzhanov, V.E. Fortov, Solid-state detonation in the zinc-sulfur system, Appl. Phys. Lett. 88 (2006) 24102.

[139] R.A. Graham, M.U. Anderson, Y. Horie, S.K. You, G.T. Holman, Pressure measurements in chemically reacting powder mixtures with the Bauer piezoelectric polymer gauge, Shock Waves. 3 (1993) 79–82. doi:10.1007/BF02115887.

[140] A.G. Merzhanov, Solid Flames: Discoveries, Concepts, and Horizons of Cognition, Combust. Sci. Technol. 98 (1994) 307–336. doi:10.1080/00102209408935417.

[141] C.E. Shuck, K. V. Manukyan, S. Rouvimov, A.S. Rogachev, A.S. Mukasyan, Solid-flame: Experimental validation, Combust. Flame. 163 (2016) 487–493. doi:10.1016/j.combustflame.2015.10.025.

[142] R.H. Wentorf Jr, Cubic form of boron nitride, J. Chem. Phys. 26 (1957) 956.

[143] V.L. Solozhenko, V.Z. Turkevich, Thermoanalytical study of the polymorphic transformation of cubic into graphite-like boron nitride, J. Therm. Anal. 38 (1992) 1181–1188. doi:10.1007/BF01979178.

[144] L.F. Dobrzhinetskaya, R. Wirth, J. Yang, H.W. Green, I.D. Hutcheon, P.K. Weber, E.S. Grew, Qingsongite, natural cubic boron nitride: The first boron mineral from the Earth's mantle, Am. Mineral. 99 (2014) 764–772. doi:10.2138/am.2014.4714.

[145] T.S. Bilyan, K.V. Manukyan, S.L. Kharatyan, J.A. Puszynski, Mechanochemically and Thermally Activated Combustion of the B-TiN System, Int. J. Self-Propagating High-Temperature Synth. 15 (2006) 235–245. http://www.ism.ac.ru/n_journal/2006_3/4.pdf (accessed November 10, 2014).

[146] A.A. Bakanova, V.A. Bugayeva, I.P. Dudoladov, R.F. Trunin, Shock compression of nitrides and carbides of metals, Izv. Phys. SOLID EARTH C/C Fiz. ZEMLI-ROSSIISKAIA Akad. Nauk. 31 (1995) 513–518.

[147] J.M. McGlaun, S.L. Thompson, CTH: A three-dimensional shock wave physics code, Int. J. Impact Eng. 10 (990) 351–360.

[148] J. Biskupek, U. Kaiser, Practical considerations on the determination of the accuracy of the lattice parameters measurements from digital recorded diffractograms, J. Electron Microsc. (Tokyo). 53 (2004) 601–610.

[149] P. Stadelmann, JEMS Java Electron Microscopy Software, 2004.

[150] P.J. Linstrom, W.G. Mallard, NIST chemistry webbook, (2001).

[151] S. Spiliopoulos, F.D. Stacey, The earth's thermal profile: Is there a mid-mantle thermal boundary layer?, J. Geodyn. 1 (1984) 61–77. doi:10.1016/0264-3707(84)90006-1.

[152] M. Ross, Generalized Lindemann melting law, Phys. Rev. 184 (1969) 233–242. doi:10.1103/PhysRev.184.233.

[153] V.F. Nesterenko, M.A. Meyers, H.C. Chen, J.C. LaSalvia, Controlled high-rate localized shear in porous reactive media, Appl. Phys. Lett. 65 (1994) 3069. doi:10.1063/1.112509.

[154] T.H. Courtney, Mechanical behavior of materials, Waveland Press, 2005.

APPENDIX A. AL/NIO PRODUCT PHASE ANALYSIS

Table A.1. Product phase lattice parameters measured through STEM selected area diffraction with candidate phases. The results indicate Ni and Al_2O_3 as the primary product phases.

d(Å)	Al	NiO	Ni	Al_2O_3				
				η	γ	θ	δ	α
							7.6	
							6.4	
							5.53	
							5.1	
						5.7	4.57	
						5.45	4.07	
4.6				4.6	4.56	4.54	3.61	
2.8				2.8	2.8	2.837	3.23	3.479
						2.73	3.05	
						2.566	2.881	
						2.444	2.728	
2.4		2.41		2.4	2.39		2.601	
2.38					2.28		2.46	2.552
							2.402	2.379
2.3	2.338					2.315	2.315	2.165
				2.27		2.257	2.279	
2.16							2.16	
2.1								
2.09		2.088						2.085
2.034			2.034					
	2.024					2.019		
				1.97	1.97		1.986	1.964
						1.9544	1.953	
						1.9094	1.914	
							1.827	
1.762			1.762				1.81	
						1.7998		
						1.7765		
						1.7376		
								1.74
						1.6807		
1.63						1.6216	1.628	1.601

APPENDIX B. SUPPLEMENTAL INFORMATION ON SHOCK SYNTHESIS OF CUBIC BORON NITRIDE

Materials and Methods

Material Preparation

High-energy ball milling (HEBM) was used to produce composite B-TiN particles. A summary of relevant milling parameters may be found in Table B.1. The B (98% purity, < 44 μm, Alfa Aesar) and TiN (99.5% purity, < 44 μm, Alfa Aesar) were mixed at a 3:1 molar ratio, respectively, using a planetary ball mill (Retsch PM 100) with a 500 mL steel milling jar. The milling media was 440C stainless steel balls of diameter 4.75 mm with a 40:1 media to powder mass ratio. The jar was purged of air with argon gas. No process control agent was used. The milling was performed in 5 min increments of active milling with 15 min rest periods between to prevent reactions during milling. This was repeated for 12 periods resulting in a total active milling time of 60 min.

Explosive Compaction

A double walled cylindrical compaction experiment (Fig. A.1) was used to explosively load the milled powders. The configuration used was based on Meyers and Wang [35]. Copper tubes were closed with mild steel caps and wrapped by 3-4 mm thick Primasheet 1000. The inner copper tube had an inner diameter, thickness and height of 10 mm, 1 mm and 40 mm respectively. The outer copper tube had an inner diameter, thickness and height of 20 mm, 2 mm and 46 mm respectively. Both the HEBM powder and a physical mixture of the initial powder were hand packed into their respective capsules resulting in relative densities of 50% ± 3%.

The explosive was initiated by a detonator placed coaxially with the cylinder, initiating a detonation front that travels from top to bottom. This drives the outer copper tube inward, collapsing on the inner cylinder that contains the powder, generating a cylindrically convergent shock that travels the length of the sample. The entire recovery capsule was recovered intact containing the powder. The material was then recovered using a diamond saw.

The compaction process was simulated for an inert powder using CTH, a shock physics hydrocode developed by Sandia National Laboratories [35]. McQueen's mixture theory [32] was

used to construct an equation of state for the ball milled powder using experimental data for B [33] and TiN [34]. In McQueen's mixture theory, the mixture Hugoniot is constructed by first determining the zero Kelvin isotherms of the individual constituents from Hugoniot data. The specific volume and energy are then mixed on a mass fraction basis to create the mixture zero Kelvin isotherm. This is then used to determine the shock response of the mixture. A full description of this process may be found in McQueen et al [32]. A linear relation between shock and particle velocities was fit and implemented as a Mie-Gruneisen EOS within CTH (see Table B.2). The mixture was assumed to have a crush strength on the order of 5 GPa with the porous response being represented with a 2nd order P-α relation. Primasheet 1000 was modelled using a programmed burn with JWL equation of state with parameters taken from Kittel et al [43]. The Steinberg Guinan Lund constitutive model [44] was chosen to model the strain rate dependent behavior of the steel caps and copper tubes. The results of these simulations show a Mach stem forming as the wave propagates the length of the tube with peak pressures on the order of 15-20 GPa (Fig. A.2).

Phase Identification

X-ray diffraction (XRD) was performed on the recovered material using a Bruker D8 diffractometer to identify crystalline reaction products. A step size of 0.02 degrees with a scan rate of 0.5 degrees per minute was used. The recovered material was crushed into a powder and mounted on a Si zero diffraction plate (MTI Corp). The peaks observed were compared to a diffraction database, with the most important possible products presented in Table B.3. Traces from experiments performed on a physical mixture of 3B-TiN and the HEBM 3B-TiN are presented in Fig. A.3.

Scanning electron microscopy (SEM) imaging, Energy-Dispersive X-ray Spectroscopy (EDS) analysis of the initial and product material, and preparation of cross-sections of composite particles by Focus Ion Beam (FIB), have been performed using a FEI Helios SEM/FIB NanoLab. A FEI TITAN 80-300 transmission electron microscope (TEM) has been employed for high-resolution imaging in both TEM and Scanning TEM modes as well for EDS analysis with 1 nm spatial resolution. The resolution of TITAN is 0.2 nm (point-to-point) and 0.134 nm in TEM and STEM modes, respectively. The Java Electron Microscopy Software, or JEMS [37], is used to simulate the contrast in high-resolution TEM images.

Ignition Temperature

A thin disc was pressed from the 3B/TiN composite powder with a C-type thermocouple inserted into the center of the disc. The test material was placed on a graphite strip. An electrical current is passed through the graphite to rapidly heat the surface to 1800 C. The temperature rise of the test material is recorded via the thermocouple and the ignition temperature is calculated from this data as seen in Fig. A.6.

Supplementary Text

Confidence in Phase Identification

Samples potentially containing c-BN, as determined through XRD, were further analyzed using SEM, TEM and EDS. EDS was used to identify the compositions of individual regions within Fig. A.4. Compositions within these regions were identified as B, TiB_2, TiN, and BN as presented in Table B.3.

Once a candidate crystal was identified, intensity distributions were measured to obtain precise measurements of the observed lattice fringes as shown in Figure 4. Fig. A.5 shows the results of simulated TEM images of c-BN using JEMS. The crystal structure of c-BN was input into the software. Image contrast and lattice fringes within the simulated image compare favorably with those obtained experimentally. The results of XRD combined with TEM imaging provide high confidence that this phase is c-BN.

Figure A.1. Concentric cylinder powder compaction experiment as well as an image of the capsule before and after shock.

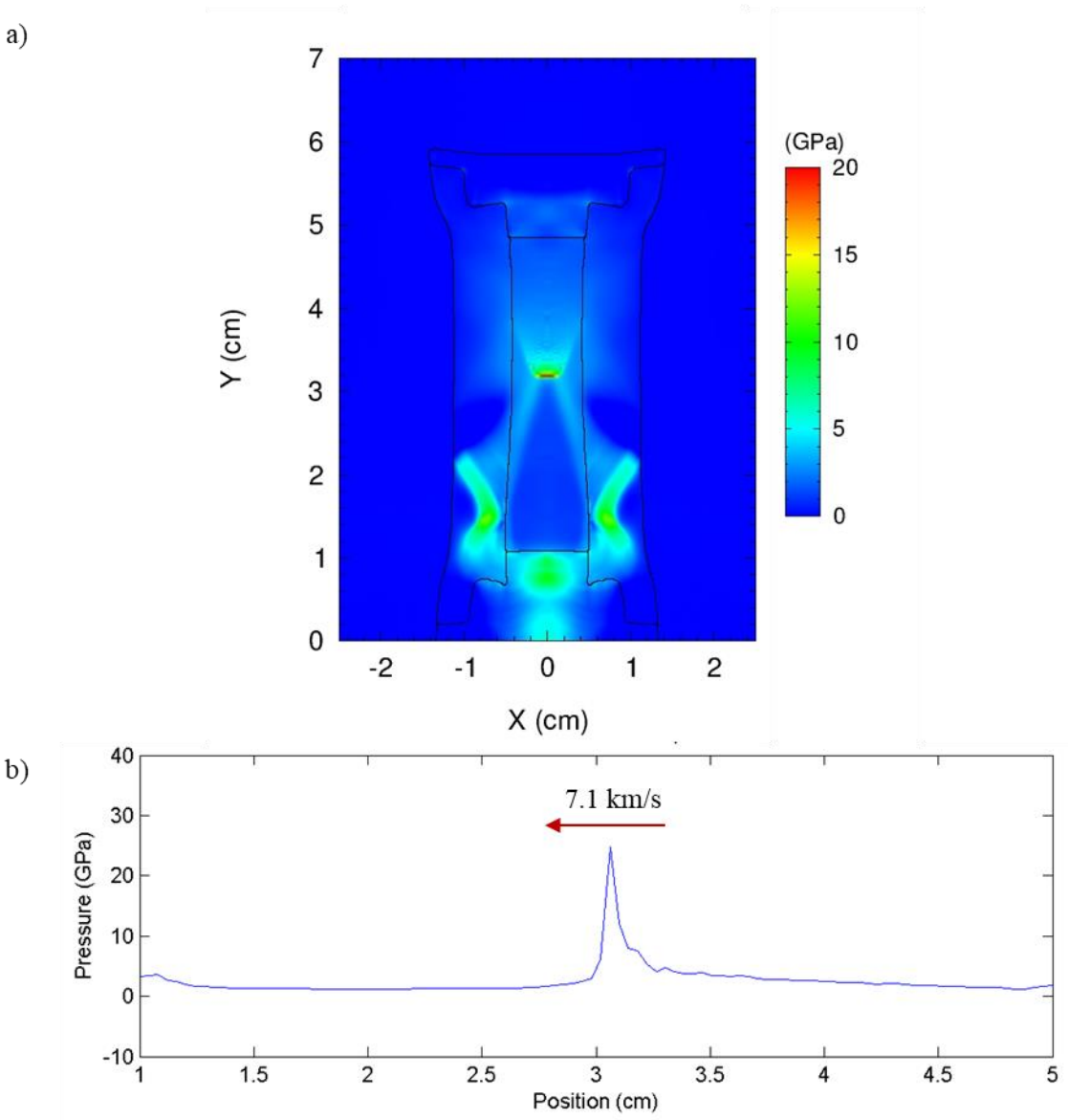

Figure A.2. a) Still frame taken at 19 μs after initiation of explosive at the top showing the generation of a mach stem geometry with peak pressure occurring on the centerline. b) Pressure trace taken along the centerline of the presented frame. Note that the peak pressure is approximately 20 GPa with a width of approximately 5 mm. This wave travels at the detonation velocity of the explosive (7.1 km/s).

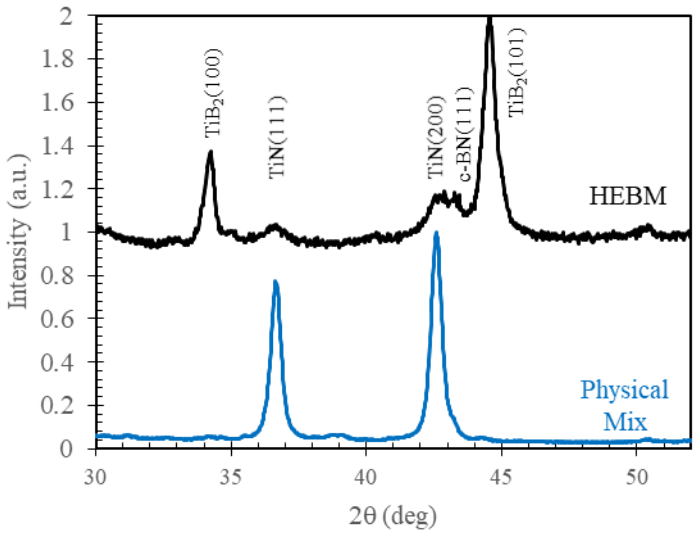

Figure A.3. XRD showing that shock loading of a physical mixture of B and TiN powders does not react, while the HEBM powders show strong peaks for TiB_2, indicating reaction.

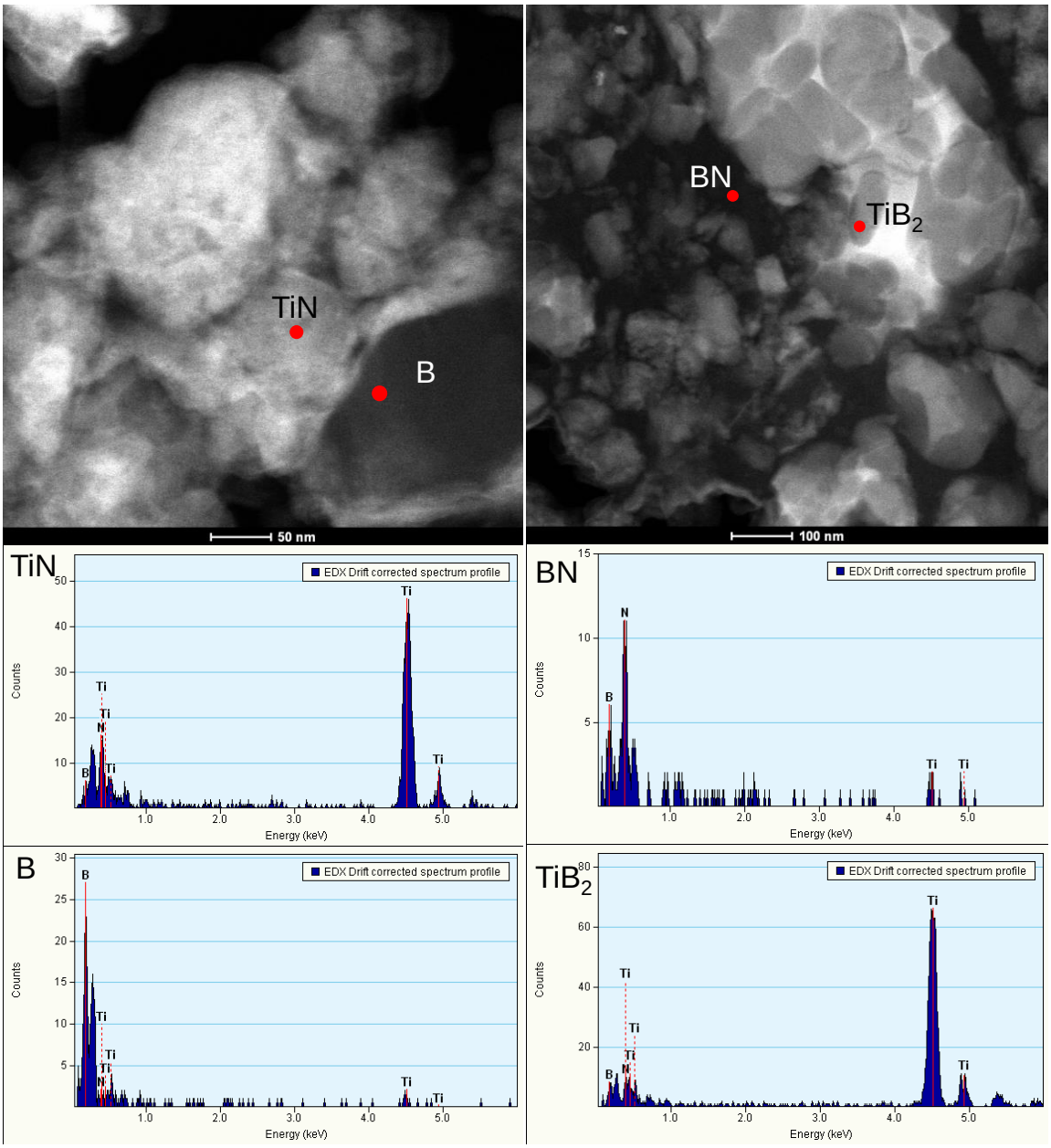

Figure A.4. EDS Analysis for TiB_2, TiN, B, and BN regions.

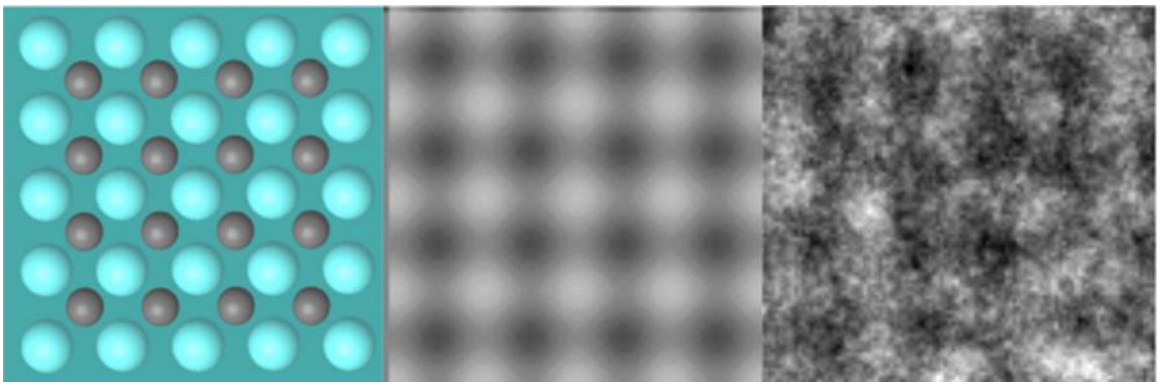

Figure A.5. Caption: L-R: Atomic model of c-BN in the <001> zone, simulated HRTEM image of c-BN in the <001> zone, and magnified fragment of TEM image of c-BN phase (see Figure 3) which is in the <001> crystallographic zone. In the atomic model, B atoms are light blue and N atoms are dark grey. White contrast in both experimental and simulated HRTEM images is associated with B atomic columns.

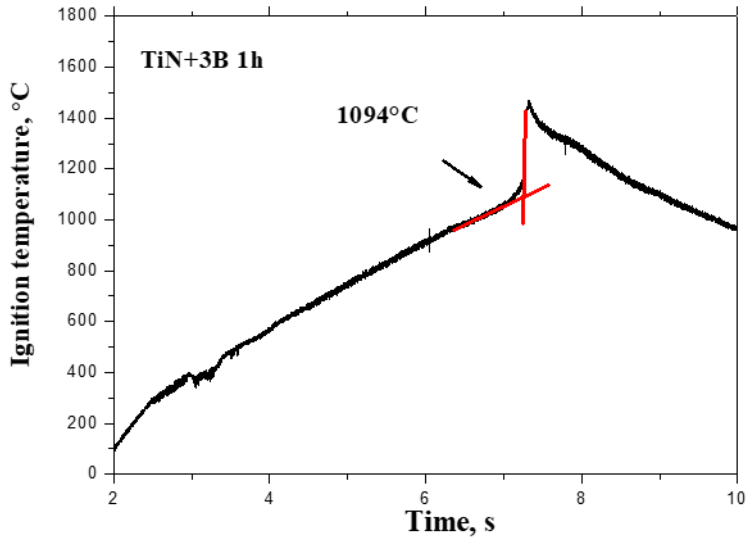

Figure A.6. Thermal ignition temperature of 3B+TiN composite powder prepared using the Retsch PM 100 planetary mill.

Table B.1. Milling conditions used with Retsch PM 100 planetary mill for production of 3B+TiN composite powders.

Parameter	Value
Boron Particle Size	< 44 μm
TiN Particle Size	< 44 μm
Ball-Powder Ratio	40:1
Media Diameter	4.75 mm
Media Type	440C SS
Media Mass	175 g
Milling Rate	650 RPM
Period	20 min
Duty Cycle	25%
Periods Run	12

Table B.2. Material parameters used for 3B+TiN composites with Mie-Gruneisen EOS in CTH. C_s and S are the intercept and slope of a linear shock velocity versus particle velocity Hugoniot. C_v and Γ_0 are the reference heat capacity and Gruneisen parameter determined from a rule of mixtures. P_s and P_e are the assumed crush strength and elastic limit of the powder composites.

Parameter	Value
C_s(km/s)	7.91
S	0.465
C_v(J/g K)	0.884
Γ_0	0.726
P_s(GPa)	5
P_e(GPa)	1

Table B.3. Powder diffraction standards for initial and product phases (3-4 highest intensity reflections).

Compound (PDF #)	(hkl)	d-spacing (nm)	2θ (degrees)	Relative Intensity
β r-B (04-007-2390)	003	0.7938	11.137	61
	104	0.5039	17.587	100
	021	0.4640	19.112	59
	113	0.4500	19.712	26
TiN (00-038-1420)	111	0.2449	36.6621	72
	200	0.2121	42.5959	100
	220	0.1500	61.8123	45
TiB_2 (00-035-0741)	001	0.3230	27.5973	22
	100	0.2625	34.1322	55
	101	0.2037	44.4269	100
	110	0.1515	61.1042	27
c-BN (00-035-1365)	111	0.2087	43.3140	100
	200	0.1808	50.4300	5
	220	0.1278	74.0897	24
	311	0.1090	89.9307	8
h-BN (00-034-0421)	002	0.3328	26.7644	100
	100	0.2169	41.5970	15
	102	0.1818	50.1487	9

Table B.4. Atomic composition as measured through EDS of regions presented in Figure A.4.

Phase	B (atomic %)	N (atomic %)	Ti (atomic %)
TiN	6.4	47.1	41.1
B	99.8	0.0	0.2
TiB_2	28.3	0.0	71.7
BN	61.1	38.9	0.0

VITA

Matt Beason was born on March 5, 1990 in Sedan, Kansas to parents Jim and Diana Beason. He received his B.S. in Mechanical Engineering from Kansas State University in 2012. He was fortunate enough to marry Anne Wicoff in the spring of 2013. He went on to receive his Ph.D. in Mechanical Engineering from Purdue University in 2018.

PUBLICATIONS

Journal Articles

- **M. T. Beason**, J. Pauls, I. E. Gunduz, S. Rouvimov, K. Manukyan, K. Matous, S. F. Son, A. S. Mukasyan. 2018. *Shock Induced Reaction Synthesis of Cubic Boron Nitride.* Accepted, Applied Physics Letters.
- B. Claus, J. Chu, **M. T. Beason**, H. Liao, B. Martin, W. Chen. 2017. *Dynamic Experiments using Simultaneous Compression and Shear Loading.* Experimental Mechanics, 57.9, 1359-1369.
- **M. T. Beason**, I. E. Gunduz, and S. F. Son. 2017. *The Role of Fracture in the Impact Initiation of Ni-Al Intermetallic Composite Reactives during Dynamic Loading*. Acta Materialia, 133, 247-257.
- A. Salvadori, S. Lee, A. Gillman, K. Matous, C. Shuck, A. Mukasyan, **M. T. Beason**, I. E. Guduz, S. F. Son. 2017. *Numerical and Experimental Analysis of the Young's Modulus of Cold Compacted Powder Materials*. Mechanics of Materials, 112, 56-70.
- C. E. Shuck, M. Frazee, A. Gillman, **M. T. Beason**, I. E. Gunduz, K. Matous, and A. S. Mukasyan. 2016. *X-ray Nanotomography and Focused-Ion-Beam Sectioning for Quantitative Three-Dimensional Analysis of Nanocomposites.* Journal of Synchrotron Radiation, 23(4), 990-996.

Articles in Review or in Draft

- **M. T. Beason**, M. J. Abere, M. A. Rodriguez, C. E. Sobczak, R. V. Reeves, S. F. Son, C. D. Yarrington, D. P. Adams. *The Ignition Kinetics and Self-Propagating Reaction of 2Al+3NiO Rective Multilayer Thin Films.* In draft, Journal of Physical Chemistry C.
- **M. T. Beason**, I. E. Gunduz, C. Rebholz, C. C. Doumanidis, A. Mukasyan, S. F. Son. 2018. *Sub-Critical Hotspots to Quench Reactions in Ni-al Nanofoils*. In draft, Applied Physics Letters.
- **M. T. Beason**, J. Pauls, I. E. Gunduz, T. Manship, A. Mukasyan, B. J. Jensen, S. F. Son. 2018. *Dynamic Compaction of Ball Milled Al Green Bodies.* In draft, Acta Materialia.

Selected Conference Presentations and Posters

- **M. T. Beason**, A. W. Justice, I. E. Gunduz, W. Chen, and S. F. Son. *The Effect of High Energy Ball Milling on the Dynamic Response of Aluminum Powders.* Oral Presentation, APS Topical Conference on the Shock Compression of Matter 2017, St. Louis, MO, July 10-14, 2017.
- **M. T. Beason**, I. E. Gunduz, A. Mukasyan, and S. F. Son. *Sub-Critical Hotspots to Quench Reactions in Ni-Al NanoFoils.* Oral Presentation, International Conference on Metallurgical Coatings and Thin Films, San Diego, CA, April 23-27, 2017.
- **M. T. Beason**, M. J. Abere, R. V. Reeves, S. F. Son, and D. P. Adams. *Combustion of Al-NiO Nanolaminate Thermites*. Poster, Gordon Research Conference on Energetic Materials, Stowe, VT, June 5-10, 2016.
- **M. T. Beason**, I. E. Gunduz, A. S. Mukasyan, and S. F. Son. *Shockwave Processing of Composite Boron and Titanium Nitride Powders*. Oral Presentation, APS Topical Conference on the Shock Compression of Matter 2015, Tampa, FL, June 15-20, 2015.
- **M. T. Beason**, I. E. Gunduz, A. S. Mukasyan, and S. F. Son. *Combustion Synthesis of Hexagonal Boron Nitride Using Mechanically Activated Boron and Titanium Nitride Precursors*. Oral Presentation, Materials Research Society Fall Meeting and Exhibit, Boston, MA, November 30-December 4, 2014.